



AALBORG UNIVERSITY
DENMARK

Design of Mechanical Systems

MASTER THESIS

SPRING 2018

Substructure Assembly of Composite Structures

EFREN GONZALEZ MADRUGA



AALBORG UNIVERSITY
STUDENT REPORT

**Study Board of Industry and Global
Business Development**

Fibigerstraede 16, 9220 Aalborg

Phone +45 99 40 93 09

<http://info@m-tech.aau.dk>

Title:

Substructure Assembly of Composite Structures

Project:

DMS4, Spring Semester 2018

Semester theme:

Master Thesis

Period:

01/02/18 - 16/08/18

Author:

Efrén González Madruga

Aau Supervisor:

Jørgen Asbøll Kepler

Collaboration with company:

Agile Automotive

Company Supervisor:

Alfredo Esbrí Mateu

Synopsis:

The present master thesis shows a research work related to bonded joints in composites together with a design for manufacturing work within the field of composite substructures. The geometry of a carbon fibre chassis is designed for the new car Agile SC122 from Agile Automotive. The geometry is divided into sub-structures in order to make it possible to manufacture, so bonded joints are required into the design.

The possibility of using thermoplastic resins for the chassis design is investigated with the aim of comparing the welded joints with adhesive bonded joints. However, after mechanical and processing tests, the thermoset resin is finally chosen. The selection is made based on the lower inter laminar shear strength that, after testing, the thermoplastic resin shows. Since a thermoset resin is chosen for the chassis design, the material is characterized analytically by using micromechanics theory.

The critical joint of the structure is identified and represented in a multi-scale model. The joint geometry is designed in order to make it work in shear mode, for what an analytical approach is used to validate the finite element model of the joint. Geometry of the joint, strength optimization, and lay-up sequence are the sections covered within the adhesive joint design. A final joint design is obtained with a significant strength improvement, compared to a regular lap joint.

Number of copies: 4

Number of report pages: 80

Number of appendix pages: 30

Submission: 16/08/2018

Resumé

Denne rapport præsenterer arbejde udført i forbindelse med projektet "Substructure Assembly of Composite Structures, og den omhandler design af kompositmaterialer der tilgodeser fremstilling.

Arbejdet tager udgangspunkt i den nuværende metode til at samle emner af kompositmateriale, som er samlinger af understrukturer ved hjælp af lim.

I samarbejde med Agile Automotive er et nyt chassis til Agile SC122 designet. Geometrien er optimeret med formålet at reducere masse og øge stivhed. Et litteraturstudie danner baggrund for materialevalg, og en ny termoplastisk resin er testet og sammenlignet med traditionelt temperaturhærdnet epoxy resin. Det valgte materiale er beskrevet analytisk ved hjælp af teori om mikromekanik af kompositmaterialer.

Chassiset er inddelt i understrukturer baseret på spændingsfordelingen i samlingslinjerne. Den kritiske samling er lokaliseret og submodelleret. En simplificeret repræsentation af samlingen er modelleret ved en FEM-analyse med det formål at finde en optimeret geometri, der skal reducere tværspændinger og peel spændinger i samlingslinjerne. FEM modellen er valideret ved sammenligning med analytiske modeller.

Et Matlab program er udviklet til at beregne samlinger med et overlap på baggrund af Goland & Reissner modellen.

Effekten af stivheden og tykkelsen af limsamlingerne på den overordnede samlingsstyrke er undersøgt, og designforslag for samlinger med lim i et chassis er opstillet. Derudover er effekten af fibermåtte oplægs-rækkefølgen undersøgt, og afsluttende designanbefalinger er udarbejdet.

Eksperimenter og fysiske tests er udført ved Agile Automotives faciliteter. Finite Element beregninger er lavet ved brug af ANSYS Workbench 18.2, og analytiske beregninger og programmer er lavet i Matlab R2017b. Materiale prøver såsom termoplastisk resin og kulfibermåtter med termoplastisk sizing er stillet til rådighed af producenterne mod at testdata bliver tilgængelig for dem.

Firmaer involveret: Agile Automotive [Agile, Automotive], House of Composites [HOC, Composites], Arkema [Arkema, Elium], Akzo Nobel [Akzo, Nobel], Chomorat composites [Chomarat, Fabrics].

Preface

This report is a master thesis from the fourth semester of the program *Design of Mechanical Systems* from Aalborg University.

The theme of the project is substructure assembly of composite structures. The aim of this thesis is to gain a deeper understanding in design for manufacturing of composite structures while focusing on structural bonded joints. During the thesis period, research work is done and tests are performed. For the tests, an electric tensile test machine Lloyd LR100K by courtesy of Agile Automotive is used. Thanks are due to the internal supervisor Jørgen Asbøll Kepler, the company supervisor Alfredo Esbrí Mateu, and the CTO of Agile Automotive, Tim Hansen.

Included figures and tables are numbered with respect to the chapter number. Figures and tables are distinguished implying that, for instance, both figure 1.1 and table 1.1 exist. During the report references will occur and a list of all the used references is to be found in the end of the report. The used method for the references is the Harvard method meaning that the references are in the form [authors surname, year]. In the list of references, books are described as follows: author's name, title, publisher, year. If the reference is a website, the description includes: authors' names, title, url and downloading date.

The author apologises for the possible lack of quality of figures and images as well as for the possible writing errors. All sketches in the figures are hand made by the author and the screen shots from CAD files or FEM files come from the author's own work. The following software have been used: SOLIDWORKS 2016, ANSYS 18.2, AUTODESK AUTCAD 2017, MICROSOFT EXCEL 2016, MATLAB R2017b, SPACE CLAIM 18.2 and TEXMAKER 4.5 for LATEX.

Aalborg Universitet, August 16th, 2018

Efrén González Madruga

Table of contents

Chapter 1 Introduction	1
1.1 Motivation	1
1.2 Problem statement and delimitation	1
1.3 Thesis Outline	3
Chapter 2 Chassis geometry design	5
2.1 Design constraints	5
2.2 Initial geometry	6
2.3 Topology optimization	7
2.4 Surface geometry	10
2.5 Mechanical model (FE)	11
2.6 Iterative design for stiffness	16
2.7 Strength validation	19
Chapter 3 Material research. Thermoplastic	23
3.1 Thermoplastic vs thermoset	23
3.2 Processing feasibility	23
3.3 Manufacturing test of thermoplastic laminate	25
3.4 A-surface quality	28
Chapter 4 Material selection	31
4.1 Inter laminar shear strength (ILSS)	31
4.2 Thermoset ILSS	33
4.3 Thermoplastic ILSS	34
4.4 Results and material choice	34
Chapter 5 Material characterization	37
5.1 Micromechanics approach	37
5.2 Calculation of material parameters	43
Chapter 6 Identification of bonded joints	45
6.1 Division of the chassis into sub-structures	45
6.2 Identification of the critical bonded joint	46
6.3 Multi-scale modeling of the bonded joint	48
Chapter 7 Adhesive joints	49
7.1 State of the art. Adhesive bonded joints	49
7.2 FEM model of the single lap joint	53
7.3 Analytical validation of the FEM	56
Chapter 8 Adhesive joint design	59
8.1 Joint geometry	59
8.2 Single lap geometry	65

8.3 Lay-up sequence effects on single lap joint strength	72
Chapter 9 Final design. Conclusions	75
References	79
Appendix A Topology optimization of the chassis geometry	81
A.1 50% mass reduction	82
A.2 60% mass reduction	83
A.3 70% mass reduction	84
A.4 80% mass reduction	85
Appendix B Shell geometry. Iterative design process	87
B.1 Iteration 1	87
B.2 Iteration 2	88
B.3 Iteration 3	89
B.4 Iteration 4	90
B.5 Iteration 5	92
B.6 Iteration 6	93
Appendix C Elium 188 XO TDS	97
Appendix D Perkadox CH-50X TDS	99
Appendix E Thermoplastic testing. A-surface issue	103
Appendix F Goland & Reissner Stress Distribution. Matlab code	109

1.1 Motivation

In the recent decades, the use of composite materials has been extended to many fields, such as wind turbines, aerospace transportation, and automotive industry. In automotive industry, composite materials have been used initially in high level categories like Formula 1. However, the design with composites in the rest of automotive categories is being implemented more each day. The need for mass reduction in the designs, in order to achieve high power efficiency, and the pursuing of a high torsional stiffness in the vehicle structure, to improve the handling of the automobile, leads to the use of composite materials. The assembly process of composite materials becomes a challenge since the classic bolted joints used for isotropic materials become structurally inefficient. Therefore, adhesive bonded joints are used in most of composite applications. Adhesive bonded joints in composites require a detailed design, validation and testing.

1.2 Problem statement and delimitation

Problem statement

The company, Agile Automotive is designing and developing the new sports car which is mostly made of carbon fiber reinforced polymer. The design of a stiff and light structure as the chassis of the car is, requires the use of the latest methods and technologies within the composite field. The bodywork is already designed and the kinematic limitations for the chassis are already defined by the company. The challenge appears when designing the chassis. A carbon fiber chassis is requested, which means that, the manufacturing viability of the structure has to be taken in to account. The manufacturing process used at the company is VARI (Vacuum Assisted Resin Infusion). Thus, the chassis structure has to be designed as an assembly of individual parts. Since the whole assembly has to carry the wheel loads, the structural bonding of the individual parts must be designed and analyzed. The present thesis covers the design of the chassis geometry with isotropic material. The mono-geometry is divided into substructures and the critical joint is identified. The critical joint is isolated and represented in Finite Element Model for a further study of the different variables of the joint, which are:

- Joint geometry
- Strength optimization
- Effects of the layup sequence on the joint strength

To carry out those studies, a research work is done about a new resin for infusion which is a thermoplastic resin, Elium. The resultant composite is tested and compared with ordinary epoxy for infusion. The chart below (1.1) shows the general lines of the problem to be analyzed.

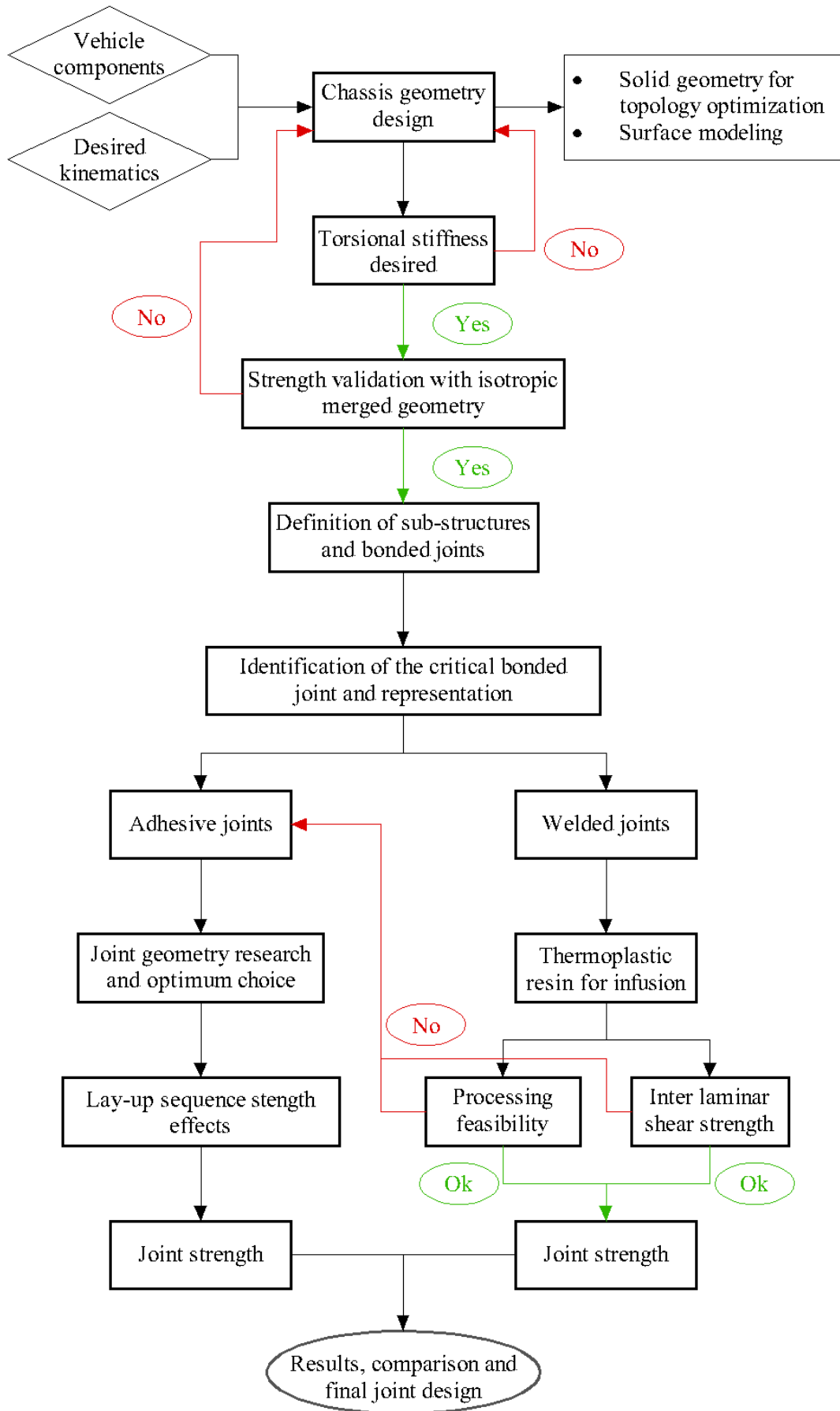


Figure 1.1. Design and research flow chart.

As it is shown in the chart, besides the main problem, previously formulated, the study of new emerging materials in the market such as thermoplastic resins for infusion is introduced. The reason is the possibility of welding, which makes the use of adhesives unnecessary. Furthermore, thermoplastic resins are totally recyclable, so they have clearly an advantage with respect to thermoset resins, whose main problem is its difficulty to be recycled.

Delimitation

Some tasks are excluded because of the lack of time, since this is a one semester thesis. Thus, the layup of the chassis and its optimization are not designed in the present report. Therefore, a final accurate joint design for the designed chassis geometry is not possible to make. The material to be used is correctly characterized but the adhesive joint research is made from a general point of view. So that the conclusions are valid for any structure without being exclusive for the structure developed along the present thesis. Moreover, the field of adhesive joints is huge. Covering every parameter which has effects on an adhesive joint would take some years. Therefore, mainly geometry design of an adhesive joint is covered. Variables like adhesive thickness, lap width, or fatigue damage are excluded from the present project. Nevertheless, this master thesis is a good introduction to the fascinating world of the adhesive joints in composite structures.

1.3 Thesis Outline

The Master thesis is split into chapters in order to obtain an easy understanding of the process followed to reach the conclusions. The thesis detailed order is set as follows.

First, a shell structure is designed and optimized with isotropic material in Chapter 2. A material research is done to choose the best composite material for the chassis structure in chapter 3. In chapter 4, the selected materials are tested in order to choose the strongest one. The resultant material is characterized analytically by using a micromechanic approach in chapter 5. The chassis shell geometry is divided into parts, making possible its manufacturing. The location of the critical joint under the chosen load scenario is found and a simplified representation is made in chapter 6. The joint mechanism is then represented numerically and analytically validated as a single lap joint in chapter 7. Chapter 8 studies the most efficient geometry design of the adhesive joint, and from a general perspective, the lay-up sequence of the composite material is studied in order to analyze its effects on the overall joint strength.

A final chassis geometry which is designed to be manufactured with composite material is obtained. The sub structuring of the chassis is modeled and the geometry of its joints is designed too. The final design and design recommendations close the present report in chapter 9.

Chassis geometry design 2

The following chapter describes the design process which leads to a final chassis geometry for the Agile SC122 car. Bodywork geometry, and scaled kinematics from the previous Agile model, the SCX, together with the engine, gearbox and seats, are used as the input constraints for the design of the new chassis.

2.1 Design constraints

Figures 2.1 and 2.2 show the geometry limitation for the design of the new chassis. An assembly with all the components is made in order to define the available space for the design. The bodywork is given by the company Agile Automotive as a CAD model. The driver is modeled according to NASA ergonomic definition, obtained from [NASA, Ergonomics] for a 40 year old man.

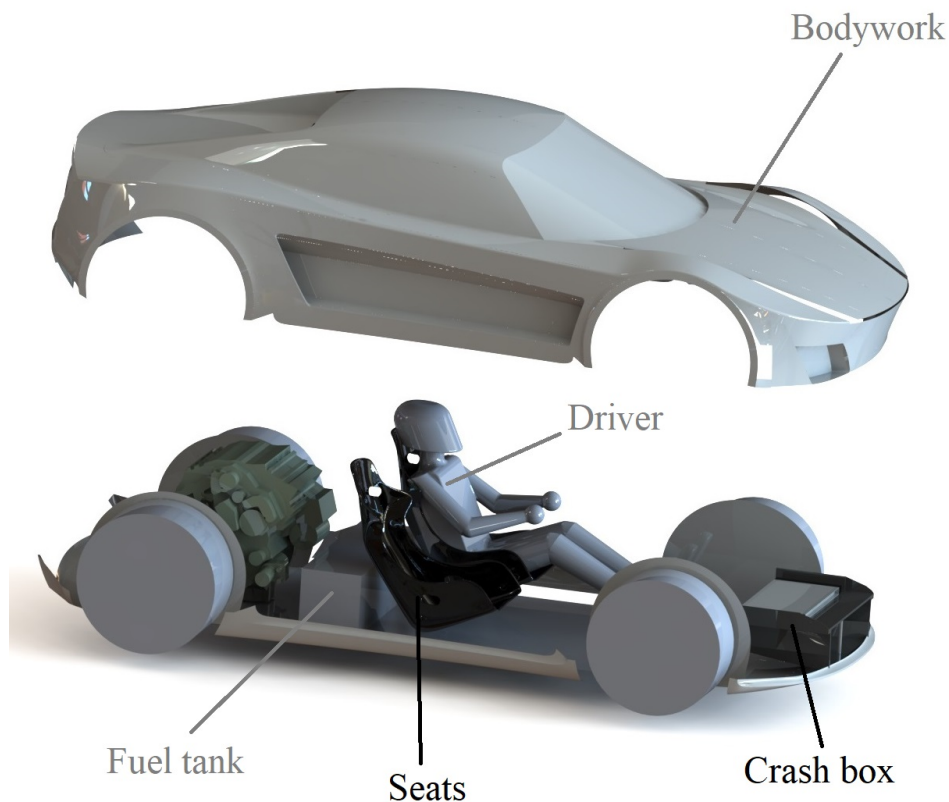


Figure 2.1. Car components. View 1.



Figure 2.2. Car components. View 2.

The seats are FIA (Federation Internationale de l'Automobile) seats, medium size. A CAD model is given by the company. The fuel tank is an off-the-shelf component chosen according to the requirements of Agile Automotive, which are a volume of more than 60 liters. Two compatible fuel tanks are chosen. The first one is a 64 liter tank for a Ford pick up [Raybuck, Fuel tanks], and the second one is a 64 liter fuel tank for a Ford Transit RWD (2000 – 2006). Both tanks have the same geometry and the same capacity. The crash box is given by the company, and the engine dimensions are obtained from the manufacturer. In this case it is a Ford Ecoboost 1,6 liters, with its respective gearbox.

Kinematics and general dimensions are also given by the company, and the wheel size.

- Wheel base: 2566,7 mm
- Front track: 1607 mm
- Rear track: 1627 mm
- Rear tire width: 325 mm
- Rear tire diameter: 20"
- Front tire width: 245 mm
- Front tire diameter: 20"
- Max. steering angle: 30°

2.2 Initial geometry

Once the available space for the chassis is defined, a solid geometry is made, fitting the assembly with all the components and respecting the kinematic dimensions.

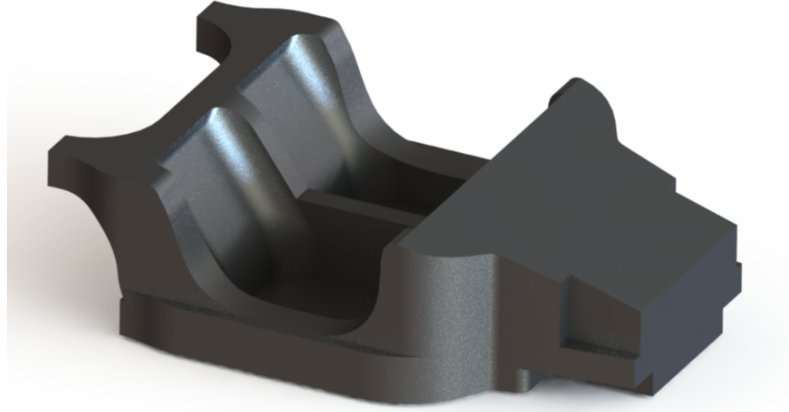


Figure 2.3. Solid initial chassis geometry.

In figure 2.3, the initial geometry is shown. To define the needed space in the sides of the car, for the easy access of the driver, a cardboard model (real size) is made, and the space for the doors is tested and defined.

2.3 Topology optimization

The chassis is designed for torsional stiffness, which means that the principal stiffness paths can be found by maximizing the stiffness of the solid geometry, while reducing the mass. Thus, topology optimization is used [Arora, 2016]. The objective function is then, the compliance of the system, to be minimized. And the constraint is the mass to retain in the model.

The problem is stated as shown below.

Objective function to minimize:

$$C(U) = U^T KU = \text{compliance}$$

subject to:

$$KU = F \quad (\text{equilibrium equations})$$

$$E_{ijkl}^H(\rho(x)) = \rho(x)^p E_{ijkl}^* \quad (\text{relation between material elasticity and density})$$

$$\int \omega \rho(x) d\omega \leq V^* = \alpha V(\omega), \quad x \in \omega \quad (\text{volume constraint})$$

$$0 \leq \rho_{min} \leq \rho(x) \leq 1, \quad x \in \omega$$

Where E_{ijkl}^H is the effective elastic tensor, p is the penalty term and α is the volume fraction of available material (20%). For this thesis, the program used is ANSYS 18.0, that uses a relaxed direct density approach. The method is called the Solid Isotropic Material with Penalization (SIMP). More information about the method can be found in [Sigmund and P.Bendsøe., 2011].

Material and mesh

The material chosen for the present optimization does not have any influence in the final results, since it is a generalized case. Thus, structural steel is used.

The discretization of the geometry is shown in figure 2.4.

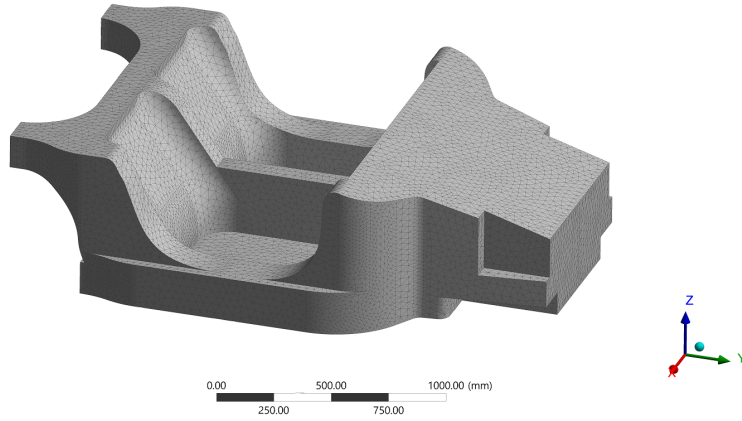


Figure 2.4. Mesh for topology optimization.

- Element type: Solid 187 tetrahedrons (10 nodes and 3 d.o.f per node)
- Number of elements: 104608
- Number of nodes: 180930

Loads

Torsional stiffness is set as a priority for the design of the chassis. A real torsional situation is difficult to model, therefore, the model is set as a superposition of two load scenarios. For the first scenario, hereinafter case 1, the front is clamped (2.6), and the torsional force is applied on the rear part of the chassis (2.5). The loads applied are two anti-symmetric loads of 5000N each one.

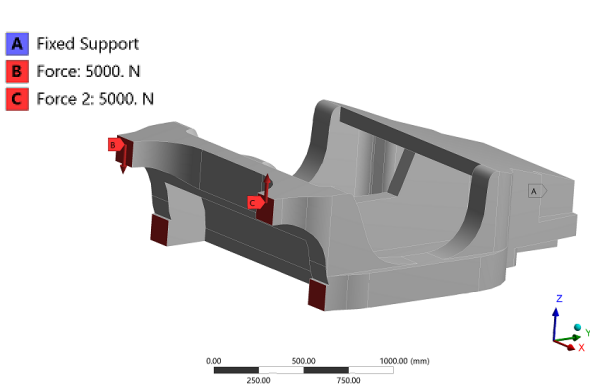


Figure 2.5. Torsional forces

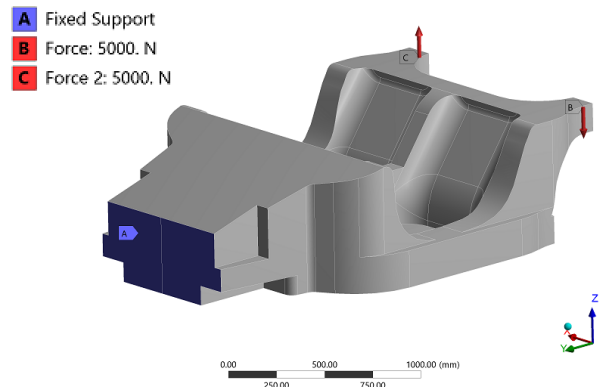


Figure 2.6. Clamped surface

The second scenario, hereinafter case 2, is the opposite, where the rear attachment points of the chassis are clamped (2.7), and the torsional force is applied at the front of the chassis (2.8).

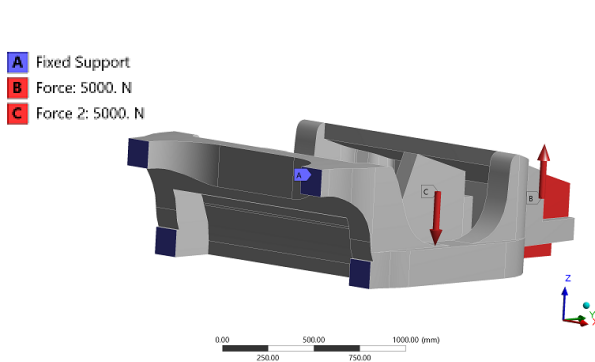


Figure 2.7. Clamped surfaces

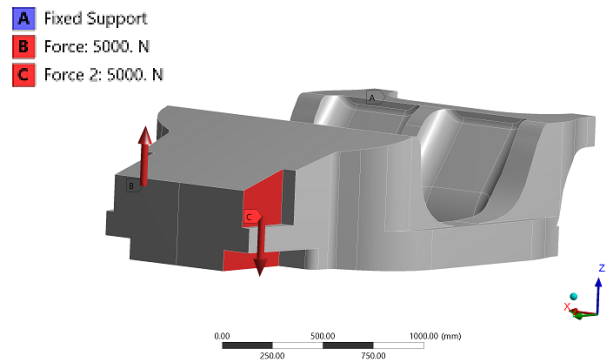


Figure 2.8. Torsional force

The reason why two scenarios are needed is because the fact that the surfaces are clamped, means that the degrees of freedom (d.o.f) at the vicinity of the clamped surface are reduced, which leads to a wrong representation of the stress and deformation state. However, by using Saint-Venant's principle [Dym and Shames, 2013], the resultant optimization obtained from the first case is overlapped with the one obtained from the second case. In this way, the parts considered for the final result are far from the clamped surfaces and the merged result is more accurate.

Topology optimization results

All topology optimization results and iterations are detailed in appendix A. Among all the described results, two optimized geometries are worth analyzing.

On the one hand, information about the optimum material distribution for the rear part of the chassis geometry is obtained from figures 2.9 and 2.10.

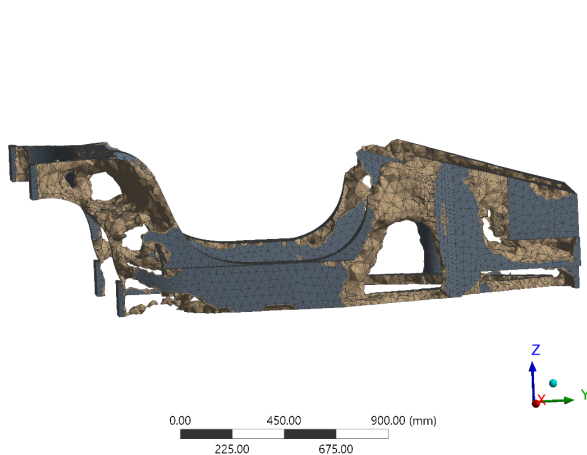


Figure 2.9. Optimized material distribution for case 1. View one.

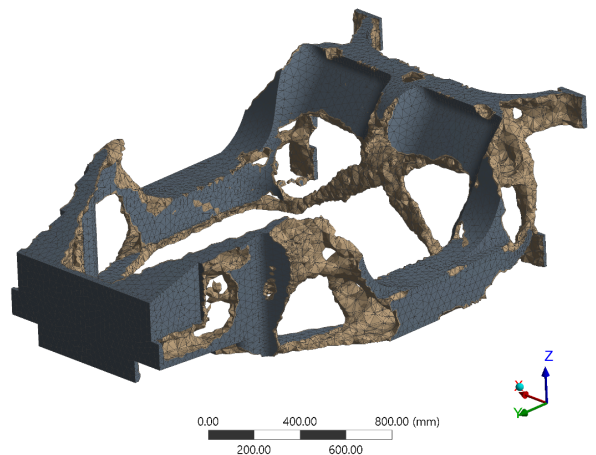


Figure 2.10. Optimized material distribution for case 1. View two.

The optimum geometry shown in the previous figures, is obtained for load case 1. Therefore, only the rear half of the geometry is analyzed. As it is shown, the main central beam behind the seats, turns out to be hollow (2.9). Thus, the outer shell is the principal part contributing to the overall torsional stiffness. Moreover, the side beams become hollow as well (2.10). On the other hand, from case 2, information about the front half of the chassis is obtained when

topology optimized. Thus, figure 2.11 shows the optimum material distribution when topology optimized for torsional stiffness.

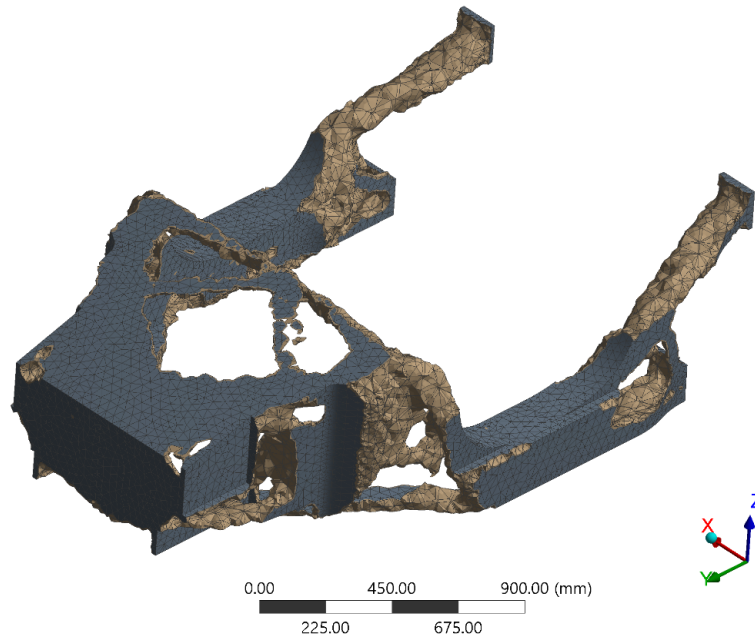


Figure 2.11. Optimized material distribution for case 2.

As can be appreciated in figure 2.11, the top front cover (lid) of the chassis, can be cut which is, in fact, a good result because a hole for the battery and the trunk is needed from a design perspective. Moreover, the side beams are confirmed to be hollow, and the rest of the front half of the chassis remains almost untouched as a single surface.

2.4 Surface geometry

Section (2.3), together with the defined available geometry, give the needed structural information to make the first shell design of the chassis. Figures 2.12 and 2.13 show the initial shell geometry used as a base for the iterative stiffness design.

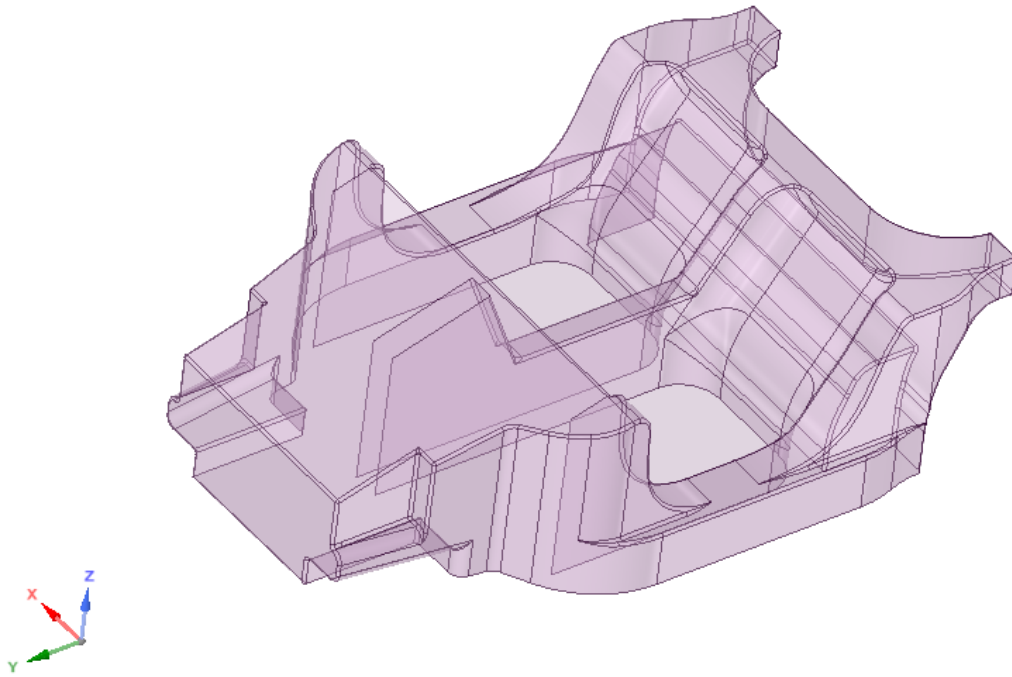


Figure 2.12. Surface geometry. View 1.

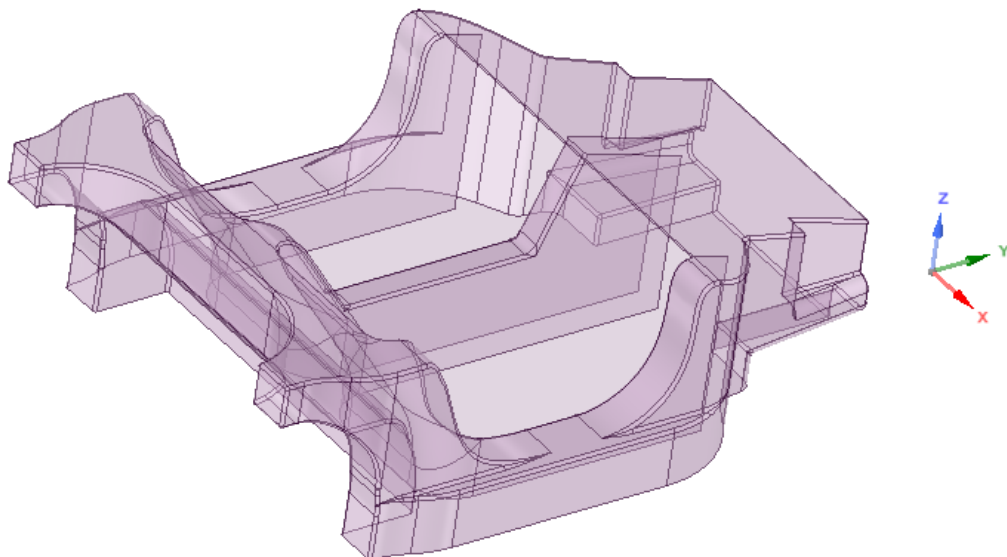


Figure 2.13. Surface geometry. View 2.

2.5 Mechanical model (FE)

The chassis is designed for stiffness, which means that a required minimum stiffness value is set. In automotive industry, the performance of the chassis when driving the car is usually measured

through the torsional stiffness.

Torsional stiffness

The torsional stiffness is defined as the torque per radian twist. In this case, since the aim is to compare with existing cars in the market, the units used are Newtons times millimeter divided by the twist angle in degrees. High stiffness cars such as the BMW Z4, have a torsional stiffness of around 40000 Nm/deg. The desired value, given by the company, Agile Automotive is 20000 Nm/deg for the design of the Agile SC122. Thus, the stiffness target is established for the iterative design process.

To calculate the torsional stiffness of the chassis, the front is clamped and the torsional force is applied at the rear ends. Figure 2.14 shows the representation of the procedure used to obtain the stiffness values. The force applied is represented as a coupled anti-symmetric force, F .

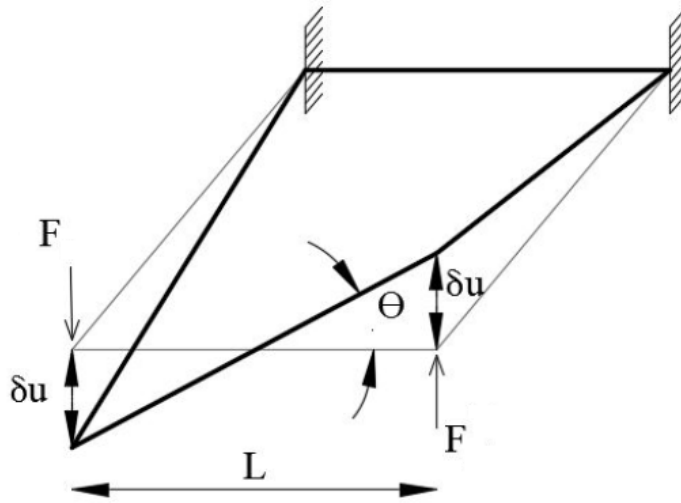


Figure 2.14. Torsional stiffness representation.

The total torsional stiffness of the system (K_t) is equal to the torque (T) divided by the angle (θ) as shown in equation 2.3. Where L is the width of the rear of the chassis and δu is the displacement of the node which more displacement suffers in the vertical direction. Equations 2.1 and 2.2 calculate θ and the torque respectively.

$$\theta = \arctan \left(\frac{\delta u}{0.5L} \right) \quad (2.1)$$

$$T = 0,5L(2F) \quad (2.2)$$

$$K_t = \frac{T}{\theta} \quad (2.3)$$

Thus, the presented analysis model for torsional stiffness is used in the finite element model of the chassis.

Applied torque

Figure 2.15 shows the mechanical model used for the iterative design process, where an anti-symmetric force of 10000N is applied at both ends of the rear of the chassis, while the farthest front surface is clamped.

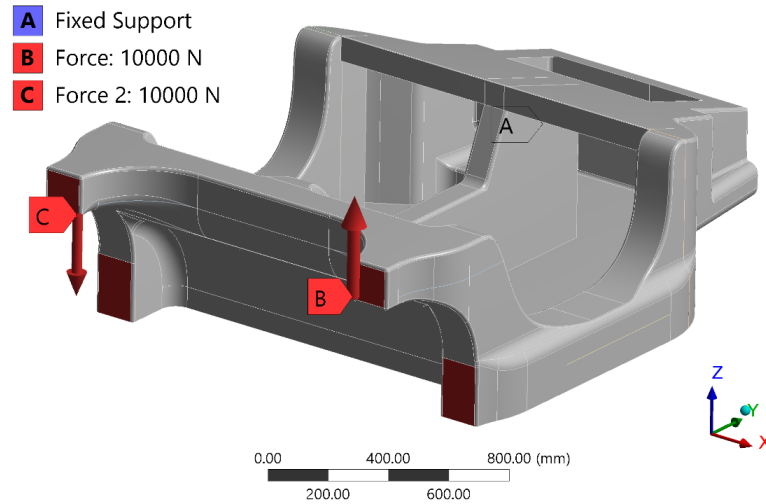


Figure 2.15. Torsion forces applied to calculate stiffness.

Material

The chassis has to be designed with carbon fiber, due to the philosophy of the company collaborating in the present thesis. However, to obtain the optimum geometry, an isotropic material can be used. In this way, by using aluminum, it is ensured that the final design in carbon fiber will have a better ratio mass-stiffness than the aluminum design. Thus, for the optimization of the shell geometry, aluminum 6061 T6 is used.

Mesh

Along the design process of the geometry, a mechanical model is set up. The loads are defined above and the mesh is shown in figure 2.16.

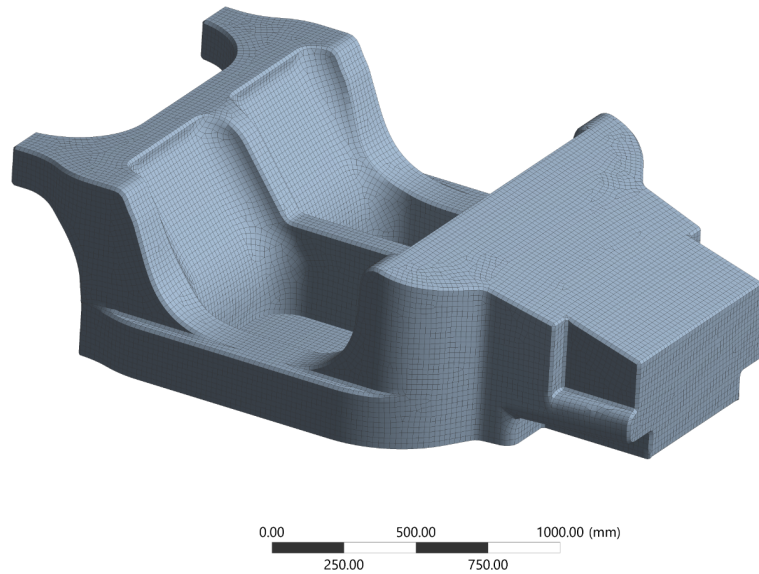


Figure 2.16. Torsional stiffness representation.

- Element type: Shell 181 Quads (4 nodes and 6 d.o.f per node)
- Number of elements: 33268
- Number of nodes: 33607

A model with quadratic elements SHELL 281 is compared with the linear model used. The distortion in the displacements due to the shear locking of linear elements, turns out to be a difference of less than a 1% error. Therefore, in order to make faster calculations linear elements SHELL 181 are used.

Mesh quality

A convergence study is performed to ensure that the mesh is compatible, so no overlaps or holes are present in the model. Figure 2.17 plots the total deformation for the mechanical model previously described.

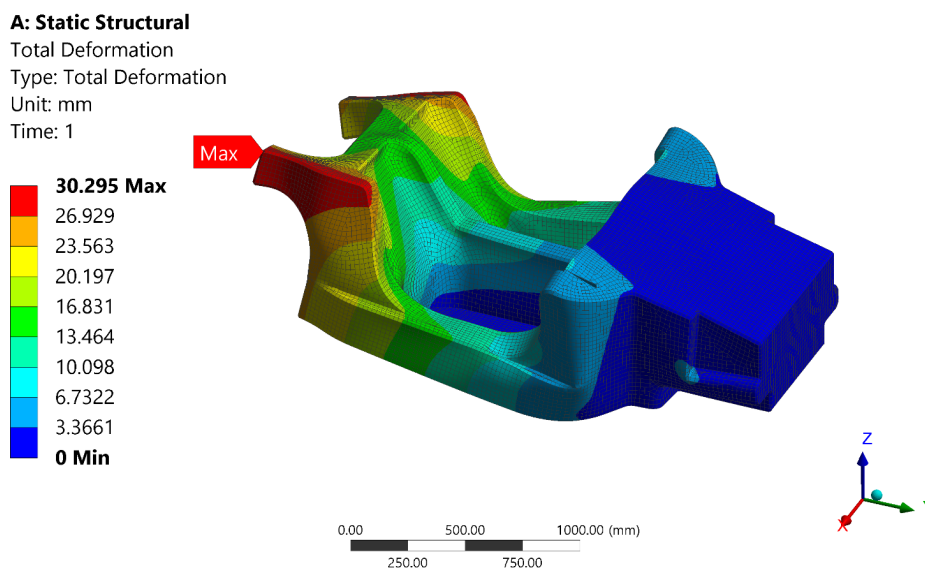


Figure 2.17. Total deformation (mm).

The graph shown in figure 2.18 confirms that the displacements converge when refining the mesh, which means that displacements are realistic.

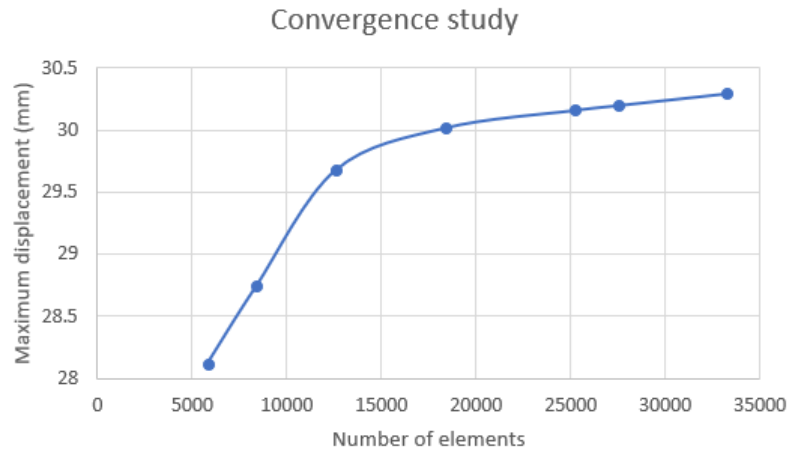


Figure 2.18. Mesh convergence study.

Another tool to ensure that the quality of the elements is optimum is the Jacobian ratio. According to [Cook et al., 2001] the Jacobian ratio is a measure of the distortion of an element from a perfect shape element. The Jacobian ratio varies from -1.0 to 1.0, where 1.0 is a perfect shape element.

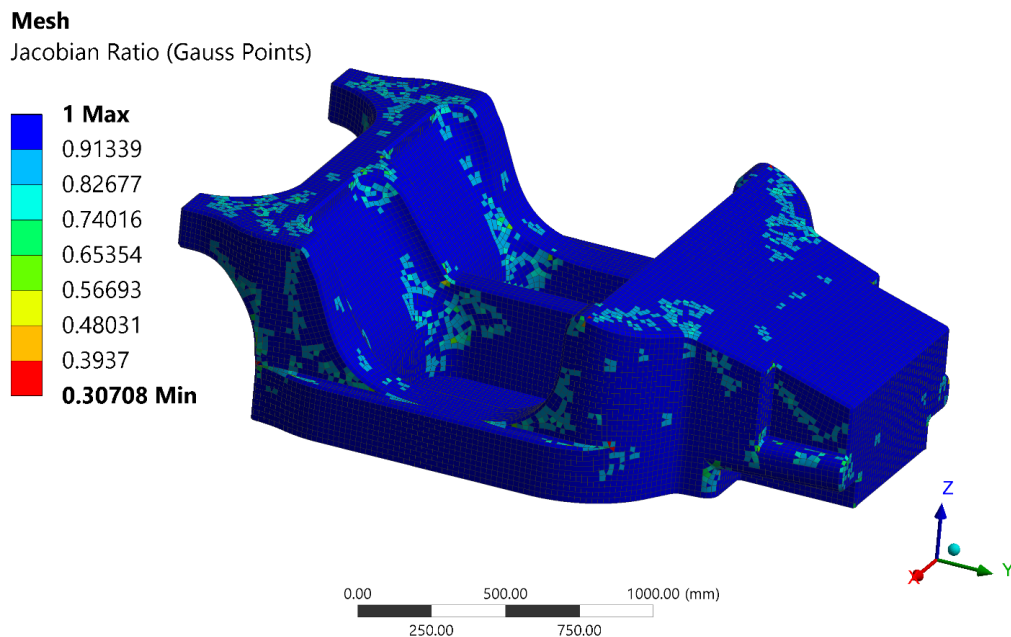


Figure 2.19. Jacobian ratio.

Figure 2.19 shows the plot of the Jacobian ratio for the current mesh. As it is shown, the minimum value of the Jacobian ratio is 0,3. Thus, together with the convergence study, the elements and mesh are validated.

2.6 Iterative design for stiffness

From the previous model, maximum displacement in Y direction at the rear end of the chassis is used to obtain the torsional stiffness as it was explained in subsection 2.5. The design has to fulfill the mass and stiffness requirements for the car performance. The required stiffness is 20000 Nm/deg and the desired mass, imposed by the company is 80 kg. Since the material used is aluminum instead of carbon fiber for the geometry design, a relevant margin is established. Therefore, the criteria for the iterative design process is to increase the stiffness while keeping the mass to 7 kg. Thus, if the desired torsional stiffness and mass are achieved using aluminum, it is ensured that when the design is made in carbon fiber, the ratio mass-stiffness is going to improve. Mass is kept to its required value by modifying the thickness of the aluminum shell.

The current first iteration for the geometry design has a mass of 77,9 kg while the torsional stiffness is 6580 Nm/deg. The stiffness target is still far from the needed one. Therefore, an iterative modification and optimization of the existing geometry is performed. Deformations in X, Y and Z are analyzed. Local bending due to thin walls is checked and improved. For this purpose, the strain energy density, which is the strain energy per unite volume of the elements, is minimized. More information about strain energy density can be found in [Dym and Shames, 2013]. It is an accurate tool to see where local stiffness has to be improved in order to produce an enhancement in the overall geometry.

Based on directional deformations and strain energy density, the iterative optimization design is performed, and the results are shown in table 2.1.

Iteration	Mass (kg)	Maximum "Y" disp. (mm)	Torsional stiffness (Nm/deg)
1	77,9	26,8	6580
2	78	16,389	10756
3	77,2	12,942	13620
4	76,8	13,18	13374
5	78,3	11,26	15655
6	83,7	10,5	17044

Table 2.1. Design iterations. Detailed in appendix B.

The whole iterative design process is detailed in appendix B, which is a self-contained document, not included in the main report due to its extension.

The final results shown in the table above for iteration 6, are obtained by introducing geometry changes and new components. This modifications are described below and the numbers in the parenthesis refer to figure 2.20.

- Corner smoothing. Corners and changes in the geometry are softened in order to avoid stress concentrations, that can produce local bending of the face sheets.
- Front shear webs (1). At the front sides of the chassis, shear webs are introduced to stabilize the face sheets and avoid buckling of the faces.
- Side shear webs (2). Two side shear webs are introduced at each side of the chassis with the purpose of getting stiffer side beams by keeping the distance of the face sheets.
- Rear shear web(3). Another shear web is added along the whole rear width of the chassis with the same purpose of the previous ones.
- Front firewall (4). The front firewall produces a closed area which increases the stiffness of the chassis.

- Central beam, height reduction. The height of the central beam of the chassis, which is placed in between the two seats is reduced, so that its stiffness is increased.
- Seat beams (5). Two beams are added on the floor of the car in the width direction of the chassis. These beams are placed to have a strong support for the seats, plus they add overall stiffness to the chassis.

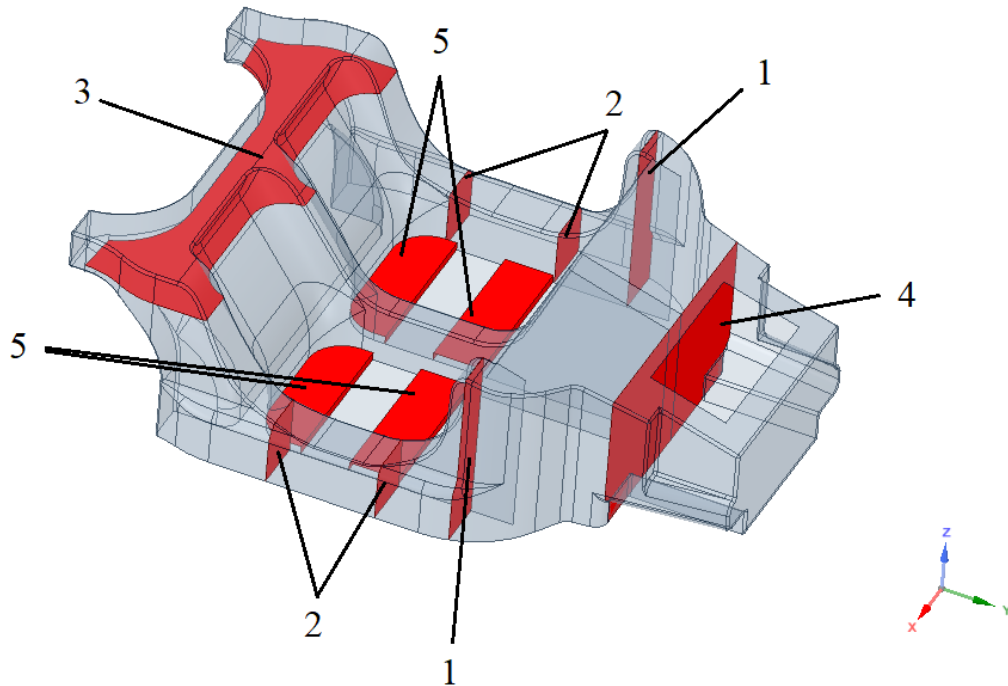


Figure 2.20. Added chassis components to improve stiffness.

A final chassis geometry is now defined with a torsional stiffness of 17000 Nm/deg and approximately 80 kg of mass in aluminum. The design ensures that the desired stiffness and mass can be reached, once it is made in carbon fiber. The final outer geometry is shown in figure 2.21 and 2.22.

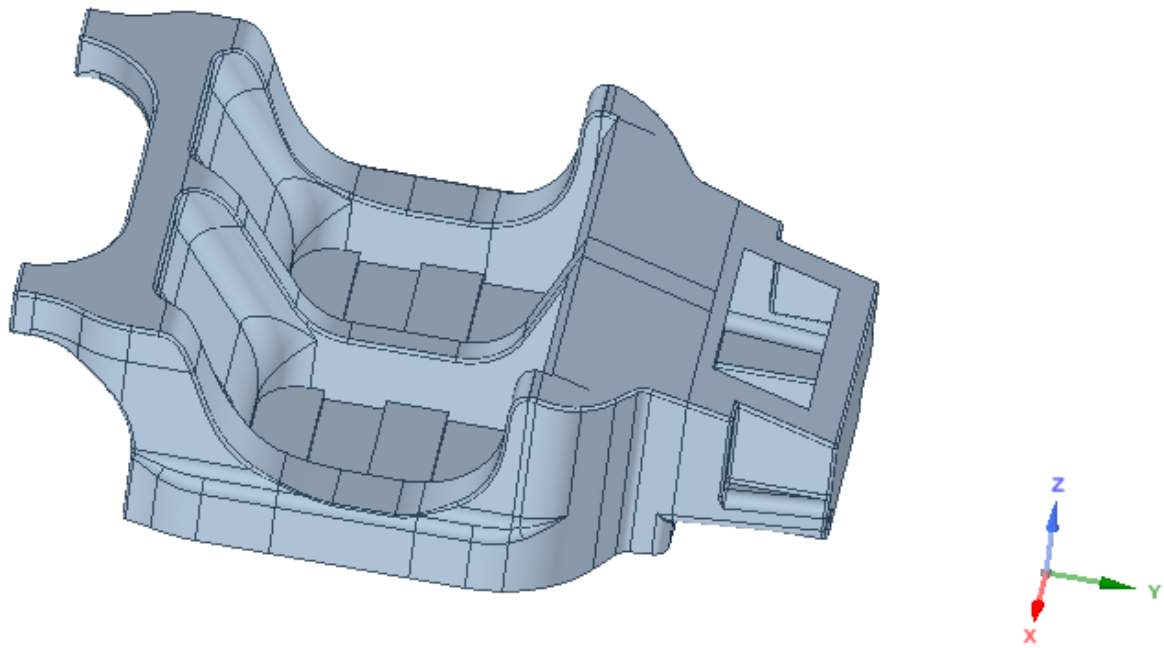


Figure 2.21. Final chassis geometry.View 1.

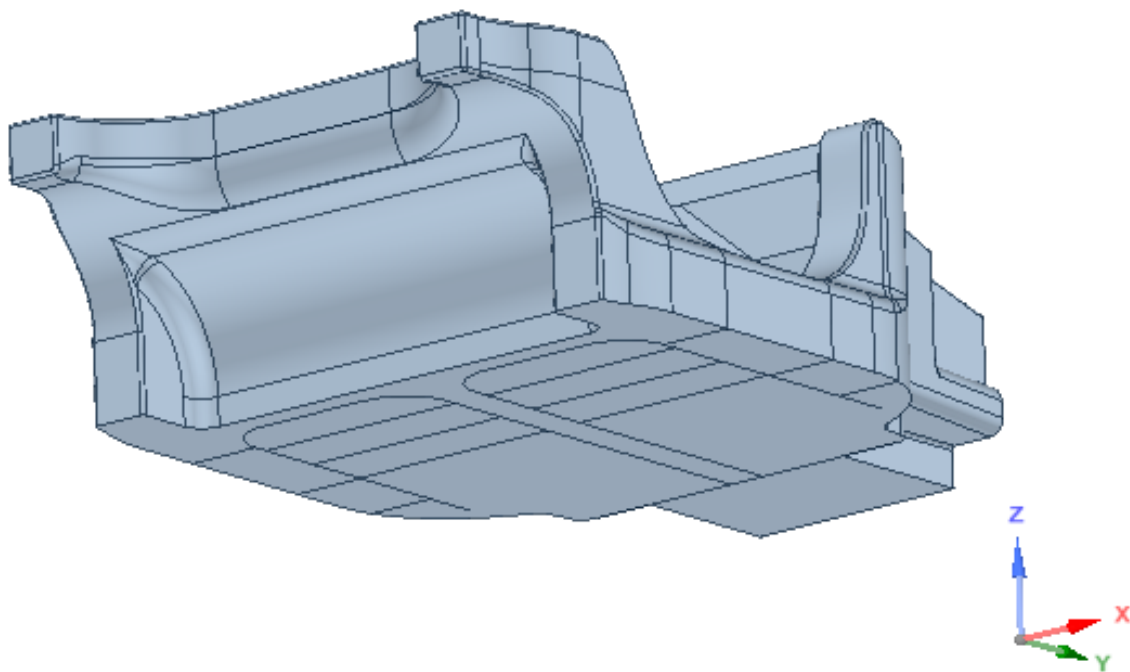


Figure 2.22. Final chassis geometry. View 2.

2.7 Strength validation

The real strength validation has to be made with the final material which has to be carbon fiber. Since that part is not included in the present thesis, a strength test is performed for the aluminum design. The purpose of this strength study is to search for possible geometry stress concentrations.

Mechanical model

From previous calculations from the company and from the author's work in the third semester of the MSc. at Aalborg University, the maximum vertical load obtained acting on the wheels of the car is 4000N when cornering. Since the aim of the present thesis is more focused on the adhesive joints than in the final strength of the chassis, which has to be made in carbon fiber, an extremely over sized load is used to make a rough strength estimation of the chassis geometry. Therefore figure 2.23 and 2.24 show the boundary conditions chosen. A couple of anti symmetric forces are applied at the rear end of the chassis (2.23) with a value of 20000N. Moreover, the front surface of the chassis is clamped. Thus, all d.o.f. are locked (2.24).

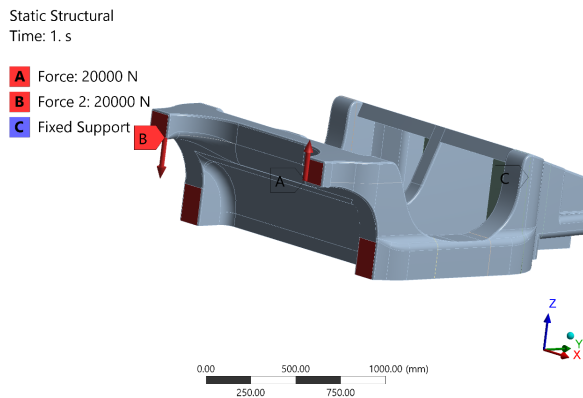


Figure 2.23. Boundary conditions. Loads.

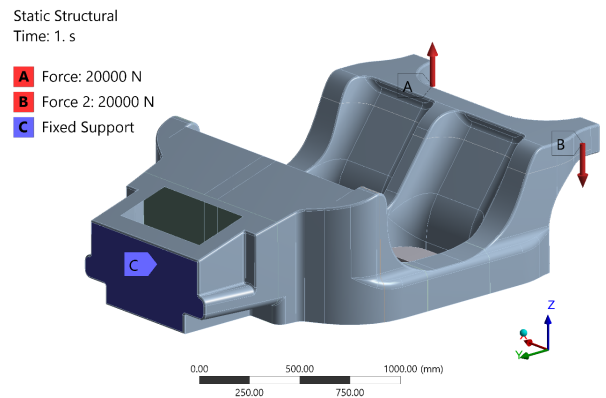


Figure 2.24. Boundary conditions. Fixed surfaces.

A uniform mesh of shell elements is used as shown in figure 2.25

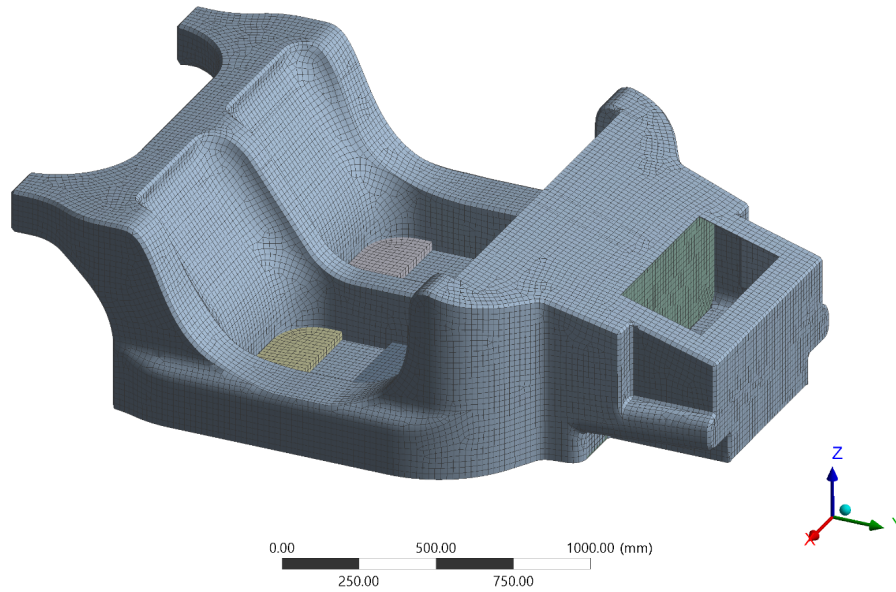


Figure 2.25. Chassis mesh.

- Element type: Shell 181 Quads (4 nodes and 6 d.o.f per node)
- Number of elements: 34056
- Number of nodes: 34385

Strength results

The failure criterion used is von Mises [Dym and Shames, 2013] criterion for isotropic materials. The yield strength of the material chosen which is Aluminum 6061 T6, is 276MPa. Figure 2.26 plots the von Mises stresses along the chassis geometry for the described load scenario.

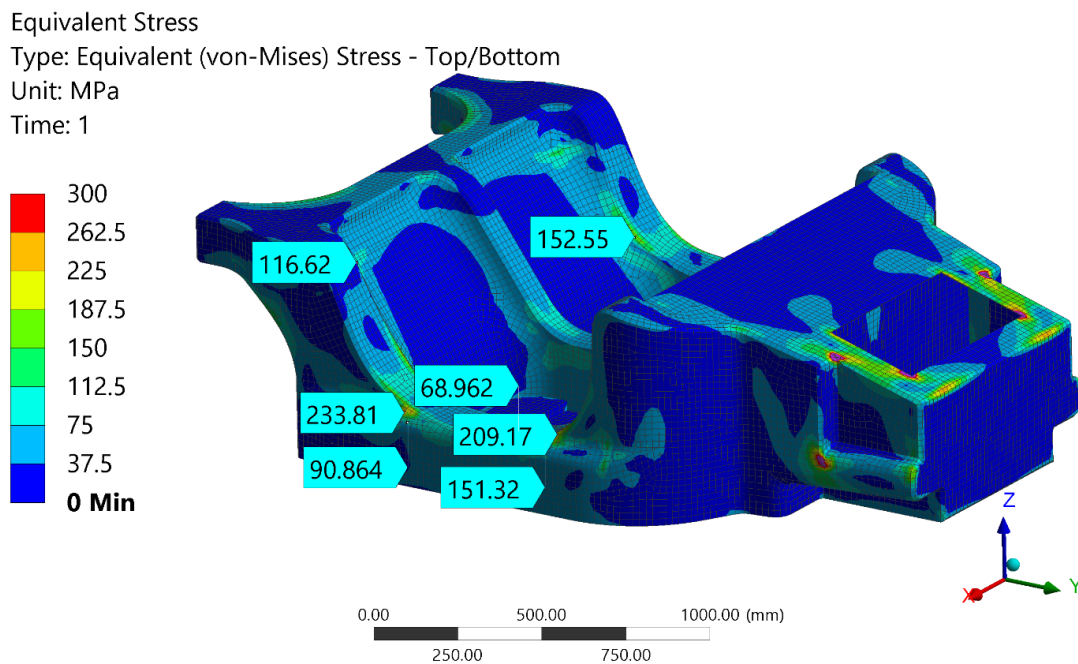


Figure 2.26. Von Mises stresses.

As it is shown, for an extremely over sized load applied, the aluminum chassis seems to be

already strong. The equivalent stresses are not bigger than the yield strength of the aluminum except some stress singularities which are concentrated in the front corners of the chassis. When the mesh is refined, the stresses at those red areas go to infinity. Therefore, they are treated as stress singularities. Nevertheless, the final design has to be made in carbon fiber so an equivalent stress state improved is expected to take place. The reason why the strength of a geometry designed for stiffness is so good, is because when designing for stiffness, the geometry is usually over dimensioned.

From the geometry design aspect, the chassis is ready to place the layup and optimize it with more accurate boundary conditions, but that is not covered in the present thesis.

Material research.

Thermoplastic 3

The current chapter describes the research process made about thermoplastic resin for infusion. Thus, the aim of the work done in this chapter is to obtain a material which can easily be manufactured in comparison with the common thermoset resins while offering similar mechanical properties.

3.1 Thermoplastic vs thermoset

The company in collaboration with the present thesis, Agile Automotive, uses thermoset resin for infusion as their manufacturing method. The materials used are epoxy and carbon fiber, which together offer high stiffness and strength properties while the density is lower compared to steel or aluminum. One of the main issues when designing with composite materials and in this case, with thermoset resin for infusion, is the need for having adhesive joints. The idea of making research about the thermoplastic resin is the possibility of welding instead of using adhesive. The advantages of the thermoplastic resin, if similar mechanical properties are achieved, are:

- Fully recyclable
- Low viscosity for infusion
- Possibility of welding
- High toughness (better for impact)

But before getting deeper with the mechanical comparisons of the thermoplastic with the thermoset resins, the processing has to be feasible and the A-surface of the parts must have a good quality since most of the parts in a car are going to be visible.

3.2 Processing feasibility

A sample batch is obtained from the company Arkema of their thermoplastic resin for infusion. The resin is Elium 188 XO. The technical data sheet can be found in appendix C. The resin is a liquid thermoplastic which needs a peroxide to react and start curing. In this case, by recommendation of the supplier, the peroxide is a powder version to avoid water in the solution, because the thermoplastic resin is pretty sensible when being in contact with water and it can foam up. The peroxide used is Perkadox CH-50X from the company AKZONOBEL and the TDS can be found in appendix D.

Processing times

In order to verify the processing times such as the pot life and the curing time, a 700ml bucket is used. When mixing the peroxide with the resin, the amount of peroxide must be between 3% and 4%. The temperature when mixing has to be room temperature and the mix must be done energetically during at least one minute. Therefore, 100g of Elium are mixed in the bucket with 3,4g of peroxide. The results obtained are shown in table 3.1.

Time	Temperature (°C)	State
15 : 15	<i>Roomtemp</i>	<i>mixed</i>
15 : 17	15	<i>liquid</i>
15 : 30	17	<i>liquid</i>
16 : 10	22	<i>liquid</i>
16 : 12	25	<i>liquid</i>
16 : 14	31	<i>liquid</i>
16 : 16	35	<i>liquid</i>
POT LIFE		
16 : 20	40	<i>liquid</i>
16 : 22	50	<i>liquid</i>
16 : 25	70	<i>foam</i>
16 : 26	80	<i>foam</i>
16 : 30	65	<i>solid</i>
16 : 38	56	<i>solid</i>
16 : 45	40	<i>solid</i>

Table 3.1. Processing times Elium 188 XO.

Figure 3.1 shows the final result obtained from the current test.

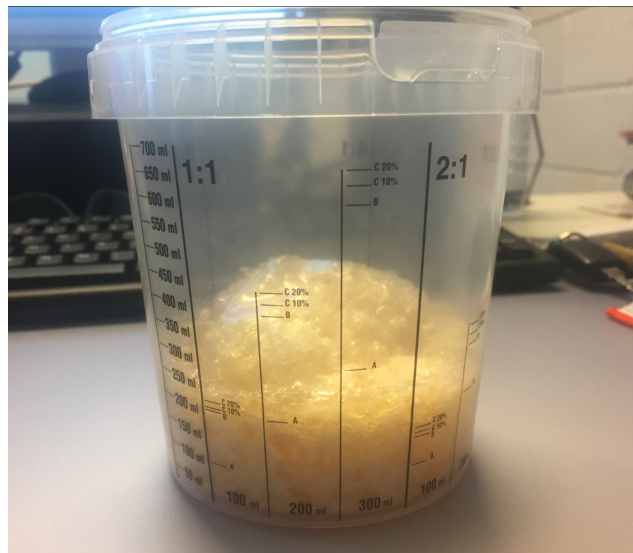


Figure 3.1. Elium processing test.

From the table, good conclusions are obtained. The pot life is around one hour, which allows for flexibility when producing parts. However, the picture of the bucket when fully cured shows a foamed shape. This is due to the contact with humidity in the air. Therefore, when producing

parts with Elium, no leaks in the infusion process have to be found. Otherwise, possibility of foaming may appear.

3.3 Manufacturing test of thermoplastic laminate

Carbon fabric choice

When choosing resins for infusion, one of the critical parameters to take into account is the sizing of the fibers. Depending on the kind of resin used, a different sizing may produce better results. The sizing is a chemical treatment for the fibers to give them the ability to bond to the resin. Therefore, if the right sizing is chosen, a perfect fiber-matrix bonding is obtained. In this case, the company Arkema (resin supplier) recommends to use thermoplastic sizing or vinyl-ester sizing. Thus, the chosen fabric to perform the tests is, Chomarac ([Chomarac, Carbon fabric]), C-WEAVE 600T 12k HS F0E (Sizing for thermoplastic resin).

Resin infusion process

Now a days, most of the high quality composite parts regarding structural properties are manufactured with prepreg using an autoclave. However, the resin infusion process, shown in figure 3.2, is a cheaper technique while if well done, it can offer good structural properties.

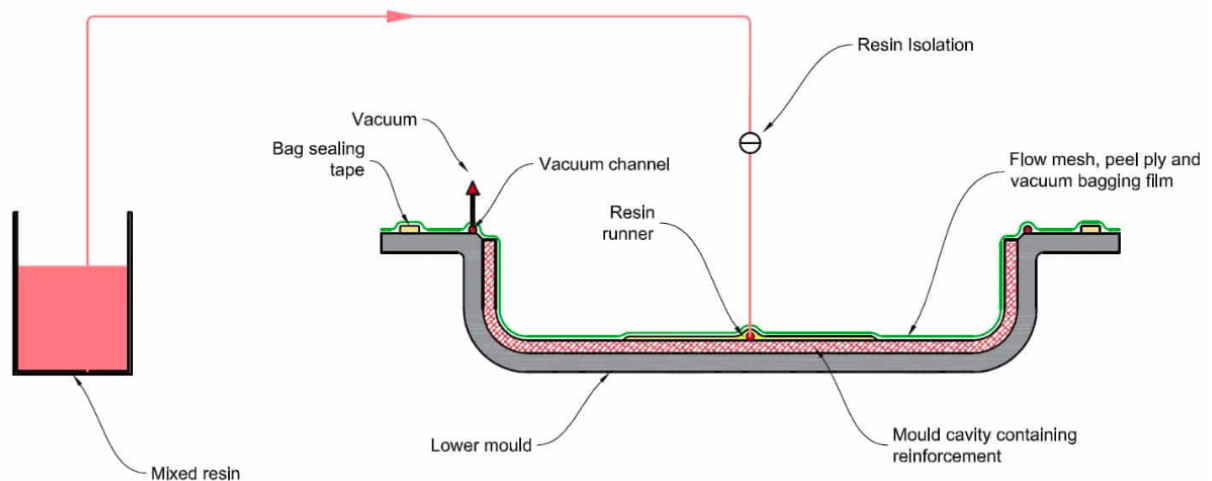


Figure 3.2. Resin infusion process [CI, Composite Integration].

Dry fibers are placed on the mold. A flow mesh is set on top with a peel ply if needed to get a rough surface in case of further bonding. A vacuum bag is placed on top and completely bonded to the mold with sealant tape. To perform the infusion, vacuum lines are placed in the mold with the respective inlet. The resin goes through the fibers helped by the vacuum line. When the fibers are completely wet, the inlet is closed and the vacuum is kept until the part is fully cured.

For the present tests done at Agile Automotive, the setup is made as shown in figure 3.3. To ensure a good infusion of all the fibers, the gap between the infusion mesh and the lay-up must be 25mm.

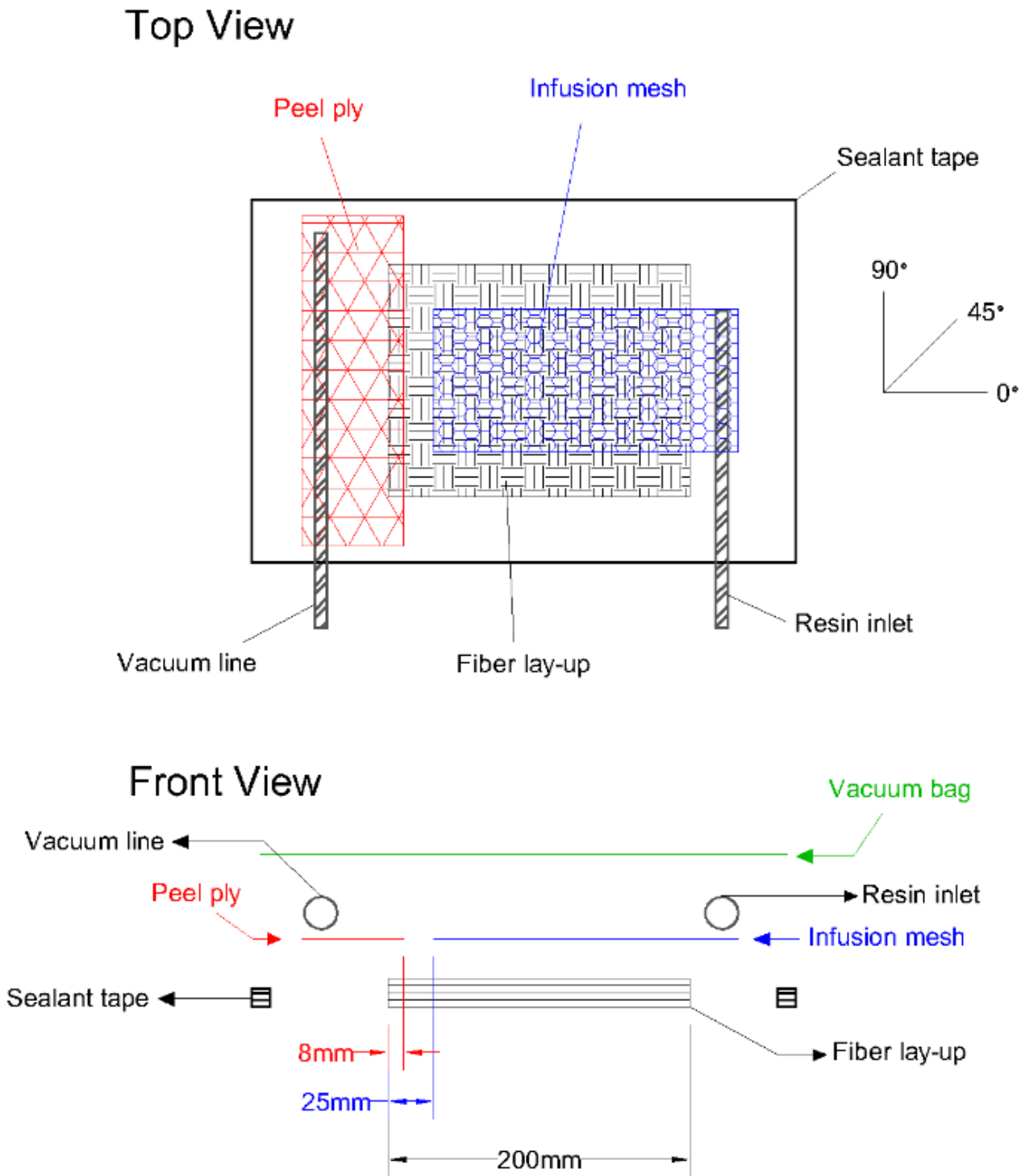


Figure 3.3. Resin infusion setup.

The present set-up excludes the use of perforated film because the used infusion mesh has already a bottom layer, which makes sure of splitting the resin from the rest of the tooling.

Laminate test

According to the previous process description, a first test is infused. The material and process are described previously and the stack-up sequence is $(0, 90)_2$. In this case it is two plies of the described twill fabric. A capture of the physical setup is shown in figure 3.4.

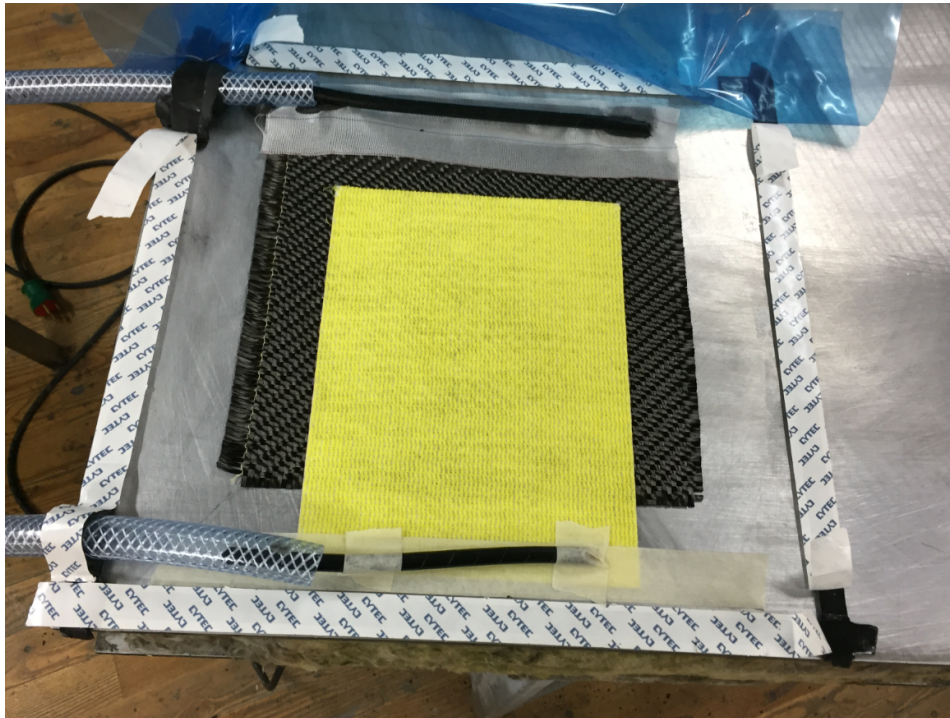


Figure 3.4. Test manufacturing setup.

After respecting the processing times obtained in the previous sections, the laminate is demolded and the infusion seems to have been good except for surface quality problems that can be observed in figure 3.5.



Figure 3.5. Laminate test 1.

From the picture, it looks like there are some holes in between the fibers. There are many variables which can produce such a bad quality and they are checked in the next section. If

the final quality of the composite is at it is shown for the first test, the use of thermoplastic reinforced polymer is not an option for the chassis design of the Agile SC122 since many parts of the chassis are visible. Moreover, these small holes on the A-surface of the part can be a structural issue from a fatigue point of view since they are potential unstable cracks.

3.4 A-surface quality

Before discarding the use of thermoplastic composite, the different variables during the manufacturing process are investigated in this section. A series of tests with different variables setup are made based on experience and brainstorming with the company engineers. All the tests follow the same manufacturing setup described before. All test specimens are physically accessible so that only a few pictures are included in the present report.

Appendix E details the steps followed for the different manufactured tests. The variables which can have an effect in the surface quality of the infused parts are:

- Vacuum infusion level
- Gelcoat and release agent used
- Type of fabric used
- Infusion speed (too much mesh)
- Resin quality

Thus, after trying to modify all possible infusion variables, the results are shown in table 3.2. TP refers to thermoplastic and TS to thermoset. The surface quality is defined from 1 to 5, being 5 the best quality that a thermoset epoxy resin can achieve. The vacuum level is indicated for the infusion period and for the post-processing step in the table, that is the reason to show the two values.

Test	Lay-up	Sizing	Vacuum	Mesh	Release/gelcoat	Quality
1	2xTwill/12K 600g	TP	100%/60%	Full mesh	Yes/No	2
2	2xTwill/12K 600g	TS	100%/60%	Full mesh	No/No	2
3	10xTwill/12K 600g	TP	100%/100%	Full mesh	Yes/No	2
4	10xTwill/12K 600g (dried)	TP	100%/60%	Full mesh	Yes/No	2
5	10xTwill/12K 600g	TP	100%/60%	Half mesh	Yes/No	3
6	10xTwill/12K 600g	TP	100%/60%	Full mesh	Yes/No	3
7	2xTwill/12K 600g	TP	100%/60%	No mesh	No/No	4
8	2xTwill/3K 600g+8g ply	TP	100%/60%	Full mesh	Yes	5

Table 3.2. A-surface testing.

No one of the variable modifications seems to obtain a good quality surface. Vacuum level, infusion speed or fabric type do not have an effect in the final quality surface. However, in test 7, instead of making the part in a mold, the laminate is infused in a plastic bag with plastic touching both surfaces. The original idea is to test if the release agent produces any chemical reaction when being in contact with the resin. Surprisingly, the small holes disappear as it is shown in figure 3.6.



Figure 3.6. Test 7.

The A-surface is completely continuous without any hole. However, it is seen shrinkage, so that the plastic bag has shrunk together with the resin.

Once the issue is localized a test is made on the glass table and it is, indeed seen that during the curing process the resin shrinks and creates the holes.

A solution is implemented in the test number 8 which is to use a first micro-ply of chopped carbon fibers which can stop the shrinkage while being transparent. Thus, a $8g/m^2$ carbon ply is used as it is shown in figure 3.7.



Figure 3.7. Shrinkage solution.

The result of the combined solution is a perfect A-surface as with thermoset resin like epoxy. The shrinkage can be appreciated a little bit but it is the same than with epoxy resins. Figure 3.8 shows the test number 8 where an excellent A-surface is obtained and therefore, the use of thermoplastic resin for the chassis design is now possible after solving the processing problem.

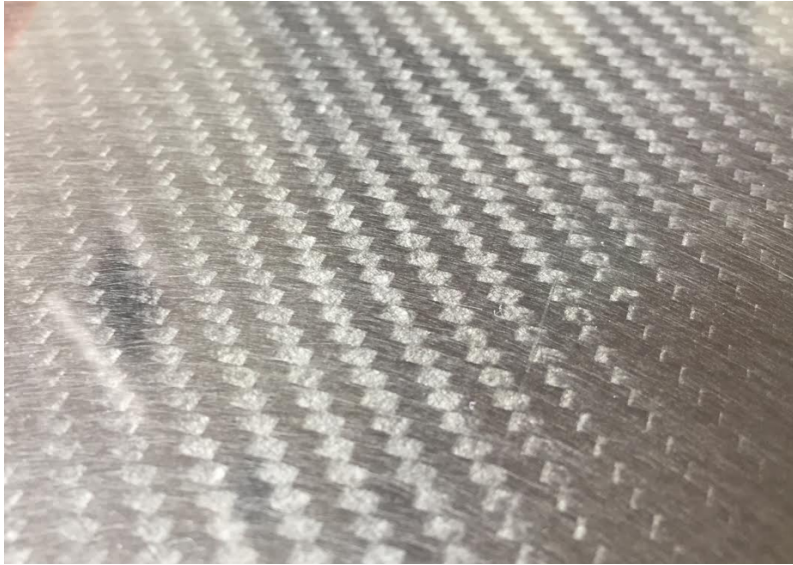


Figure 3.8. Test 8.

Material selection 4

Along this chapter, the mechanical properties of the two possible materials to choose, (thermoplastic and thermoset) are tested and as a result, the resin for the chassis design is chosen.

4.1 Inter laminar shear strength (ILSS)

An accurate mechanical test which can reveal the quality of a resin is the Inter Laminar Shear Strength test. The test is done according to [ASTM, D2344]. A thick and short carbon fiber specimen is subjected to a three point bending situation. Therefore, due to the thickness to in-plane dimensions ratio, an inter laminar failure occurs, which depends on the strength of the matrix material. Thus, the coupon test fails due to delamination.

Two resins are tested, the ordinary epoxy 900S from Bodotex and the innovative Elium 188 XO from Arkema.

Resin	Supplier	Density (g/cm^3)	Price (dkk/kg)	Viscosity (cP)
Bodopox 900S	Bodotex	1,16	60	850 – 950
Elium 188XO	Arkema	1,01	40 – 50	100

Table 4.1. Mechanical properties of the resins by [Bodotex, 900S] and [Arkema, Elium].

For each resin, a total of ten carbon fiber coupons are tested. The lay-up is given by the standard [ASTM, D2344] which in this case corresponds to ten plies of Chomarat ([Chomarat, Carbon fabric]), C-WEAVE 600T 12k HS F0E (Sizing for thermoplastic resin) for the thermoplastic ILSS test and the current twill fabric Toray *T300 12k (600gsm)* that Agile Automotive uses for the structural parts from Torey company [Toray, Fabrics]. The test must be done with unidirectional fabrics but since the sample obtained from Chomarat with the appropriate sizing is a twill, the one to compare with, has to be the same, so that even if the ILSS numbers are not the correct ones, its comparison is fair.

The set-up of the test is shown in figure 4.1.



Figure 4.1. ILSS test set-up.

The test is performed at Agile Automotive with an electric tensile test machine Lloyd LR100K, using a load cell of 100kN. The maximum load registered is the highest load achieved before it drops a 20%. In figure 4.2 it is shown the graph of one of the tests performed, where it can clearly be identified the load drop after inter laminar shear failure.

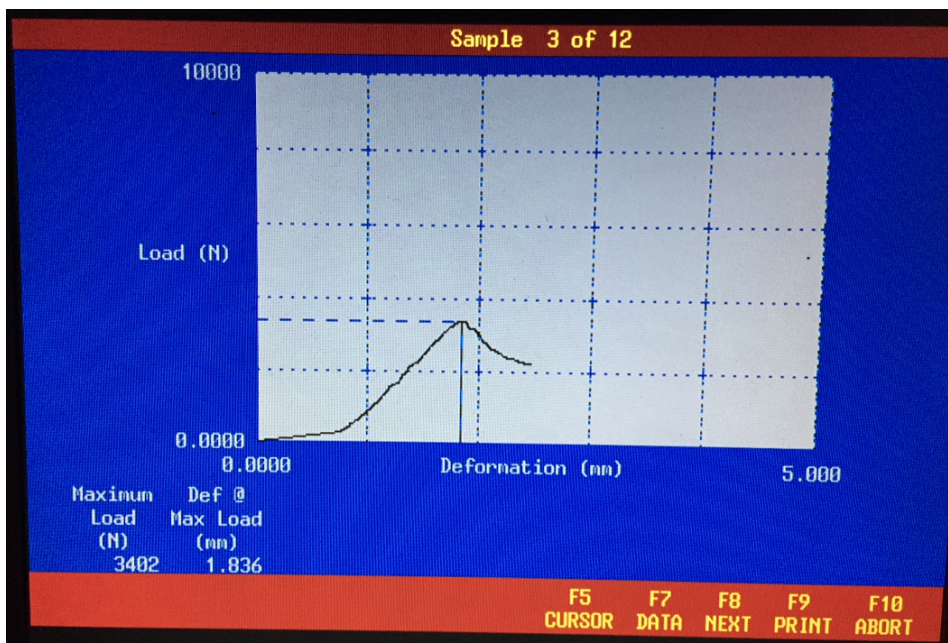


Figure 4.2. ILSS test graphic.

Once the maximum load is obtained, the ILSS is calculated by using the equation below (4.1).

$$ILSS = \frac{3P}{4tw} \tag{4.1}$$

Where P is the maximum load, t is the thickness and w the width. Dimensions are given in millimeters, the load in Newtons and as a result, the ILSS in MPa. Hereafter, the tables with the test results are detailed.

4.2 Thermoset ILSS

Epoxy 900S. Post-cured at 55°C

Coupon	Length (mm)	Thickness (mm)	Width (mm)	P (N)	ILSS (MPa)
1	44,65	7,42	15,38	7597	49,93
2	44,71	7,34	15,32	7844	52,32
3	44,67	7,28	15,45	7685	51,24
4	44,64	7,25	15,3	7770	52,54
5	44,67	7,33	15,31	7913	52,88
6	44,70	7,38	15,53	8025	52,51
7	44,61	7,37	15,23	7764	51,88
8	44,68	7,35	15,25	7887	52,77
9	44,58	7,5	15,2	7669	50,45
10	44,76	7,3	15,12	7309	49,66
Average	44,67	7,35	15,30	7746,30	51,67
Deviation	0,05	0,07	0,12	199,7	1,22
Variation %					2,35

Table 4.2. ILSS Epoxy 900S. Post-cured at 55°C.

Epoxy 900S. Post-cured at 100°C

Coupon	Length (mm)	Thickness (mm)	Width (mm)	P (N)	ILSS (MPa)
1	44,76	7,35	14,26	7186	51,42
2	44,83	7,35	14,33	6676	47,54
3	44,81	7,4	14,42	7407	52,06
4	44,88	7,35	14,33	6884	49,02
5	44,92	7,35	14,42	6446	45,61
6	44,66	7,27	14,38	6972	50,02
7	44,75	7,44	14,27	6854	48,42
8	44,85	7,3	14,02	6583	48,24
9	44,7	7,4	14,32	7351	51,99
10	44,89	7,45	14,27	6493	45,81
Average	44,78	7,36	14,30	6848,55	48,80
Deviation	0,10	0,05	0,11	348,97	2,35
Variation %					4,82

Table 4.3. ILSS Epoxy 900S. Post-cured at 100°C.

4.3 Thermoplastic ILSS

Elium 188 XO. Post-cured at room temperature

Coupon	Length (mm)	Thickness (mm)	Width (mm)	P (N)	ILSS (MPa)
1	37	6	13,1	3704	35,34
2	36,9	6	13	3899	37,49
3	37	6	13,1	3850	36,74
4	36,85	6	12,8	3271	31,94
5	36,85	6	13,65	3788	34,69
6	37,05	6	12,7	3402	33,48
7	37,05	6	13,05	3818	36,57
8	37	6	13,1	4056	38,70
9	37	5,95	13	3780	36,65
10	37	6	12,95	3907	37,71
Average	36,96	6,01	13,03	3747,5	35,9
Deviation	0,08	0,05	0,23	238,06	2,07
Variation %					5,77

Table 4.4. ILSS Elium 188 XO. Post-cured at room temperature.

Elium 188 XO Post-cured at 60°C

Coupon	Length (mm)	Thickness (mm)	Width (mm)	P (N)	ILSS (MPa)
1	37,75	6,1	13,85	4165	36,97
2	37,8	6	13,65	4041	37,01
3	37,85	6	14,05	4484	39,89
4	37,9	6,05	13,65	4093	37,17
5	37,8	6	14,8	4521	38,18
6	37,9	6,05	14,8	4302	36,03
7	37,75	6	14,7	4451	37,85
8	37,8	6	14,9	4386	36,80
9	37,8	6,1	13,8	3783	33,70
10	37,55	6	14,9	4383	36,77
Average	37,79	6,03	14,31	4260,9	37,03
Deviation	0,10	0,04	0,55	236,69	1,58
Variation %					4,26

Table 4.5. ILSS Elium 188 XO. Post-cured 60° C.

4.4 Results and material choice

The resultant inter laminar shear strengths obtained are shown in table 4.6.

Resin	ILSS (MPa)
Elium 188 XO. Post-cured at room temperature	37,01
Elium 188 XO Post-cured at 60°C	37,03
Epoxy 900S. Post-cured at 55°C	51,67
Epoxy 900S. Post-cured at 100°C	48,80

Table 4.6. ILSS Comparison.

Since the difference in strength is too much, having around 25% less inter laminar shear strength the thermoplastic resin, at this point the use of thermoplastic resin is discarded. There is no point in designing a chassis with a material which takes more work to produce with good surface quality while the mechanical properties are not close to the thermoset resins used in the company. Therefore, the resin selected to continue with the joints study is the Epoxy 900S from Bodotex, which together with Toray reinforcements is characterized in the following chapter.

Material characterization

5

By making use of micromechanics of composite materials, the parameters for the chosen material (thermoset epoxy) are obtained in an analytical form. The theory and calculations are presented in this chapter.

5.1 Micromechanics approach

The whole section is based on [Qu, 2006] and [Cook et al., 2001].

Micromechanics is the study of the interaction between the components of a composite material like fibers and matrix, when the material is considered homogeneous.

In order to create a macromechanical model of composite material, the properties of a lamina can be obtained through micromechanics of composite materials. There are two basic approaches to micromechanics of composite materials:

- Mechanics of materials approach
- Elasticity approach

In this chapter, only "mechanics of materials approach" is considered for the material characterization.

To obtain the material parameters of a lamina, some initial assumptions and restrictions are defined.

For the lamina:

- Stress free in the start
- Macroscopically orthotropic and homogeneous

For the fibers:

- Homogeneous and isotropic
- Regularly spaced
- Perfectly aligned and bonded

For the matrix:

- Homogeneous and isotropic
- Void free

The parameters to be obtained through the present method are the two elastic modulus E_1 and E_2 , the poisson's ratio ν_{12} and the shear modulus G_{12} .

Definition of E_1

The assumption of iso-strain (Voigt model [Qu, 2006]) is introduced. This means that for a lamina loaded in the direction of the fibers 5.1, the strain in the matrix and in the fibers is the same, so that the cross section remains straight.

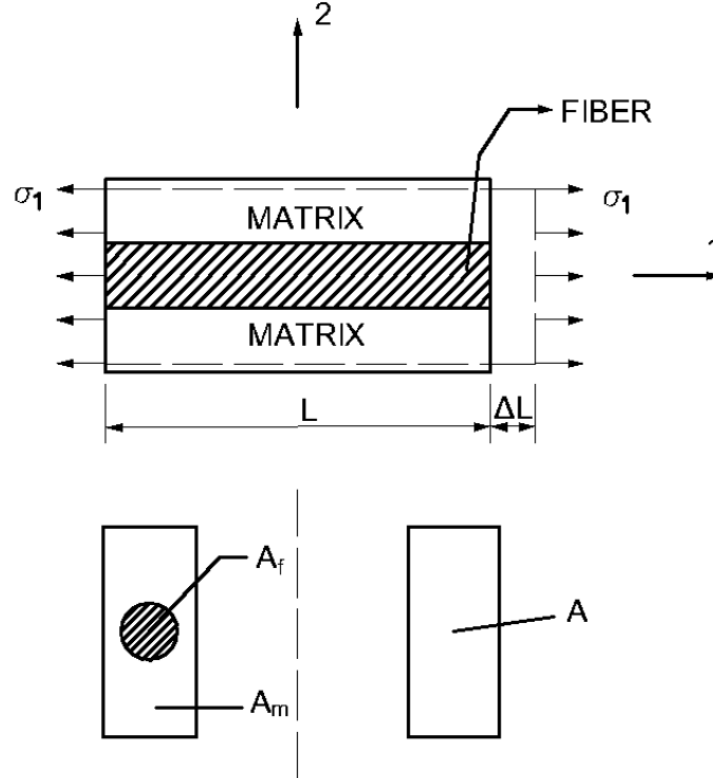


Figure 5.1. Loaded lamina σ_1 . Inspired by [Cook et al., 2001].

It is assumed that both phases of the lamina, the matrix and the fibers have different elastic properties. Thus, the elastic modulus of the fibers (E_f) and the elastic modulus of the matrix (E_m) are different as shown in expression 5.1.

$$E_f \neq E_m \tag{5.1}$$

Which means that due to the constitutive equation, which relates the strains (ε) with the stresses (σ) through the elastic modulus (E), the stresses are different for fibers (σ_f) and matrix (σ_m). Since the strain is considered to be iso-strain, from now, the strains (ε) are the strains in the loading direction which are the same for fibers and matrix. And in figure 5.1 the loading direction is 1, so the strains now are written as ε_1 .

$$\sigma_f = E_f \varepsilon_1 \tag{5.2}$$

$$\sigma_m = E_m \varepsilon_1 \tag{5.3}$$

From macromechanics it is known that the force (F) is equal to the stress (σ) times the area (A),

$$F = \sigma_1 A \tag{5.4}$$

but since the total stress over the whole surface which includes fibers and matrix is a combination of fiber stress and matrix stress as shown in equation 5.2 and 5.3,

$$F = \sigma_f A_f + \sigma_m A_m \quad (5.5)$$

where A_f and A_m are the cross section area of fibers and matrix respectively.

From macromechanics,

$$\sigma_1 = \frac{F}{A} \quad (5.6)$$

Therefore, by inserting equation 5.2 and 5.3 into 5.5 and all in once inserting equation 5.5 into 5.6, the resulting expression is,

$$\sigma_1 = \frac{E_f \varepsilon_1 A_f}{A} + \frac{E_m \varepsilon_1 A_m}{A} \quad (5.7)$$

From equation 5.7 the term ε_1 is taken as a common factor and passed to the left side of the equation,

$$\frac{\sigma_1}{\varepsilon_1} = \frac{E_f A_f}{A} + \frac{E_m A_m}{A} \quad (5.8)$$

where, the left term of the equation which relates the stress with the strain is the constitutive relationship, which is equal to the elastic modulus E .

Thus, if reordering the expression and introducing the new term (E), the final expression becomes:

$$E_1 = E_f V_f + E_m V_m \quad (5.9)$$

where V_f and V_m are the volume fractions of fibers and matrix respectively.

$$V_f = \frac{A_f}{A} \quad (5.10)$$

$$V_m = \frac{A_m}{A} \quad (5.11)$$

From equation 5.9, an expression to determine the elastic modulus E_1 is derived, depending on the individual properties of fibers and matrix. This expression is called "Rule of mixtures" by [Cook et al., 2001].

Definition of E_2

In this case to calculate the parameter E_2 an assumption based on the Reuss model [Qu, 2006] is introduced. The assumption is the homogenization of the stresses. Thus, iso-stress condition under loading. This assumption is valid for a lamina, loaded transverse to the fiber direction (5.2).

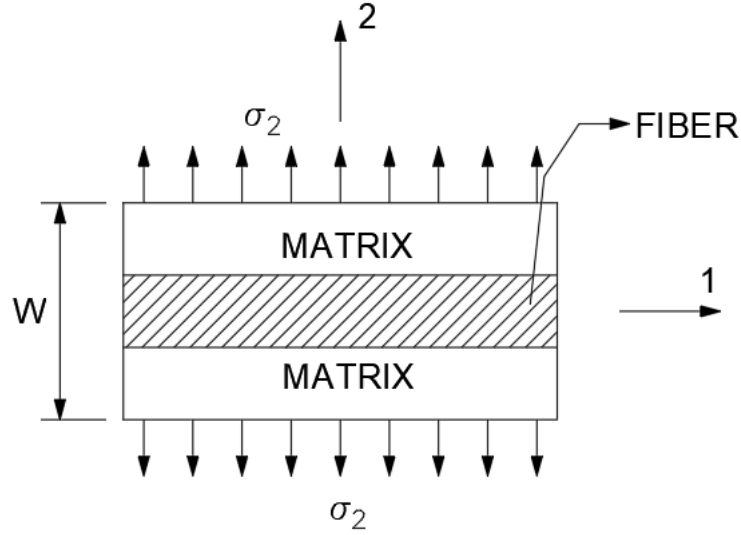


Figure 5.2. Loaded lamina σ_2 . Inspired by [Cook et al., 2001].

In contrast with the calculation of E_1 , now the strains are unknown and the stresses are the same for matrix and fibers (equations 5.12 and 5.13).

$$\varepsilon_f = \frac{\sigma_2}{E_f} \quad (5.12)$$

$$\varepsilon_m = \frac{\sigma_2}{E_m} \quad (5.13)$$

The load is acting now over the width (W). Therefore, the load is split proportionally for the fibers and for the matrix by using the volume fraction of fibers (V_f) and matrix (V_m) related to the width (W). So ε_f acts over $V_f W$ and ε_m over $V_m W$.

Thus the total deformation in direction 2 is given by equation 5.14.

$$\Delta W = \varepsilon_2 W = V_f W \varepsilon_f + V_m W \varepsilon_m \quad (5.14)$$

So the strain is then,

$$\varepsilon_2 = V_f \varepsilon_f + V_m \varepsilon_m \quad (5.15)$$

By inserting equations 5.12 and 5.13 into 5.15,

$$\varepsilon_2 = V_f \frac{\sigma_2}{E_f} + V_m \frac{\sigma_2}{E_m} \quad (5.16)$$

From macromechanics, the constitutive equation,

$$\sigma_2 = E_2 \varepsilon_2 \quad (5.17)$$

Thus, introducing equation 5.16 into equation 5.17, the following expression (5.18) is obtained.

$$\sigma_2 = E_2 \left(V_f \frac{\sigma_2}{E_f} + V_m \frac{\sigma_2}{E_m} \right) \quad (5.18)$$

Dividing by σ_2 and solving, an expression for calculating E_2 is obtained.

$$\frac{1}{E_2} = \frac{V_f}{E_f} + \frac{V_m}{E_m} \Rightarrow E_2 = \frac{E_f E_m}{V_m E_f + V_f E_m} \quad (5.19)$$

Definition of ν_{12}

The assumption taken in this case is the same than for calculating E_1 . Thus, iso-strain homogenization.

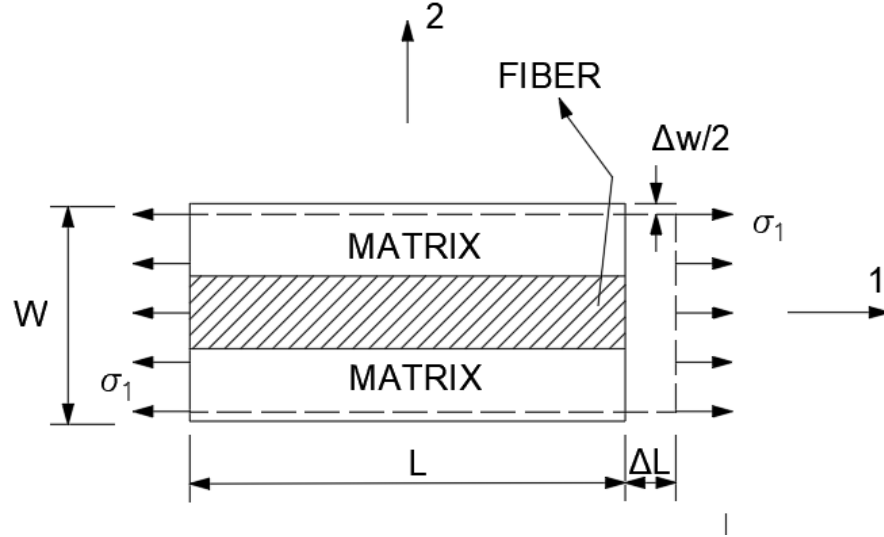


Figure 5.3. Loaded lamina σ_1 . Inspired by [Cook et al., 2001].

According to figure 5.3, and introducing the definition of Poisson ratio (ν_{12}) from macromechanics approach, the following expression is obtained.

$$\nu_{12} = -\frac{\varepsilon_2}{\varepsilon_1} \quad (5.20)$$

And the strain in the transverse direction to the fibers is, according to figure 5.3,

$$\varepsilon_2 = \frac{\Delta W}{W} \quad (5.21)$$

Therefore, equation 5.20 together with equation 5.21 yield to,

$$\Delta W = -W\varepsilon_2 = W\nu_{12}\varepsilon_1 \quad (5.22)$$

which, due to physical reasons is equal to,

$$\Delta W = \Delta W_m + \Delta W_f \quad (5.23)$$

If now the deformations are written in terms of volume fraction as it is done for calculating E_2 , the resultant expressions are,

$$\Delta W_m = WV_m\nu_m\varepsilon_1 \quad (5.24)$$

$$\Delta W_f = WV_f\nu_f\varepsilon_1 \quad (5.25)$$

If equations 5.22, 5.24 and 5.25 are now introduced into equation 5.23, the resultant combined expression is shown below (5.26).

$$\nu_{12} = \nu_m V_m + \nu_f V_f \quad (5.26)$$

The resultant equation 5.26 is called "Rule of mixtures" and it is used to calculate Poisson's ratio from a micromechanical approach.

Definition of G_{12}

The basic assumption introduced in this case is that the lamina is subjected to pure shear load as shown in figure 5.4, which means that fibers and matrix are dealing with the same load.

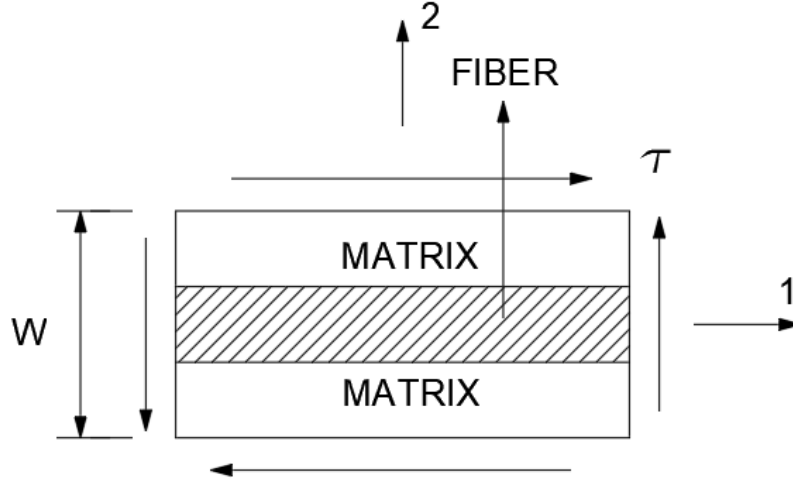


Figure 5.4. Shear loaded lamina. Inspired by [Cook et al., 2001].

It is known from macromechanics that the shear strains can be calculated from the stresses as shown in equation 5.27 and 5.28.

$$\gamma_m = \frac{\tau}{G_m} \quad (5.27)$$

$$\gamma_f = \frac{\tau}{G_f} \quad (5.28)$$

Where γ_m and γ_f are the shear strains for the matrix and for the fibers respectively, τ is the shear stress and G_m and G_f are the shear modulus of matrix and fibers respectively.

If the shear deformation is equally distributed for fibers and matrix as it was done for calculating the previous parameters, the following expression is obtained.

$$\gamma = V_m \gamma_m + V_f \gamma_f \quad (5.29)$$

If the same procedure as used for calculating E_2 is followed, the final expression is obtained.

$$\frac{1}{G_{12}} = \frac{V_f}{G_f} + \frac{V_m}{G_m} \quad (5.30)$$

If equation 5.30 is re-ordered, the final equation for calculating the shear modulus of a lamina is shown in equation 5.31.

$$G_{12} = \frac{G_m G_f}{V_m G_f + V_f G_m} \quad (5.31)$$

With the four parameters defined in this section, the material can be characterized to make a finite element model which according to the literature ([Cook et al., 2001]), is very precise.

5.2 Calculation of material parameters

Based on the theory described in the previous section, the material selected is now characterized. The two phases which, combined, yield to the composite material are:

- Resin. Bodopox 900S. Epoxy resin.
- Fabric. Toho Tenax UD STS Carbon fiber.

And the elastic properties given by the manufacturers are shown in table 5.1.

Material	E (GPa)	ν_{12}	G_{12} (GPa)
Epoxy 900S	10	0,33	2,4
UD Carbon	240	0,3	13

Table 5.1. Elastic properties of the phases.

Material properties of the carbon fiber fabric are obtained from [Sigmatech, Fabrics]. Epoxy properties are obtained from [Bodotex, 900S]. Only elastic modulus (E) is obtained from the manufacturer data sheets, while poisson's ratio (ν_{12}) and the shear modulus G_{12} are obtained from statistical data gathered from different sources. However some good approximations can be consulted in Michigan Technological University web page, [MTU, University]. From their studies, it seems like most of epoxy resins have the same poisson's ratio and shear modulus.

According to equations 5.9, 5.19, 5.26 and 5.31, the parameters for a lamina of UD carbon epoxy are calculated and shown in table 5.2. The fiber volume fraction obtained by the resin infusion process at Agile Automotive is 55% of carbon fiber. Thus, $V_f = 0,55$ and $V_m = 0,45$.

	E_1 (GPa)	E_2 (GPa)	E_3 (GPa)	G_{12} (GPa)	G_{13} (GPa)	G_{23} (GPa)	ν_{12}	ν_{13}	ν_{23}
UD	136,5	21,14	?	4,3	?	?	0,31	?	?

Table 5.2. Elastic properties of a UD lamina.

To make a finite element model, the rest of the parameters marked with question mark are needed. So their estimation is explained below.

Out of plane Young's Modulus

The parameter E_3 is mostly dominated by the resin Young's modulus. However, the thickness of the lamina is really small compared to the other in-plane dimensions when designing with composites. Therefore, the out of plane Young's modulus of the lamina is set to 5GPa which is a conservative value according to the matrix value.

G_{13} and G_{23}

It is extremely difficult to obtain these values, even through experimental methods. Theoretically, the out of plane shear stiffness (G_{13}) should be equal to the in-plane shear stiffness (G_{12}) which was calculated to be 4,3GPa. Therefore, in order to be conservative, both out of plane shear stiffness are set as 4GPa.

Out of plane Poisson's Ratio

From a micromechanical approach, for a UD lamina, the out of plane Poisson's ratio ν_{13} is equal to ν_{12} . To calculate the out of plane Poisson's ratio ν_{23} the following expression (5.32) is used:

$$\nu_{23} = 1 - \nu_{12} - \frac{E_2}{3K} \quad (5.32)$$

Where K is the Bulk modulus which is defined in equation 5.33.

$$K = \left(\frac{V_f}{K_{fibre}} + \frac{1 - V_f}{K_{matrix}} \right)^{-1} \quad (5.33)$$

And the bulk modulus of fibers and matrix is defined in equations 5.34 and 5.35.

$$K_f = \frac{E_f}{3(1 - 2\nu_f)} \quad (5.34)$$

$$K_m = \frac{E_m}{3(1 - 2\nu_m)} \quad (5.35)$$

Therefore, the out of plane Poisson's ratio ν_{23} is equal to 0,29.

Material characterization results

Table 5.3 shows the final calculated parameters which characterize the UD lamina that is going to be used for the next studies.

	E_1 (GPa)	E_2 (GPa)	E_3 (GPa)	G_{12} (GPa)	G_{13} (GPa)	G_{23} (GPa)	ν_{12}	ν_{13}	ν_{23}
UD	136,5	21,14	5	4,3	4	4	0,31	0,31	0,29

Table 5.3. Elastic properties of a UD lamina.

The calculated parameters are needed for the further joint strength analyses carried out in finite element software.

Identification of bonded joints 6

Along the present chapter, the chassis geometry is divided into substructures based on manufacturing feasibility. The critical joint of the assembly regarding failure is then identified and represented. A multi-scale approach is finally used to perform an optimum design of the adhesive joint.

6.1 Division of the chassis into sub-structures

The chassis geometry developed in chapter 2.4, is now divided into substructures to make it possible to manufacture. Therefore, the manufacturing requirements define the substructure design of the chassis. According to the resin infusion process which is the technique used at Agile Automotive, the geometry must not present negative angles and the corners have to be accessible for the technicians when placing the fibers. The main parts of the chassis are now shown in figure 6.2.

The chassis structure is divided into the following substructures:

- Lid
- Main part
- Floor
- Shear webs

The shear webs, shown in figure 6.1 are completely independent of the chassis structure and bonded.

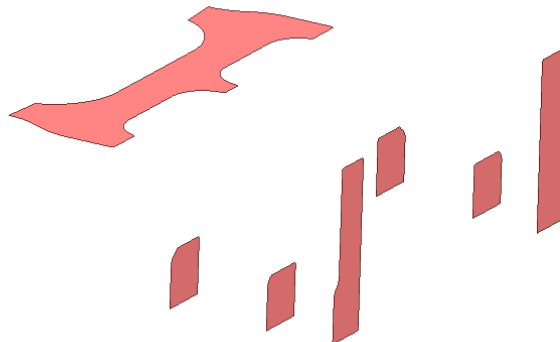


Figure 6.1. Shear webs.

The main structure is then divided into 3 parts as figure 6.2 shows. The main part, the lid and the floor.

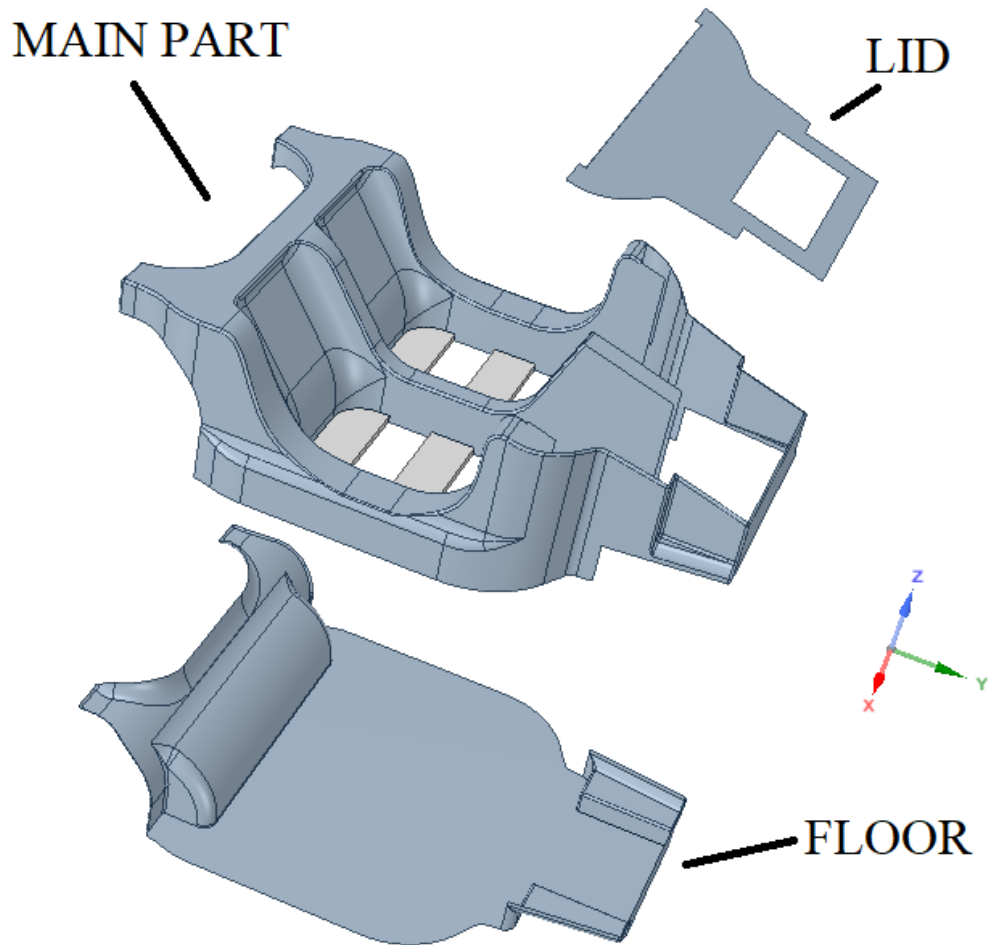


Figure 6.2. Chassis substructure parts.

The individual parts are now possible to be manufactured by the resin infusion process.

6.2 Identification of the critical bonded joint

Since the most important load scenario in a chassis is the torsion mode, the structure is studied for a torsion load. The mechanical model used is the same as the one detailed in section 2.5. The deformation mode under a torsion load of the chassis is shown in figure 6.3.

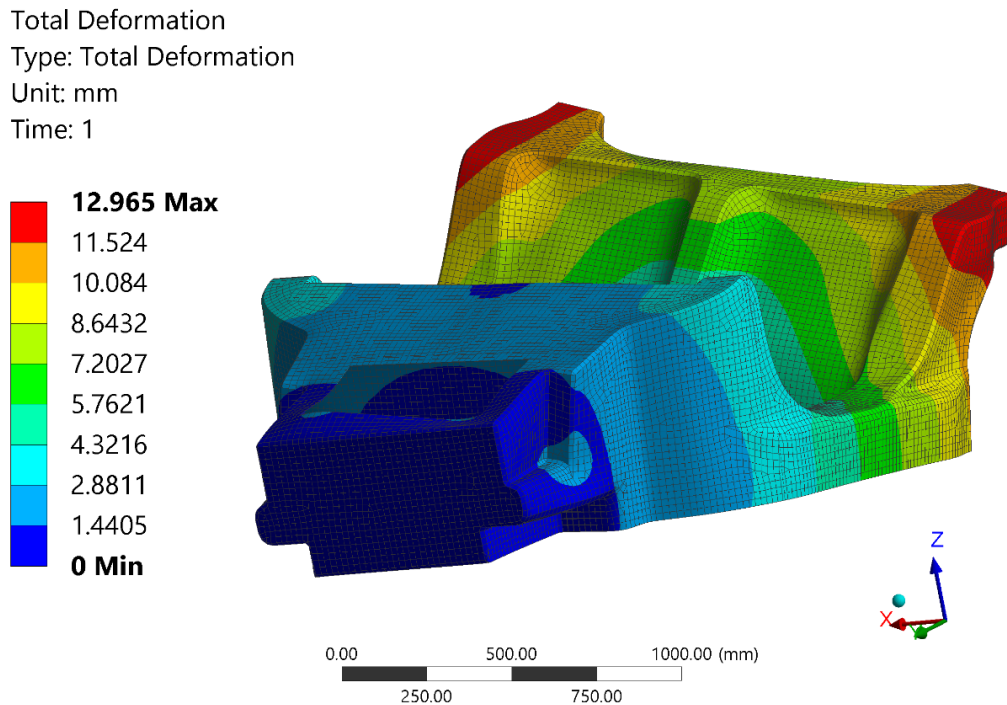


Figure 6.3. Chassis deformation under torsion.

Regarding strength, the critical joint is found by checking the strain energy density and the maximum shear stress. The strain energy density tells where the geometry is locally compliant, which means that the local strains are higher. Thus, figures 6.4 and 6.5 show the maximum shear stress and the strain energy density respectively.

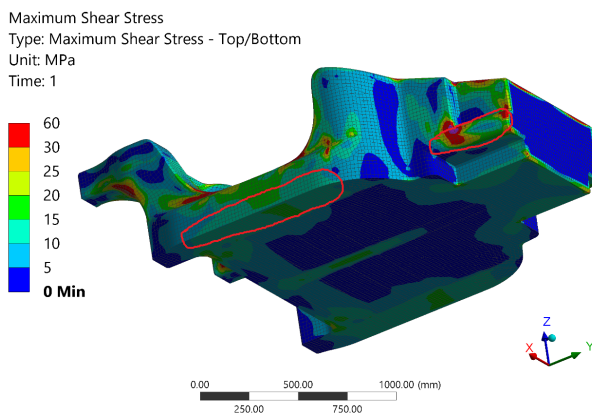


Figure 6.4. Maximum shear stress.

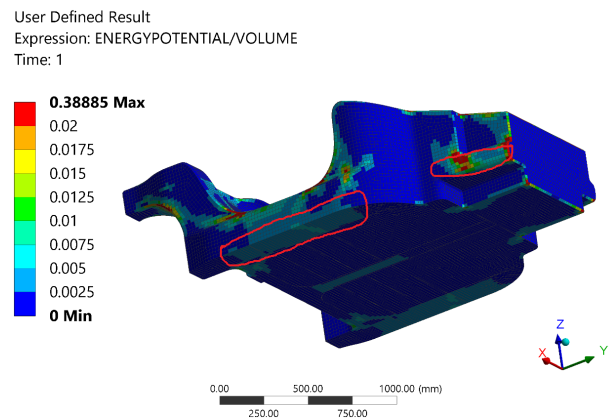


Figure 6.5. Strain energy density.

The areas highlighted in red are the regions where a bonded line is required according to the substructure model from figure 6.2, and the shear stress and strain energy density are higher. Since the lid part is not that important regarding strength, because if it fails, the structural integrity of the chassis remains intact, the critical structural joint of the chassis structure is the bonding between the main part and the floor. And the areas marked in red in the previous figure are the regions to study.

A representative joint structure of the identified critical assembly is modeled in the following section.

6.3 Multi-scale modeling of the bonded joint

In order to make a good optimization of the adhesive joint, a multi-scale model is developed. Multi-scale modeling is used when different scales are needed to define a system. The idea of using this way of modeling makes that big structures can be reduced to smaller sub-models, and thus, faster analysis can be performed with more accuracy. At the end, the sub-model results can be scaled up and implemented in the big model obtaining the benefits of a detailed analysis in a big structure like it is this case.

FULL CHASSIS MODEL UNDER TORSION

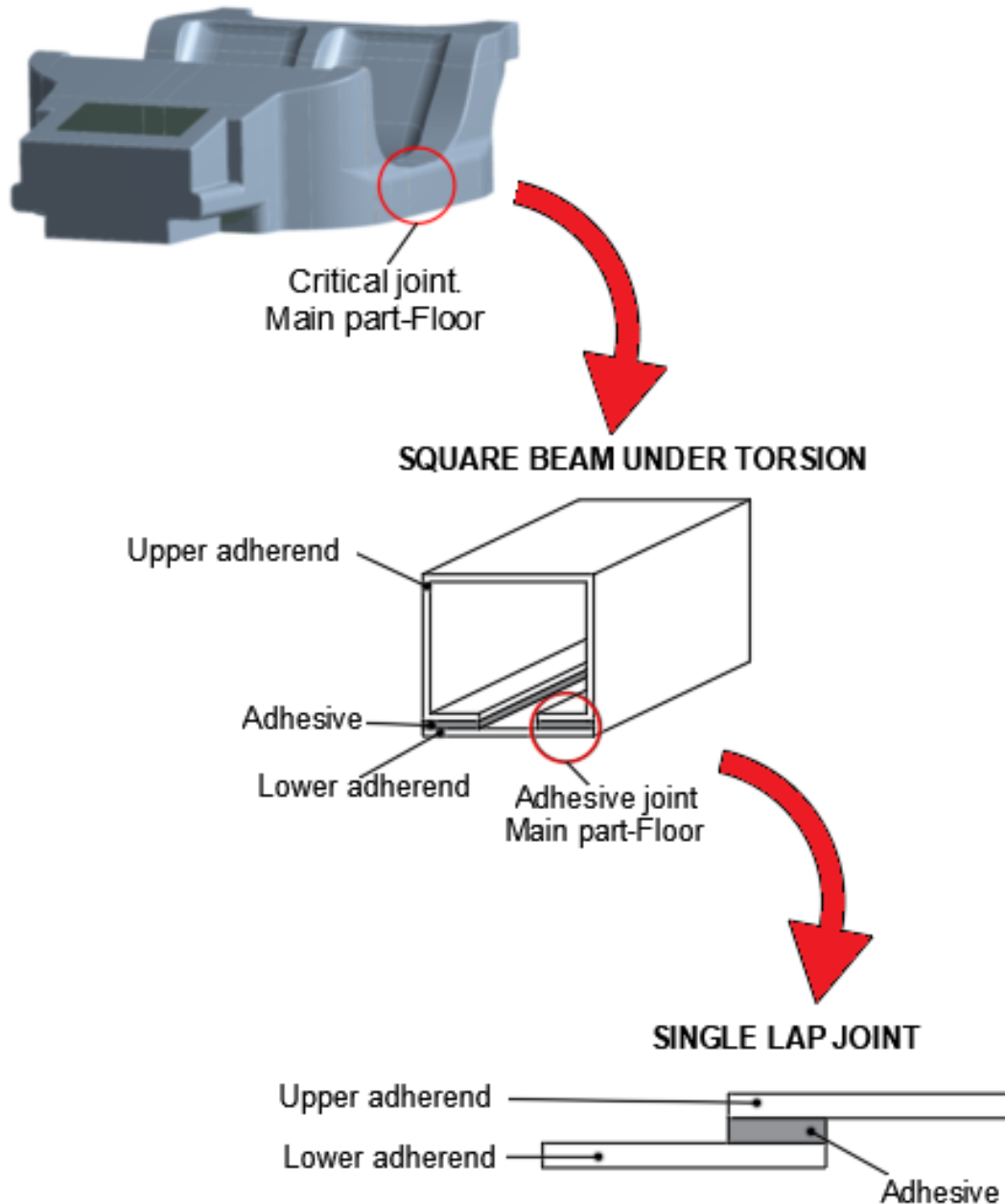


Figure 6.6. Multi-scale modeling.

Adhesive joints 7

The present chapter includes a brief summary of the theory and analytical models existing about adhesive joints. Moreover, a single lap joint, as sub-model structure of the chassis critical joint, is modeled in finite element software. The numerical model is validated analytically with a Matlab program which plots the state of stresses in a single lap joint.

7.1 State of the art. Adhesive bonded joints

Now a days, the use of adhesives in bonded joints is increasing more and more. Adhesives for composite structures offer higher strength and fatigue properties than mechanical joints. Many scientific studies have been done during the last decades about adhesive bonded joints. The types of joints have been classified in terms of strength based on stress by Hart-Smith [Hart-Smith, 1978]. Figure 7.1 shows the classification where a double scarf joint is the best joint type if the adherends are thick and high strength is required.

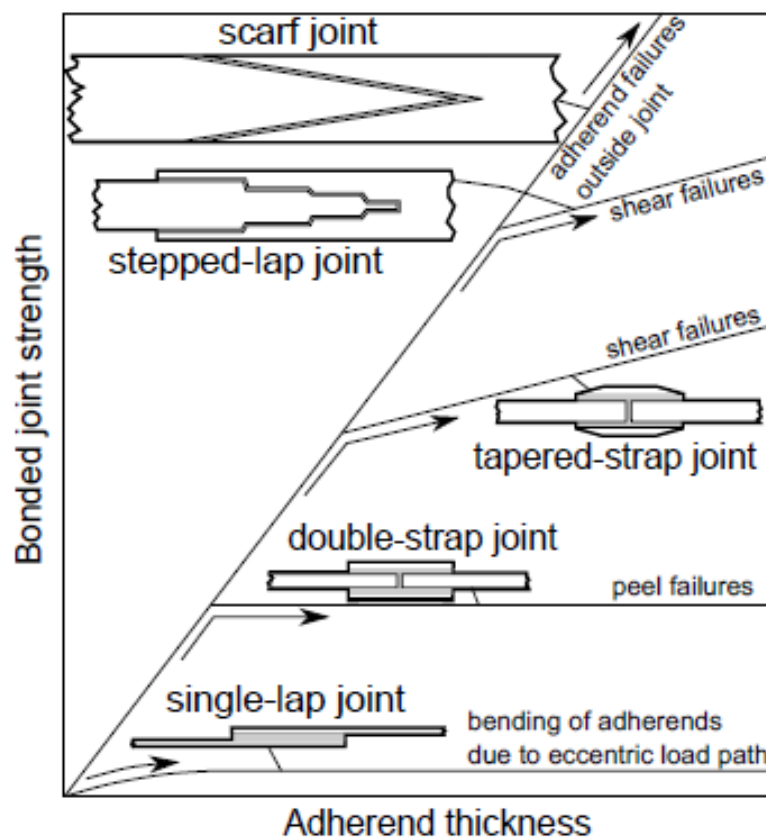


Figure 7.1. Adhesive joint strength for the different joint types with distinct adherend thicknesses. Figure by [Hart-Smith, 1978].

Many different analytical methods are available in the literature to calculate the stress distribution in adhesive joints. However the main analytical models for single lap adhesive joints are, Volkersen, Goland & Reissner and Hart-Smith. The differences of these principal models are explained below.

Simplest linear elastic analysis

The most simplified analysis where the assumptions are that the adherends are rigid and the adhesive deforms only in shear. Thus, the shear stress along the adhesive turns out to be constant. The deformation mode of this simple model is shown in figure 7.2.

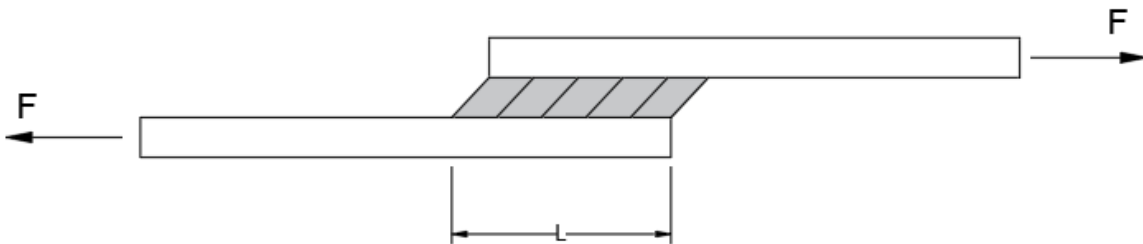


Figure 7.2. Linear elastic deformation of single lap joint.

Thus, the shear stress is obtained by just using linear elastic deformation as shown in equation 7.1.

$$\tau = \frac{F}{wL} \quad (7.1)$$

Where F is the applied force, w is the adhesive width and L the overlap length. This method has too many simplifications and it can be interpreted as the average shear stress in the adhesive material. Moreover it can be used as a first approximation when dimensioning the adhesive line of a structure.

Volkersen

In 1938, the first analytical model to calculate the stress distribution of a single lap joint is introduced by Volkersen [Volkersen, 1938] with the introduction of the concept of differential shear. Figure 7.3 shows the deformation in Volkersen model where the adherends are not rigid anymore and they deform in tension while the adhesive deforms in shear.

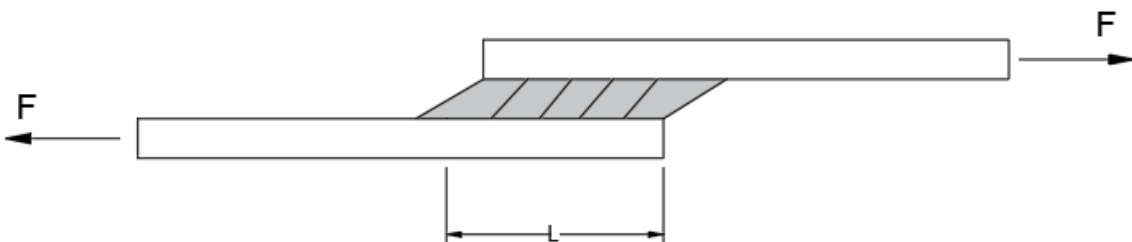


Figure 7.3. Volkersen deformation of single lap joint.

Goland & Reissner

In 1944, Goland and Reissner [Goland and Reissner, 1944], introduced a new model for adhesive bonded joints. In this case, the rotation of the adherends is included so that they fully deform in 2D.

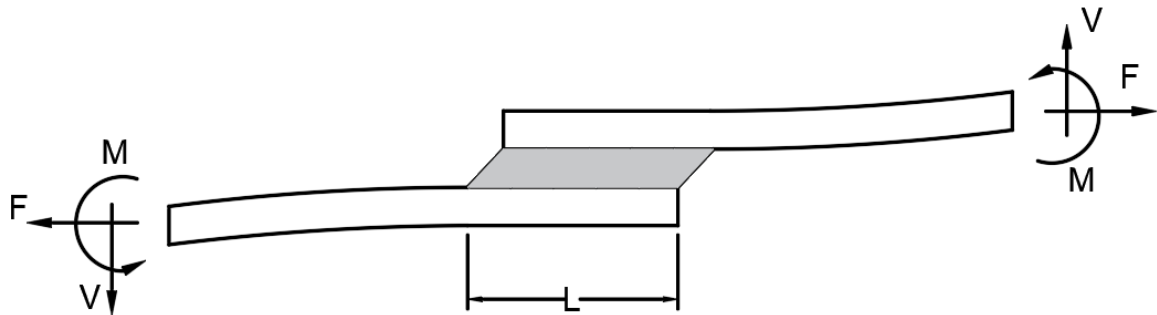


Figure 7.4. Goland & Reissner deformation of single lap joint.

Due to the offset of the applied force F to the middle plane of the joint, a moment M is produced. Due to this moment, the joint deforms in a rotational mode. And when the deformation is produced, the moment decreases, which gives a non-linear behavior. The non-linear effect has to be considered when large deflections. Goland & Reissner consider this situation by introducing a bending moment factor (k) and a transverse force factor (k_1). The bending moment factor relates the moment at the ends of the lap joint with the applied load and the transverse factor relates the shear force with the applied load.

The shear distribution (τ), along the overlap length in the adhesive, according to [Goland and Reissner, 1944] is then shown in equation 7.2.

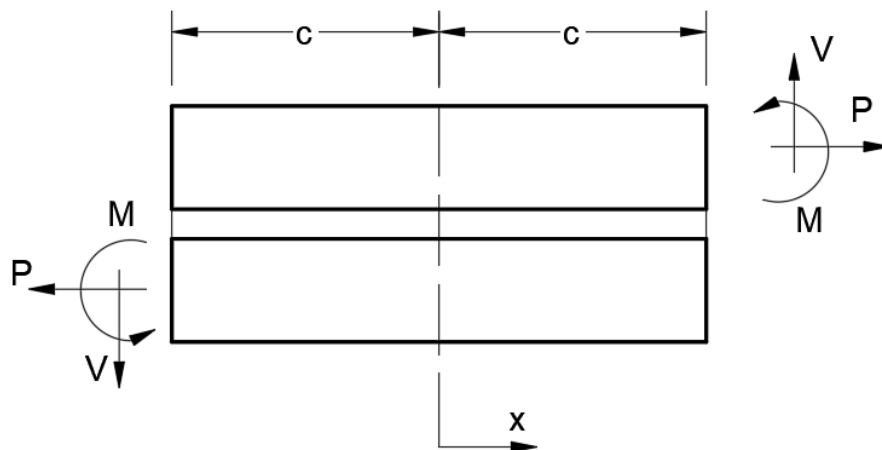


Figure 7.5. Goland & Reissner model.

$$\tau = -\frac{1}{8} \frac{P}{c} \left\{ \frac{\beta c}{t} (1 + 3k) \frac{\cosh\left(\frac{\beta c x}{t}\right)}{\sinh\left(\frac{\beta c}{t}\right)} + 3(1 - k) \right\} \quad (7.2)$$

Where P is the load per unit width, c is the overlap length divided by two, t is the thickness of the adherend, x is the coordinate x along the adhesive length, starting from the middle of the joint as shown in figure 7.5. The parameter β is a relationship between stiffnesses of adherends and adhesive, given by equation 7.3.

$$\beta^2 = 8 \frac{G_a}{E} \frac{t}{t_a} \quad (7.3)$$

Where G_a is the adhesive shear modulus, E is the Young's modulus of the adherends and t_a is the adhesive thickness.

Finally, the bending moment factor, k is defined in equation 7.4.

$$k = \frac{\cosh(u_2 c)}{\cosh(u_2 c) + 2\sqrt{2} \sinh(u_2 c)} \quad (7.4)$$

Where u_2 is equal to,

$$u_2 = \sqrt{\frac{3(1 - \nu^2)}{2}} \frac{1}{t} \quad (7.5)$$

In equation 7.5, the poisson's ratio is represented by ν . The peel stress distribution (σ) of the adhesive is also considered in this model and it is defined in equation 7.6.

$$\sigma = \frac{1}{\Delta} \frac{Pt}{c^2} [A + B] \quad (7.6)$$

Where A and B are:

$$A = \left(R_2 \lambda^2 \frac{k}{2} + \lambda k_1 \cosh(\lambda) \cos(\lambda) \right) \cosh\left(\frac{\lambda x}{c}\right) \cos\left(\frac{\lambda x}{c}\right) \quad (7.7)$$

$$B = \left(R_1 \lambda^2 \frac{k}{2} + \lambda k_1 \sinh(\lambda) \sin(\lambda) \right) \sinh\left(\frac{\lambda x}{c}\right) \sin\left(\frac{\lambda x}{c}\right) \quad (7.8)$$

The transverse force factor, (k_1), is defined in equation 7.9.

$$k_1 = \frac{kc}{t} \sqrt{3(1 - \nu^2)} \frac{P}{tE} \quad (7.9)$$

And λ and Δ are defined in the following expressions (7.10 and 7.11).

$$\lambda = \gamma \frac{c}{t} \quad \text{and} \quad \gamma^4 = 6 \frac{E_a}{E} \frac{t}{t_a} \quad (7.10)$$

$$\Delta = \frac{1}{2} (\sin(2\lambda) + \sinh(2\lambda)) \quad (7.11)$$

Being E the Young's modulus of the adherends.

Moreover, the terms R_1 and R_2 are defined as follows.

$$R_1 = \cosh(\lambda) \sin(\lambda) + \sinh(\lambda) \cos(\lambda) \quad (7.12)$$

$$R_2 = -\cosh(\lambda) \sin(\lambda) + \sinh(\lambda) \cos(\lambda) \quad (7.13)$$

Hart-Smith

Hart-Smith (1973) [Hart-Smith, 1978], introduced large deflections into a model for single lap and double lap joints for NASA. The idea is to combine elastic peel stresses with plastic shear stresses. Therefore, Hart-Smith, [Hart-Smith, 1978] presented a modified expression for the bending moment factor which includes the adherends bending stiffness. The introduction of adhesive plasticity in the model produces more accurate results than the previous models but in this project, since the finite element analysis done are linear, the model used to validate the numerical model is Goland & Reissner since it includes the peel stresses which are of interest in the present thesis.

7.2 FEM model of the single lap joint

The single lap joint which represents the critical joint problem of the chassis structure is modeled numerically in finite element software. In order to set a mechanical model which can be used for the analysis of the joint strength, an isotropic material is used for the numerical model, so that it can be validated analytically. The material chosen for the adherends is aluminum 6061 T6 [Metals, Metals] and for the adhesive, a structural epoxy adhesive from Araldite company [Araldite, Adhesives]. A table with the mechanical properties (at 25°) of the materials is shown in table 7.1. The materials chosen for the numerical model are not final materials. They are just useful to validate a mechanical model which can be used to investigate afterwards.

Material	E (MPa)	G (MPa)	ν
<i>Aluminum 6061 T6</i>	68900	26000	0,33
<i>Araldite AW4858</i>	1600	800	--

Table 7.1. Single lap joint. Materials.

Figure 7.6 shows the dimensions of the single lap model used.

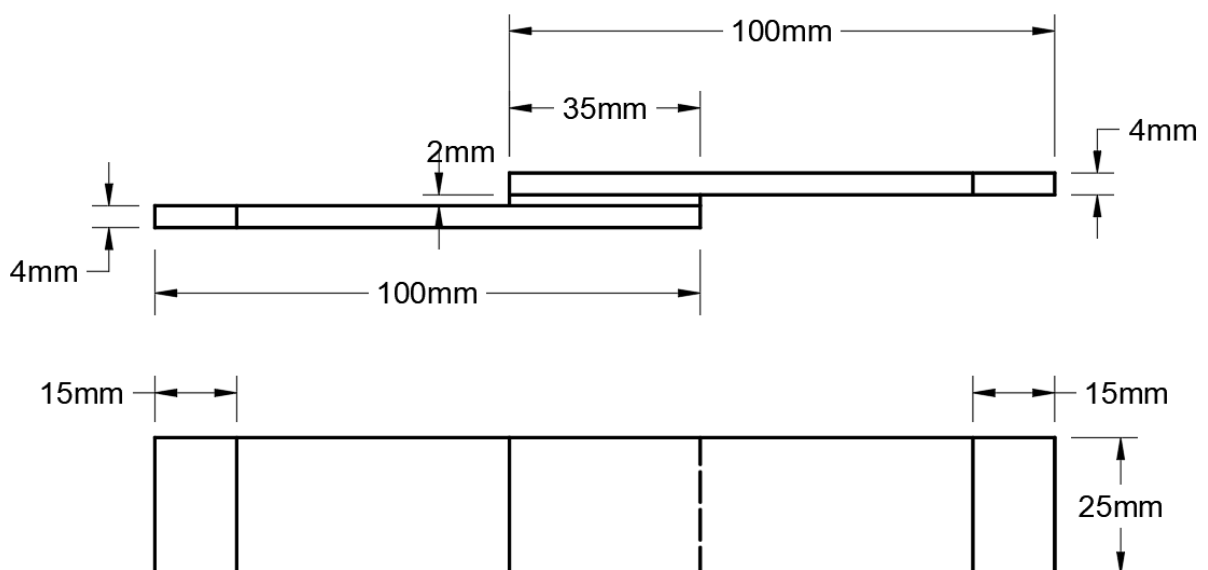


Figure 7.6. Single lap model. Dimensions.

Two tabs are introduced in the model, as shown in figure 7.7. The tabs are designed in order to introduce appropriate boundary conditions to get an accurate model which corresponds to the analytical one.

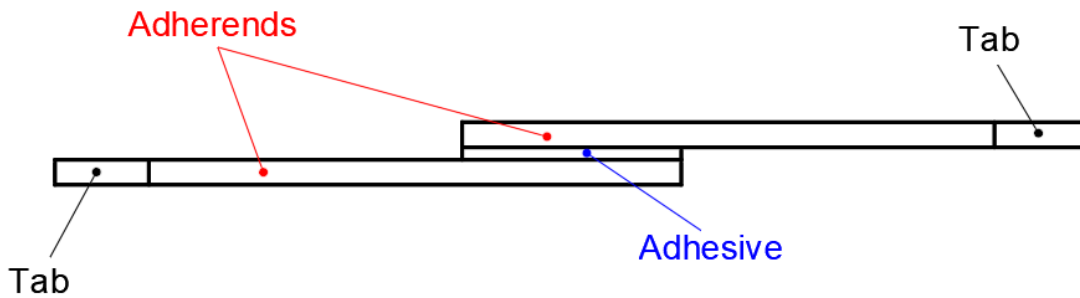


Figure 7.7. Single lap model. Tabs.

The geometry is modeled in 3D in Ansys Workbench and the boundary conditions are applied as figure 7.8 shows. The two tabs are used to introduce the boundary conditions and to obtain a symmetric static analysis with respect to the center of the overlap.

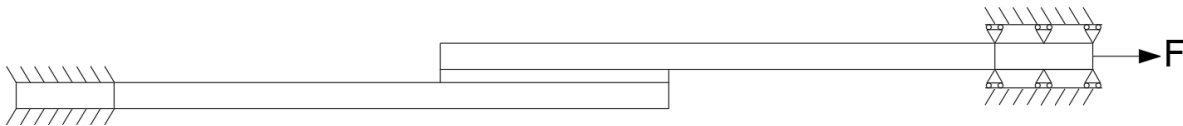


Figure 7.8. Single lap. Boundary conditions.

As it is shown, the left tab is clamped while the right tab is not allowed to translate vertically. A sample horizontal force of 1000N is applied on the right side surface. The geometry is modeled as a solid, and meshed with solid elements. The model mesh is shown in figure 7.9.

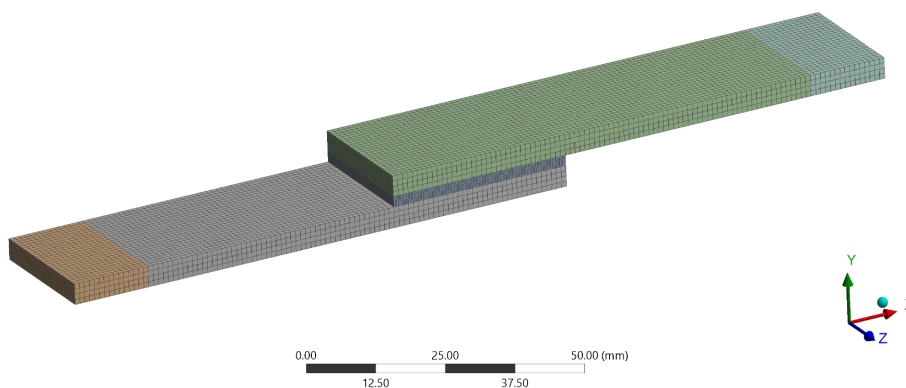


Figure 7.9. Single lap. Mesh.

- Element type: Solid 186 tetrahedrons (20 nodes and 3 d.o.f per node)
- Number of elements: 86584
- Number of nodes: 398677

The SOLID186 element is chosen because it can be used as a layered element as well, which allows a composite modeling for the further studies. The contact elements between the adhesive and the adherends are MPC elements which ensure a perfect bonding. The elements in the adhesive are refined until convergence is found. A convergent value is needed in order to validate the model with the analytical one.

The convergence study is done based on the shear and peel stresses, since they are the values of interest. Therefore, a path in the adhesive is chosen to analyze the stresses, as shown in figure 7.10 and 7.11.

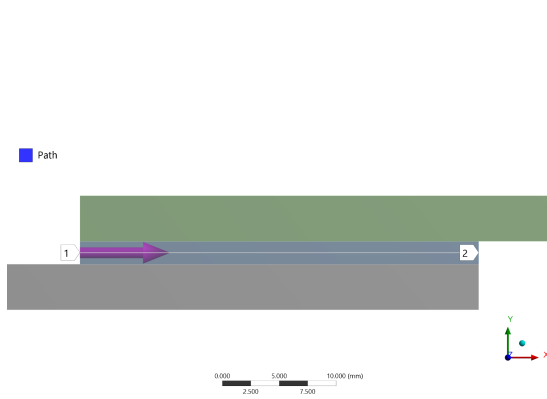


Figure 7.10. Stress plot path. View 1.

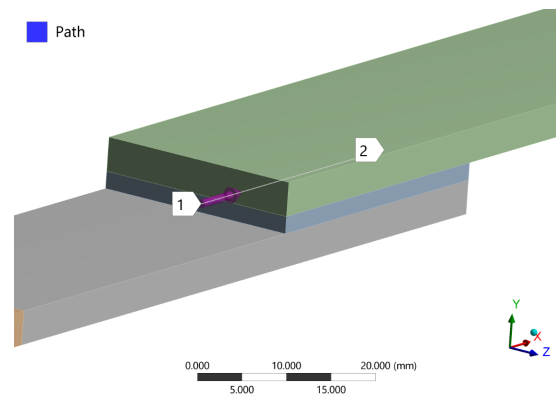


Figure 7.11. Stress plot path. View 2.

The path is chosen in the middle of the thickness of the adhesive and in the middle of the width of the adhesive layer too. This is because the stress singularity found at the top and bottom of the adhesive layer produces wrong stress results. Therefore, the desired values are checked as far as possible from the singularities, so in the middle. The peel and shear stresses are plotted along the path 1 – 2 from figure 7.10.

The element size of described mesh from figure 7.9, is obtained from the convergence study shown in figure 7.12.

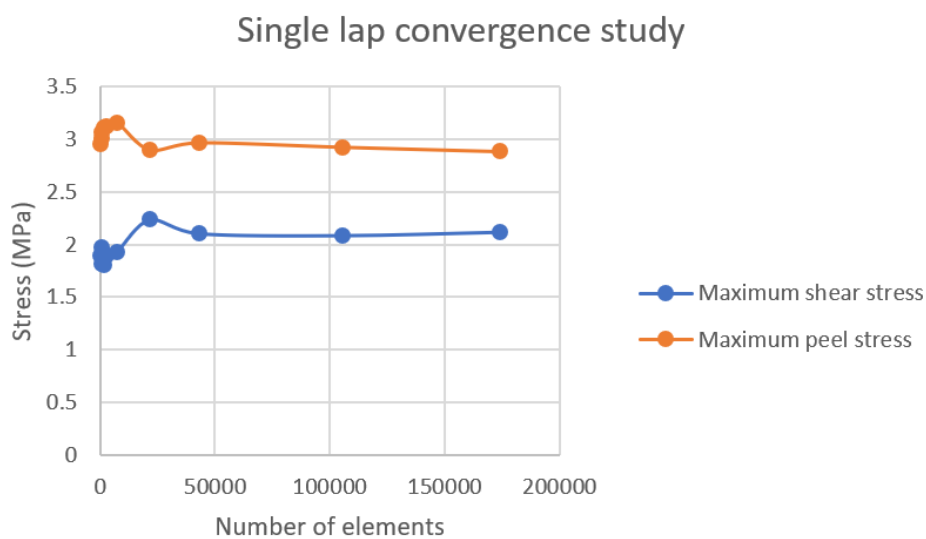


Figure 7.12. Convergence study. Single lap joint.

The previous figure shows that there is convergence, so the stresses are correct. The peel stress

and shear stress shown in figure 7.13 are now obtained according to the described model.

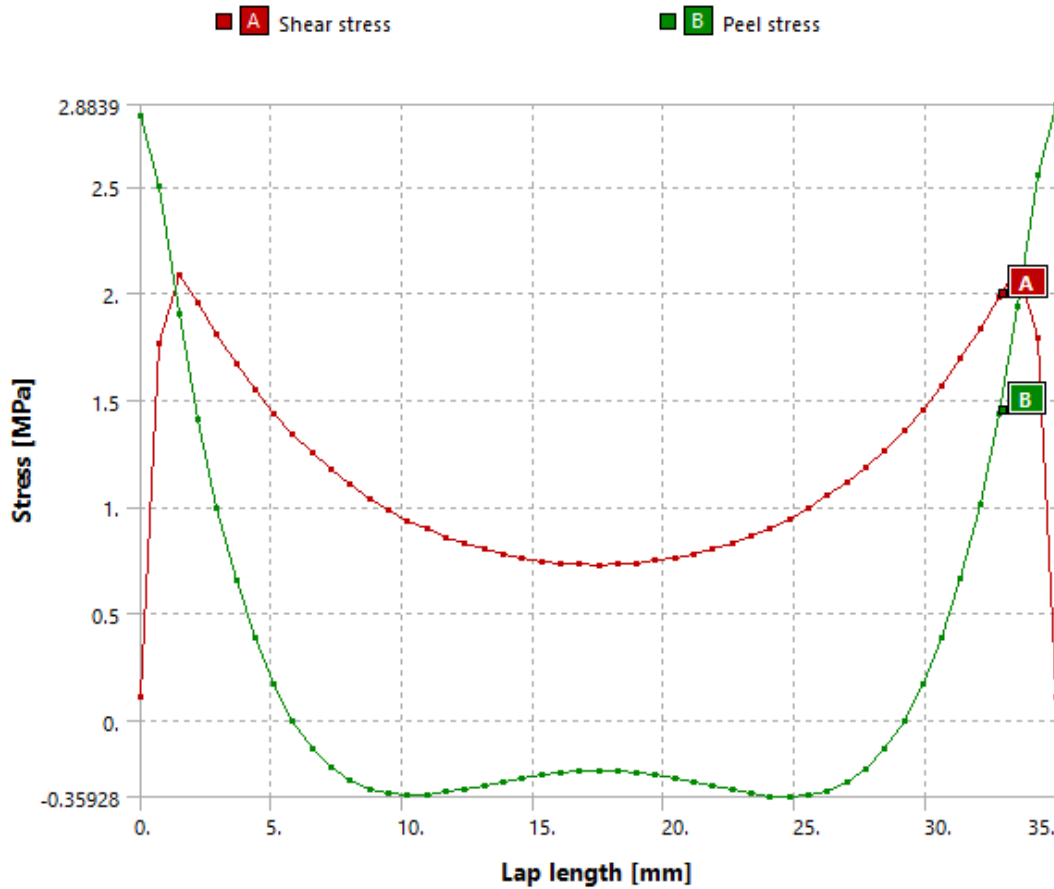


Figure 7.13. Shear and peel stresses in the FEM.

7.3 Analytical validation of the FEM

The finite element model of the single lap joint is the tool used for the joint design. Geometry studies, improvement of strength and layup sequence effects on the joint strength are studied using the numerical model. Therefore, it requires to be validated, for what the analytical model by Goland & Reissner described in section 7.1 is used to do that. A Matlab code is created for plotting the shear and peel stresses according to Goland & Reissner model. The Matlab code can be found in appendix F.

Matlab results are shown in figure 7.14 and FEM results are shown in figure 7.15.

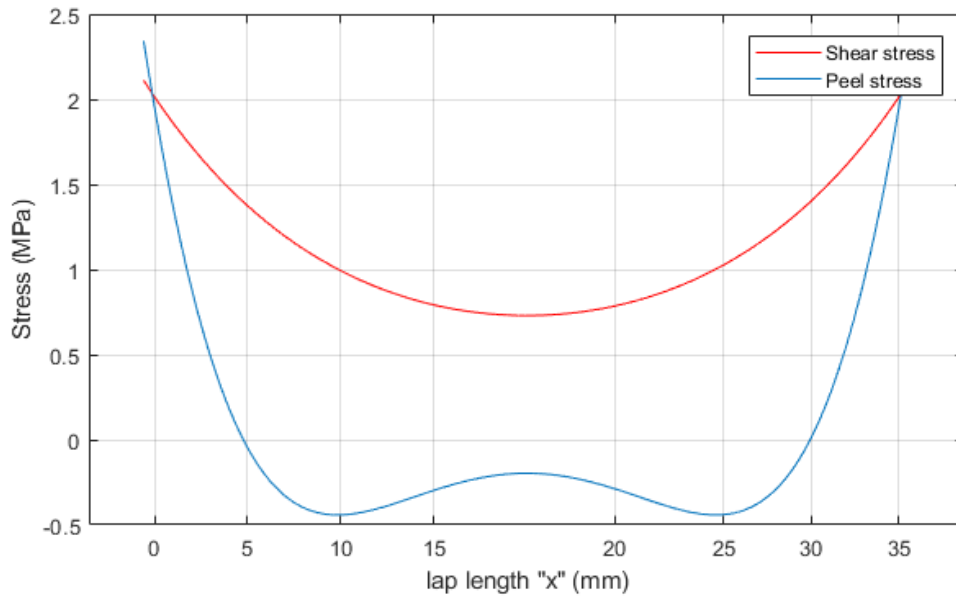


Figure 7.14. Matlab results. Shear and peel stress. Goland & Reissner.

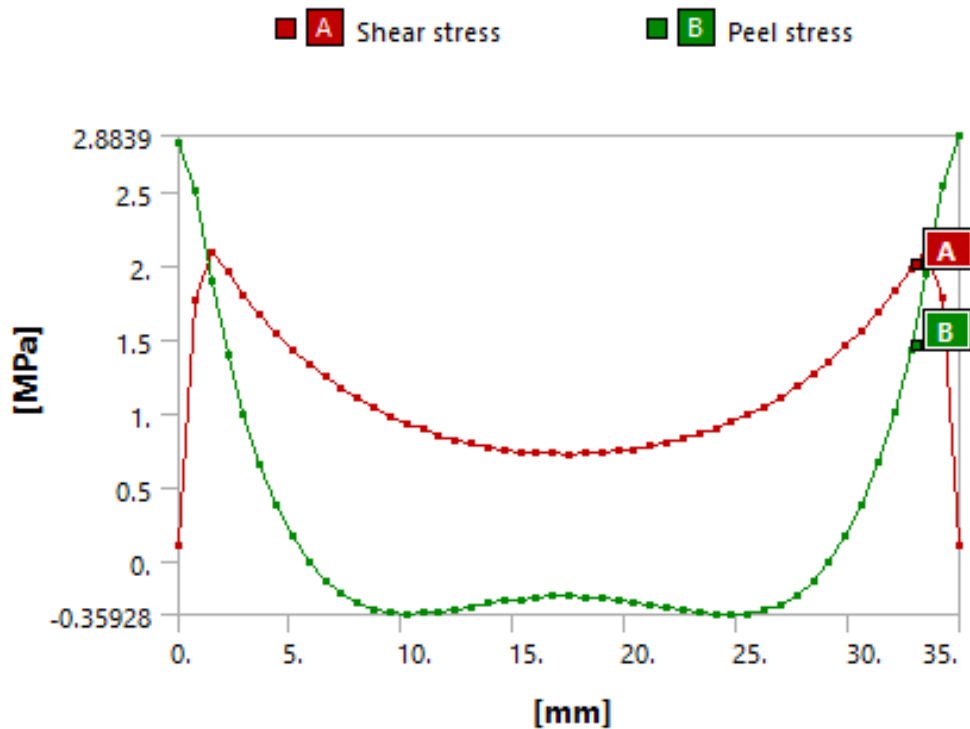


Figure 7.15. FEM results. Shear and peel stress.

As it can be seen from the results, a good match is produced in stress results for both, peel and shear stresses along the overlap length of the single lap joint. Therefore, the numerical model represents the real behavior of the lap joint under a tensile load, which means that the model can be used for development and improvement of the joint.

Adhesive joint design 8

Along the present chapter, the strength of the adhesive joint is examined and optimized. The effects of joint geometry, single lap geometry and lay-up sequence on the joint strength are investigated and a feasible solution is proposed. The strength approach taken is stress based so no energy criteria are used. Thus, the adhesive is assumed to be perfectly bonded, without voids or cracks.

8.1 Joint geometry

In chapter 6, the multi-scale modeling approach is introduced. The main part and the floor of the chassis have to be bonded and the first step is to set the target of the design. To design an optimum adhesive joint, the adhesive must work in shear mode. So that no tensile stresses are introduced or they are minimized. Therefore the first goal is to design an assembly of the chassis with the floor in a way that most of the stresses transmitted to the adhesive are shear stresses. From the multi-scale modeling approach, the squared beam under torsion shown in figure 8.1 is set as the model to design the mentioned assembly.

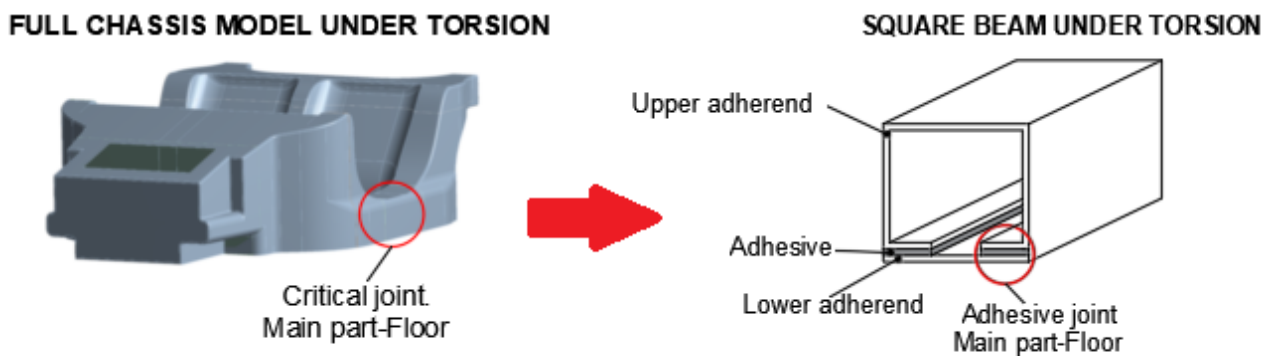


Figure 8.1. Square beam under torsion.

A numerical model is set-up with isotropic materials. The geometry does not depend on the material chosen so, for simplicity, the analysis is done with the previous materials used during the chassis design and validation in previous chapters as table 8.1 shows.

Material	E (MPa)	G (MPa)	ν
Aluminum 6061 T6	68900	26000	0,33
Araldite AW4858	1600	800	0,34

Table 8.1. Adhesive joint materials.

The model with the boundary conditions is shown in figure 8.2.

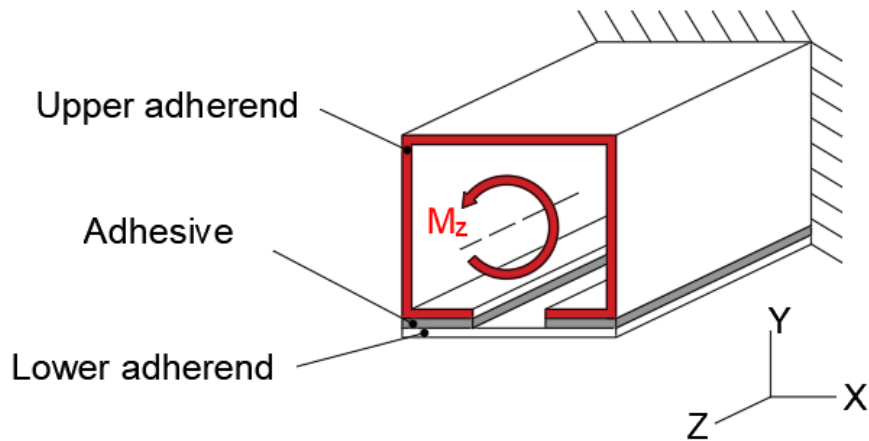


Figure 8.2. Square beam model. Boundary conditions.

The rear surface of the beam is clamped while a moment is applied on the front surface of the upper adherend. Only the upper adherend is subjected to the moment because when the chassis is under torsion, it is because the main part (6.6) of the chassis is the one where the loads from the suspension are applied to through the spring. Therefore, the floor is just offering resistance to the torsion mode. The numerical model is then set-up with an applied moment of 200000Nm, where the thickness of the adherends is 20mm and the adhesive thickness is 5mm as shown in figure 8.3.

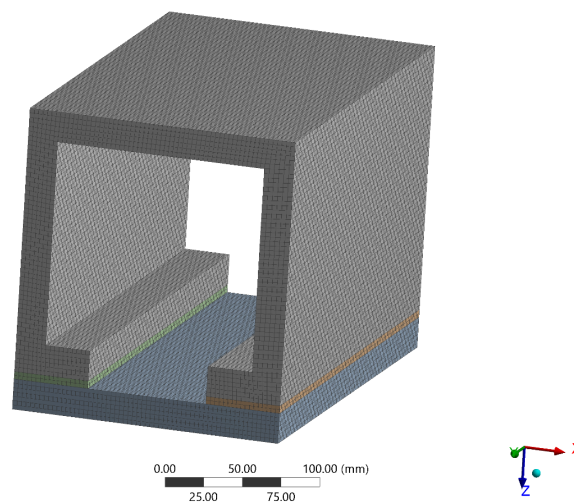


Figure 8.3. Square beam model. Mesh.

- Element type: Solid 186 tetrahedrons (20 nodes and 3 d.o.f per node)
- Number of elements: 167100
- Number of nodes: 763609

The adhesive width is 50mm for each side and the length is 300mm. Both dimensions together with the thicknesses are fixed for the different models from now on, so they can be compared proportionally.

The deformation under the applied torsion is analyzed. The total deformation is scaled and shown in figure 8.4.

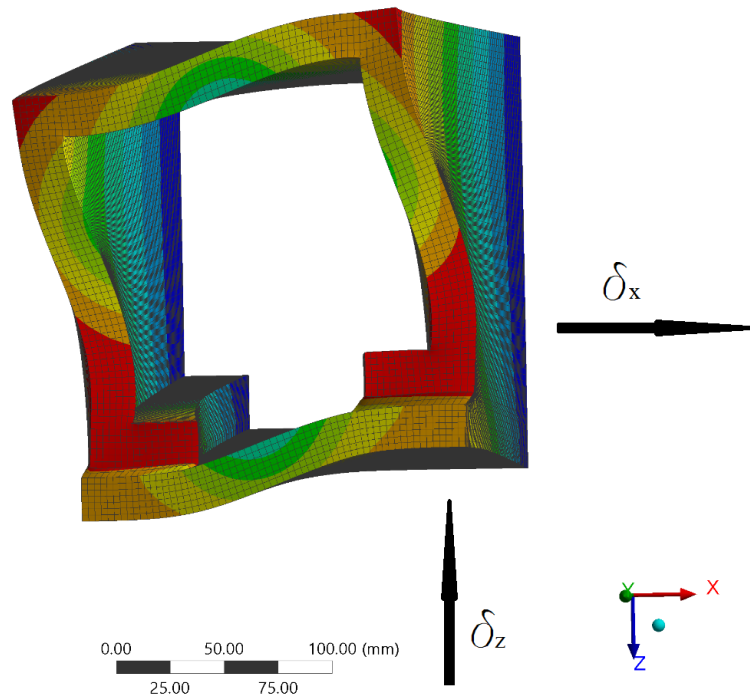


Figure 8.4. Square beam model. Deformation under torsion.

As it is shown, according to the coordinate system of the figure, due to the moment applied, the torsion mode produces in the right adherend two main deformations δ_x and δ_z . The displacement δ_x , in this case introduces a shear stress to the adhesive layer since the displacement is parallel to the adhesive layer. However, the displacement δ_z introduces a peel stress to the adhesive. Therefore, the geometry needs to be optimized, so the peel stresses are minimized and most of the stress is shear, where the adhesive works more efficiently. Due to the torsion, there is always the two forces as a consequence of the deformation mode. Thus a reasonable idea is to place the lapped joint in a 45° angle.

Three different geometries are analyzed to confirm that the 45° lap is the joint with less peel stress.

Geometry 1 (0° lap joint)

From the first input geometry, previously described (8.3), shear stresses and peel stresses are plot at the interface between adhesive and adherend. Shear and peel stresses at the adhesive interface are shown in figures 8.5 and 8.6.

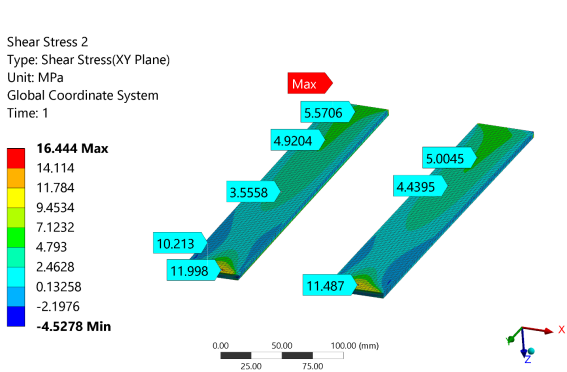


Figure 8.5. Shear stress in adhesive layer. 0° lap joint.

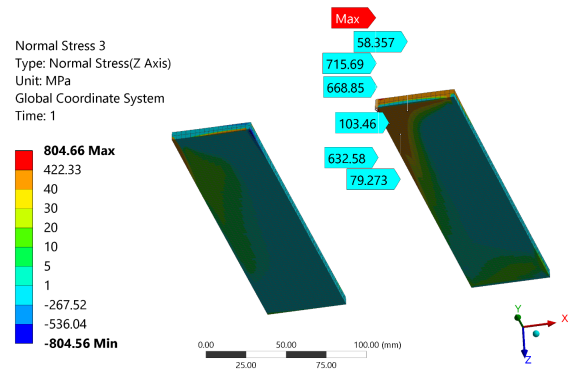


Figure 8.6. Peel stress in adhesive layer. 0° lap joint.

The maximum values are:

- Maximum shear stress: 16,4MPa
- Maximum peel stress: 804,6MPa

Geometry 2 (90° lap joint)

The adhesive layers are now rotated 90° with respect to the previous geometry. The geometry is shown in figure 8.7.

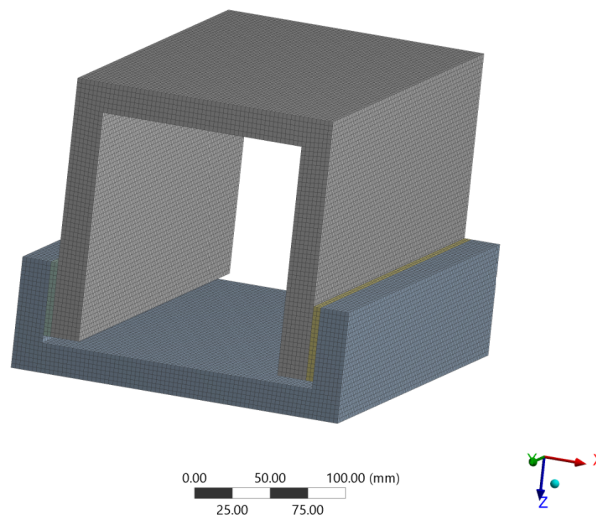


Figure 8.7. Geometry 2 (90° lap joint). Mesh.

- Element type: Solid 186 tetrahedrons (20 nodes and 3 d.o.f per node)
- Number of elements: 195300
- Number of nodes: 887221

Shear and peel stress plots are shown in figures 8.8 and 8.9.

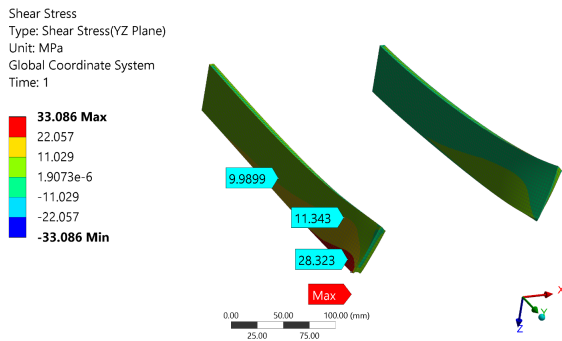


Figure 8.8. Shear stress in adhesive layer. 90° lap joint.

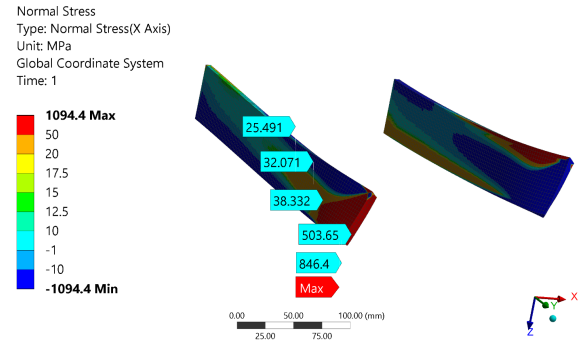


Figure 8.9. Peel stress in adhesive layer. 90° lap joint.

The maximum values are:

- Maximum shear stress: 33,08MPa
- Maximum peel stress: 1094MPa

Geometry 3 (45° lap joint)

The adhesive layers are now placed 45° with respect to the floor. The geometry is shown in figure 8.10.

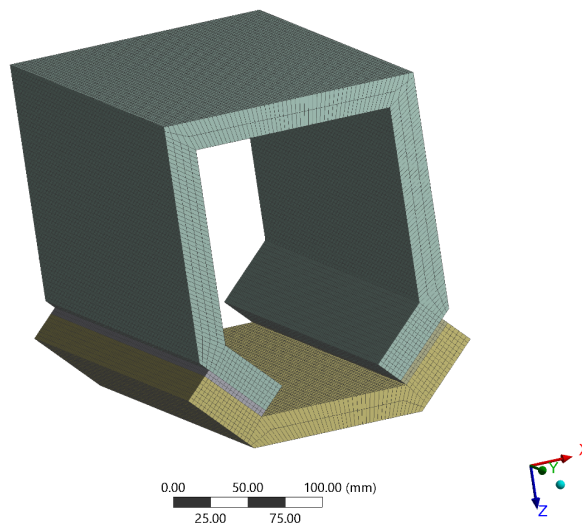


Figure 8.10. Geometry 3 (45° lap joint). Mesh.

- Element type: Solid 186 tetrahedrons (20 nodes and 3 d.o.f per node)
- Number of elements: 108800
- Number of nodes: 534398

Shear and peel stress plots are shown in figures 8.11 and 8.12.

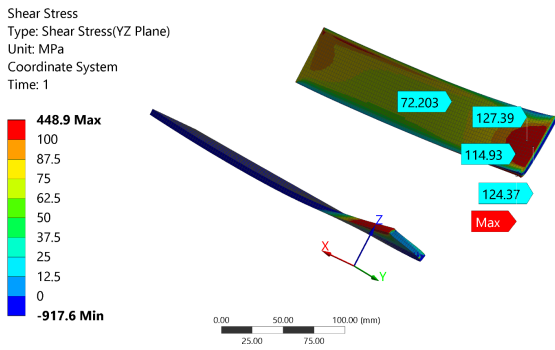


Figure 8.11. Shear stress in adhesive layer. 45° lap joint.

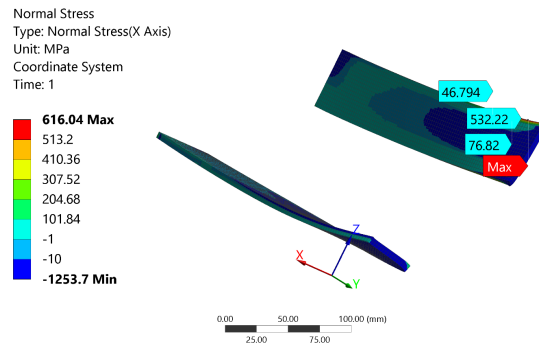


Figure 8.12. Peel stress in adhesive layer. 45° lap joint.

The maximum values are:

- Maximum shear stress: 448,9MPa
- Maximum peel stress: 616,04MPa

Joint geometry results

The results confirm the hypothesis previously stated. Table 8.2 shows the stress comparison between the three studied geometries.

Joint	Max. Shear Stress(MPa)	Max Peel Stress (MPa)
0° lap joint	16,4	804,6
90° lap joint	33.08	1094
45° lap joint	448,9	616,04

Table 8.2. Maximum shear and peel stress evaluation.

The peel stresses are reduced and transformed into shear stresses at the adhesive interface. Therefore, the geometry chosen for the bonded joint is the geometry 3, shown in figure 8.13.

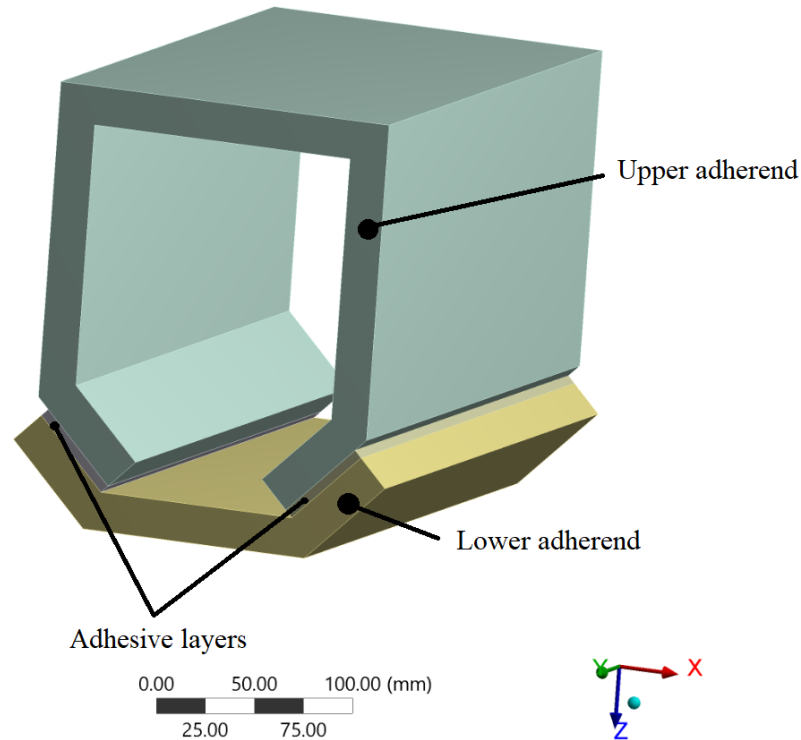


Figure 8.13. Single lap chosen geometry.

8.2 Single lap geometry

The deepest sub-structure from the multi-scale model explained in section 6 is now modeled in this section as figure 8.14 shows.

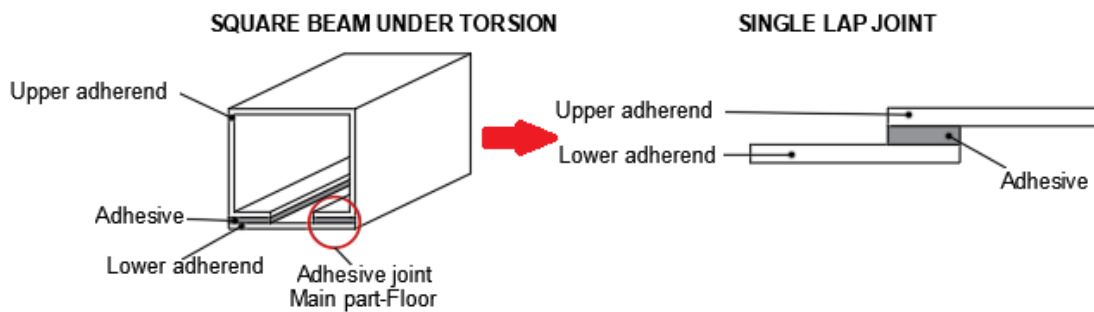


Figure 8.14. Single lap, sub-scale model.

The local geometry of the single lap joint is modified so that the peel and shear stress concentrations are reduced. The mechanical model used has been validated in section 7.3 with an analytical Matlab model. The materials, again are isotropic materials since they are not relevant when improving geometry aspects. Thus, the same materials used in the previous section, shown in table 8.1 are used now.

The dimensions of the numerical model are shown in section 7.3 and the boundary conditions are shown in the following figure (8.15).



Figure 8.15. Boundary conditions. Single lap.

The force applied in this case is 10000N. and the peel and shear stresses along the chosen path, (7.3) are shown in figure 8.16.

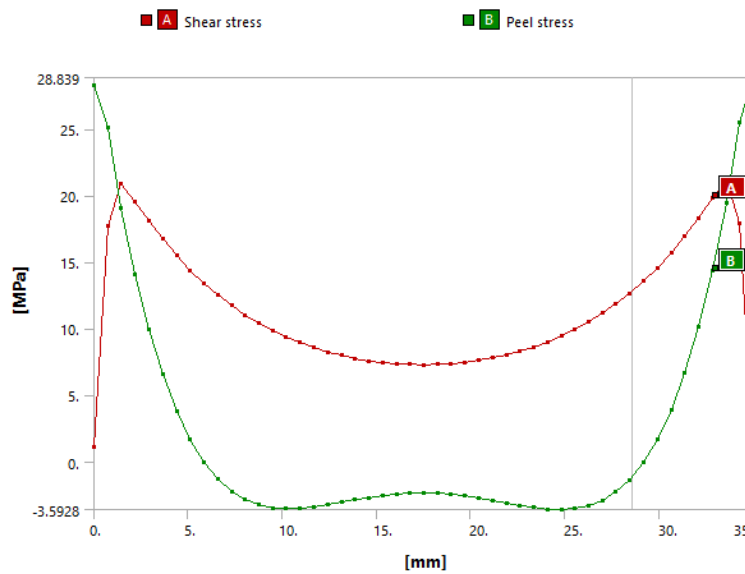


Figure 8.16. Peel and shear stress. Regular single lap joint.

The peel stresses have to be reduced. They appear due to the deformation of the adherends, which show rotational deformation due to the moments introduced because of the offset from the middle plane of the applied load. To avoid the mentioned deformation, shown in figure 8.17, the adherends have to become stiffer, or the adhesive more compliant, so that the displacement of the ends of the adherends should be reduced. Moreover, in order to reduce the peel stress concentration at the sides of the single lap joint, different end geometries have been studied by many authors. From [da Silva and Adams, 2007], Silva and Adams studied the different possibilities to reduce the peel stresses in single lap joints with composites. From the four geometries that they proposed, inside taper, outside taper, adhesive fillet and inside taper with adhesive fillet, the only one which could easily be implemented in the manufacturing of the chassis is the outside taper geometry. And indeed, from their work, a peel stress reduction is achieved.

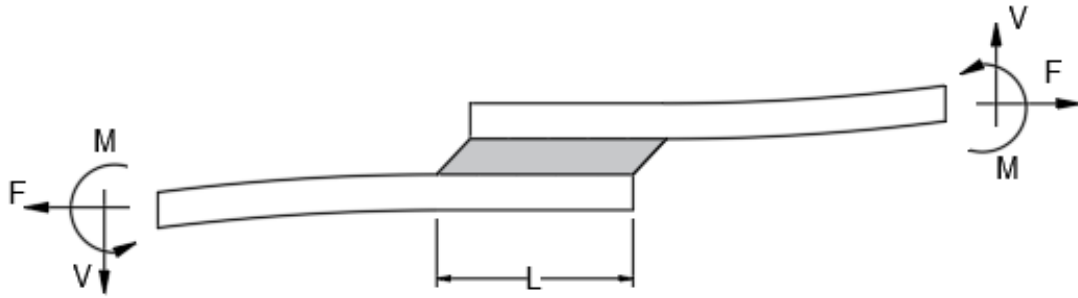


Figure 8.17. Rotational deformation of the adherends due to the moment.

Tapered geometry

Since the materials are fixed because the target is to improve the joint from a geometrical point of view, different proposed geometries are analyzed. As a first improvement, tapered adherends are introduced into the numerical model to see the resultant peel stresses. The corners of the adherends are tapered with a slope of 13° . Figure 8.18 shows the numerical model outside tapered single lap joint.

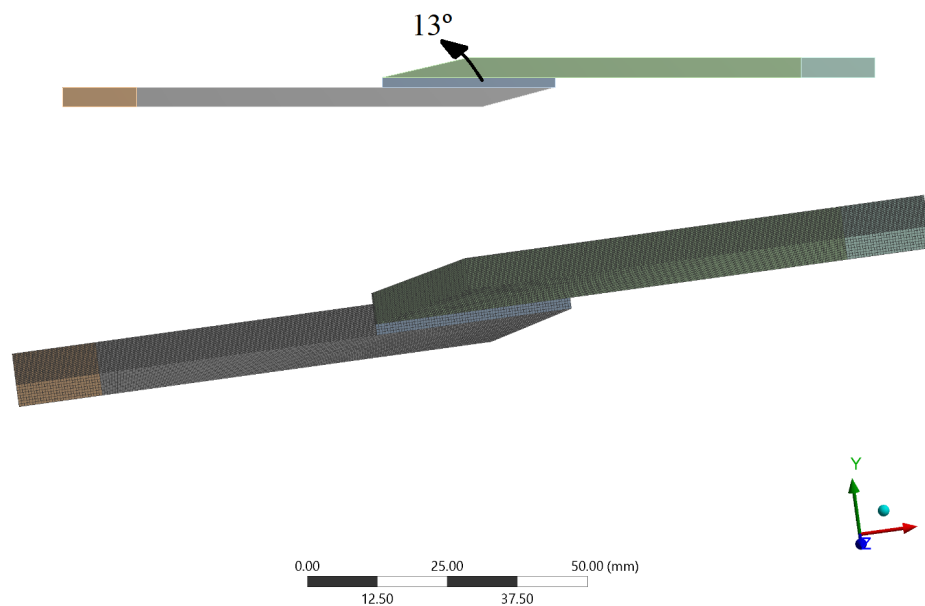


Figure 8.18. Tapered single lap joint.

- Element type: Solid 186 tetrahedrons (20 nodes and 3 d.o.f per node)
- Number of elements: 398677
- Number of nodes: 1507148

The peel stress is, indeed reduced by a 20% approximately. Figure 8.19 shows the peel and shear stress distribution in the single lap joint under the same load than the regular joint.

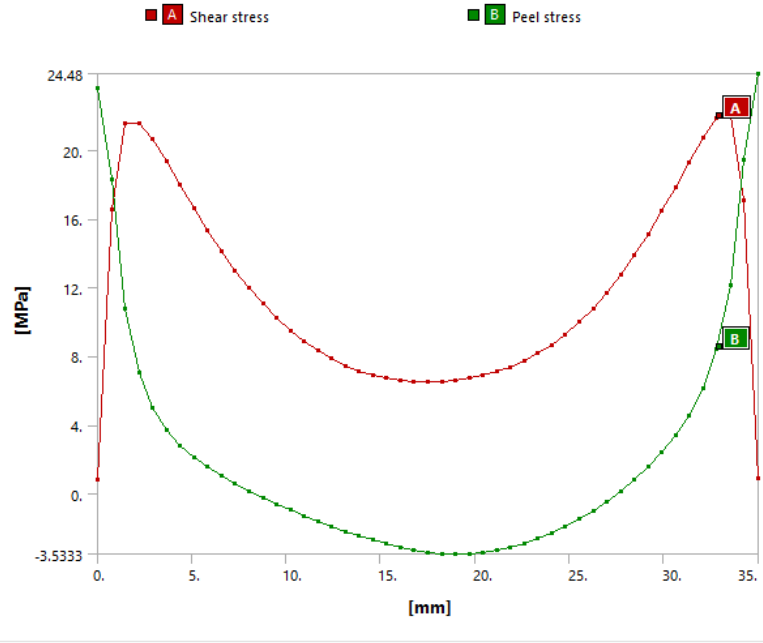


Figure 8.19. Peel and shear stress for the tapered single lap joint.

Besides the reduction of the peel stress, the whole stress distribution becomes more uniform when more tapering is introduced.

Since the adhesive is designed to work in shear mode, and thus, peel stresses have to be minimized as much as possible, different geometry modifications are introduced. The intention is to reduce the deformation shown in figure 8.17 by changing the stiffness distribution along the overlap length of the joint. Therefore, if the cross section is increased at the points where more deflection is occurring, the moment of inertia is increased too and as a result, the local stiffness of the geometry is improved.

Modified geometry 1

A first change in the geometry is introduced by intuition. The idea is to increase the overall stiffness of the joint so the adhesive thickness is increased in the center of the overlap and the top adherend is curved.

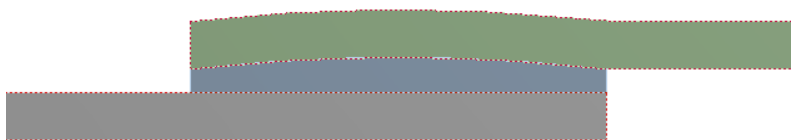


Figure 8.20. Modified geometry 1.

- Maximum shear stress: 25,8MPa

- **Maximum peel stress:** 33,3MPa

The results show an increment in stresses, peel and shear stresses. This is because at the ends the joint becomes less stiff than in the center, producing more stress concentration due to the rotational deformation.

Modified geometry 2

As the previous modification does not improve the geometry, in this case, the moment of inertia is increased at the ends of the overlap length, where the highest stress concentrations occur. Thus, adhesive thickness is increased at the ends of the joint and the adherends are shaped to adapt to the geometry as shown in figure 8.21.

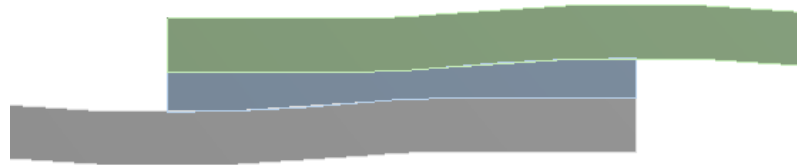


Figure 8.21. Modified geometry 2.

- **Maximum shear stress:** 19,6MPa
- **Maximum peel stress:** 22MPa

The stresses are reduced as expected. However, since the single lap is part of the chassis structure of the car, one of the adherends has to be completely flat because it is manufactured by using a flange for the mold. Thus, only one of the adherends which is part of the floor of the chassis can have a variable geometry.

Modified geometry 3

The following geometry, shown in figure 8.22, has the same advantages of the previous one which are the stress reduction due to stiffer lap ends but it fulfills the manufacturing requirement of having one flat adherend. Thus, the thickness of the adhesive is reduced by half in the middle of the lap joint and the upper adherend is shaped so it fits the new geometry.

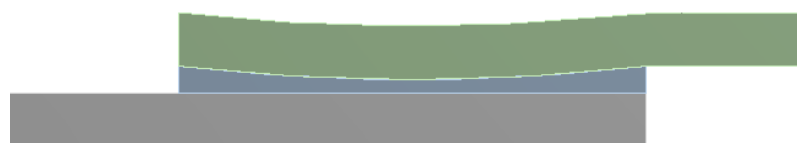


Figure 8.22. Modified geometry 3.

- **Maximum shear stress:** 20,5MPa

- **Maximum peel stress:** 24,5MPa

Compared to the previous iteration the peel stress has improved less but compared to the regular shape it improves significantly.

Modified geometry 4 (Case 3 + Tapered geometry

The tapered shape is now implemented into geometry 3 and the geometry is shown in figure 8.23.

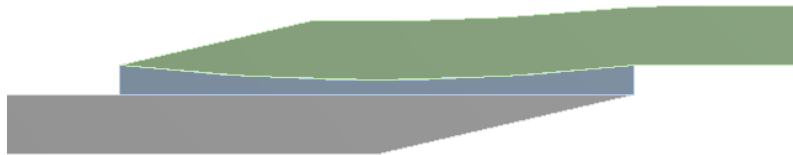


Figure 8.23. Modified geometry 4.

- **Maximum shear stress:** 21,4MPa
- **Maximum peel stress:** 19,5MPa

The combination of both modifications reduces the peel stresses importantly and the joint is now much more efficient than the regular single lap joint.

Results

A comparison chart of the peel stress distribution for the different analysis is shown in figure 8.24.

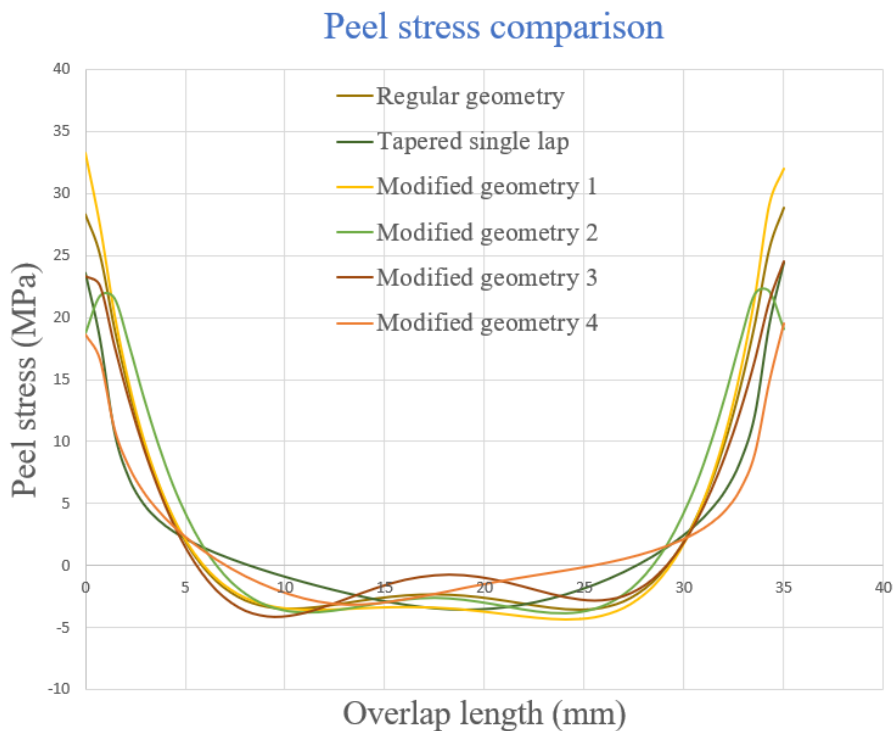


Figure 8.24. Peel stress comparison of the different geometries.

The maximum peel and shear stress values are shown in table 8.3.

Joint	Max. Shear Stress(MPa)	Max Peel Stress (MPa)
<i>Regular geometry</i>	21, 2	28, 9
<i>Tapered geometry</i>	22	24, 4
<i>Modified geometry 1</i>	25, 8	33, 3
<i>Modified geometry 2</i>	19, 6	22
<i>Modified geometry 3</i>	20, 5	24, 5
<i>Modified geometry 4</i>	21, 4	19, 5

Table 8.3. Maximum shear and peel stress comparison.

Therefore, a final design for the single lap joint is obtained, which respects the requirement of having one of the adherends completely flat for manufacturing purposes and the maximum peel stresses are reduced in a 33% with respect to the regular single lap joint. The final model is shown in figure 8.25. The boundary conditions are the same as the mechanical model previously defined and so, the materials are too.

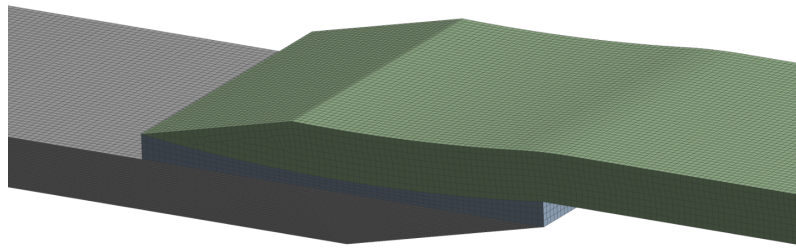


Figure 8.25. Mesh model. Final single lap joint design.

- Element type: Solid 186 tetrahedrons (20 nodes and 3 d.o.f per node)
- Number of elements: 268600
- Number of nodes: 1166565

The peel and shear distribution along the adhesive path are shown in figure 8.26.

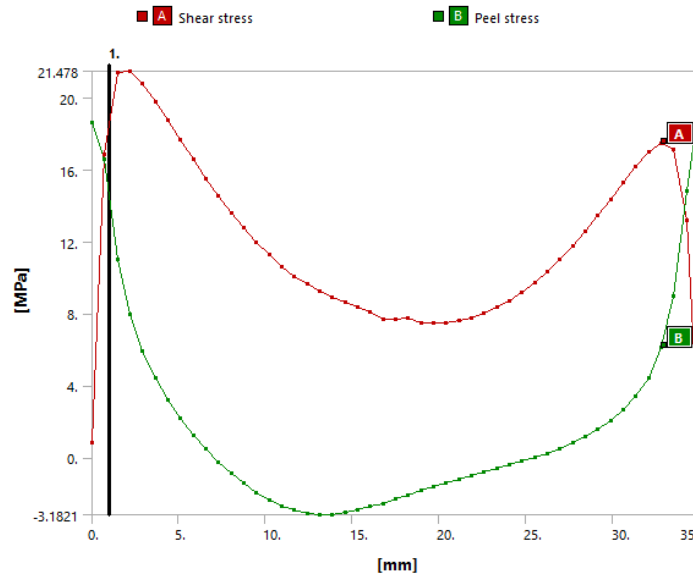


Figure 8.26. Peel and shear stress distribution along the overlap length.

A peel stress distribution plot is shown in figure 8.27.

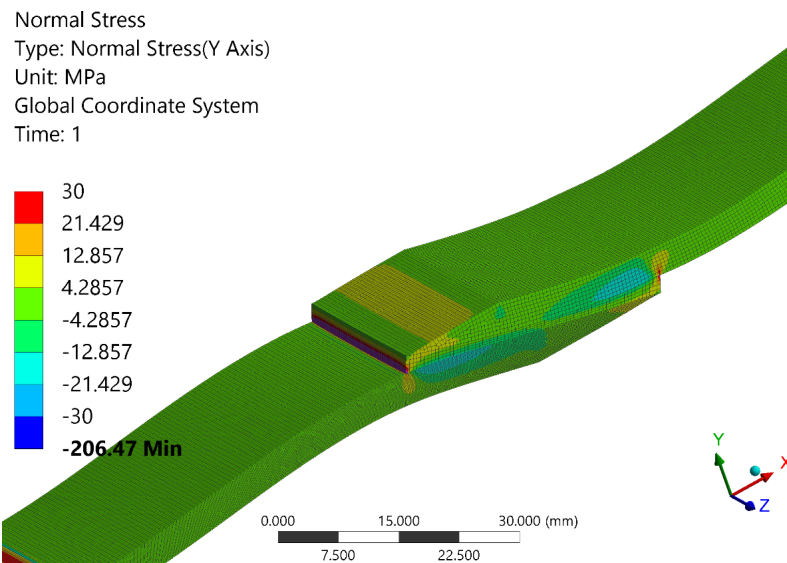


Figure 8.27. Peel stress plot.

8.3 Lay-up sequence effects on single lap joint strength

It is assumed that the lay-up sequence of the adherends has a direct impact in the joint strength. Therefore, a numerical model is set. The mechanical model used for analyzing these effects is detailed in section 7.3, where an analytical validation successfully proves that the model works as expected. The material of the adherends has been also characterized in section 5.2, thus, a lamina with those properties is used as the adherend material, by stacking up several plies of them with different orientations. The adhesive used for the analysis is not relevant since the results wanted are mostly the effects of the ply orientation of the laminate. So the previous adhesive shown in table 8.1 is used.

The adhesive layer is modeled as a solid geometry while the adherends are modeled as surfaces.

Thus, a combination of shell and solid elements is used. The numerical model is shown in figure 8.28.

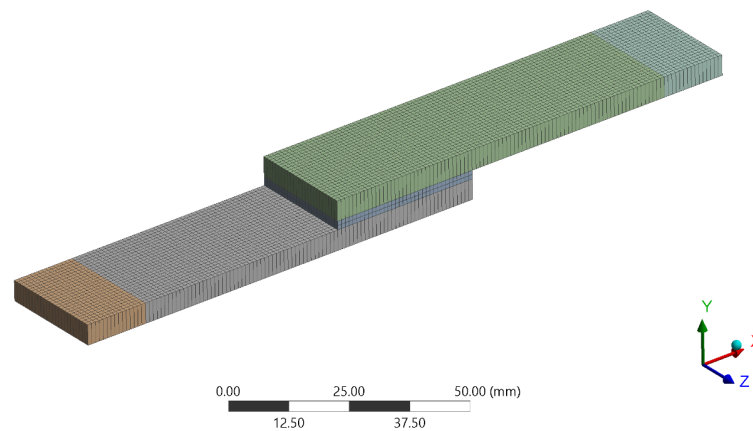


Figure 8.28. Composite single lap joint. mesh.

- Element type: Solid 186 tetrahedrons (20 nodes and 3 d.o.f per node) and Shell 181 squares (4 nodes per element and 6 d.o.f per node)
- Number of elements: 6750
- Number of nodes: 15414

The boundary conditions are defined in section 7.3 and the load applied in this case is 500N. The lay-up in general must be symmetric for the design of the chassis, therefore, two combinations are tested in finite element software. Since the stiffer the adherends are, the less they deform due to the previously explained, introduced moment, a laminate with a high equivalent stiffness has to reduce the peel stresses at the adhesive interfaces. The two lay-up sequences are $(0, 0, 90, 90)_s$ and $(90, 90, 0, 0)_s$. The notation used is taken from [Jones, 1975]. The following figures 8.29 and 8.30 show the lay-up sequences tested.

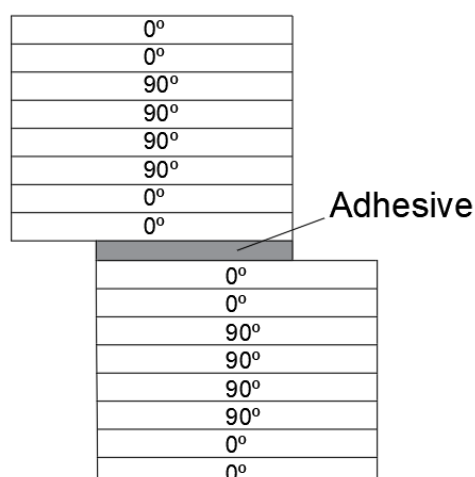


Figure 8.29. Lay-up $(0, 0, 90, 90)_s$.

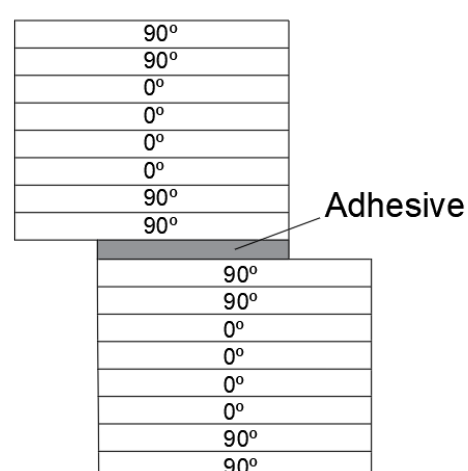


Figure 8.30. Lay-up $(90, 90, 0, 0)_s$.

The peel stresses along the adhesive interface are obtained for each sequence and the results are shown in figure 8.31.

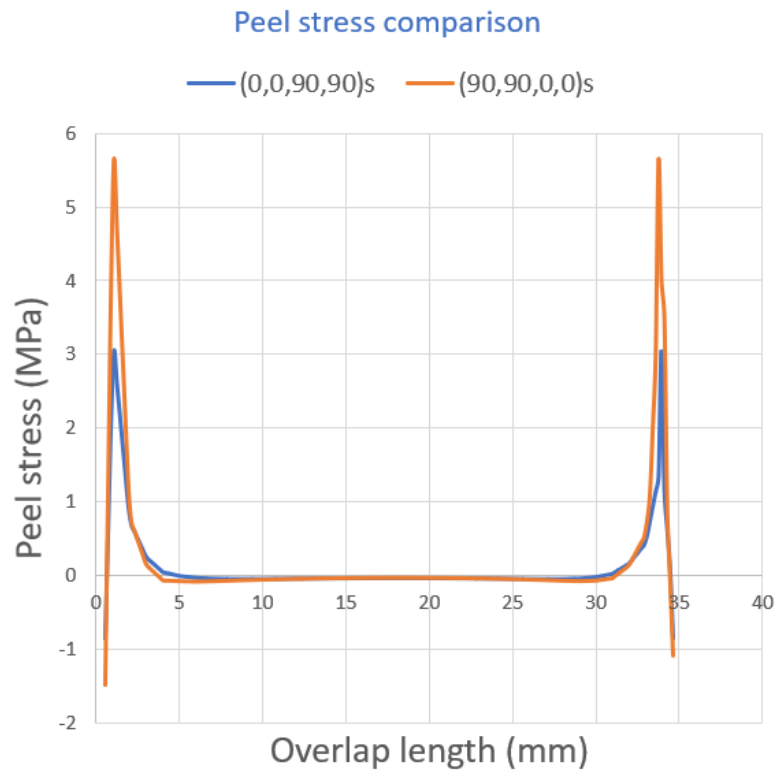


Figure 8.31. Peel stress comparison of the different lay-up configurations.

As the graphic shows, peel stress is two times lower for the sequence $(0,0,90,90)_s$ from figure 8.29. The reason is that the 0 fibers are placed on top and bottom of both adherends which increases the equivalent stiffness of each adherend.

As a general design tip, the farthest the stiffest fibers are from the mid-plane of the laminate, the strongest the adhesive joint becomes. However, fatigue damage through crack opening or crack propagation is commonly present in adhesive joints in composite structures. Due to the limited ECTS of the present project, no further research is made, so this report shows a brief introduction to the enormous field of adhesive joints in composite structures.

Final design. Conclusions

9

The geometry of the chassis for the new car, Agile SC122 from Agile Automotive is shown in figure 9.1.

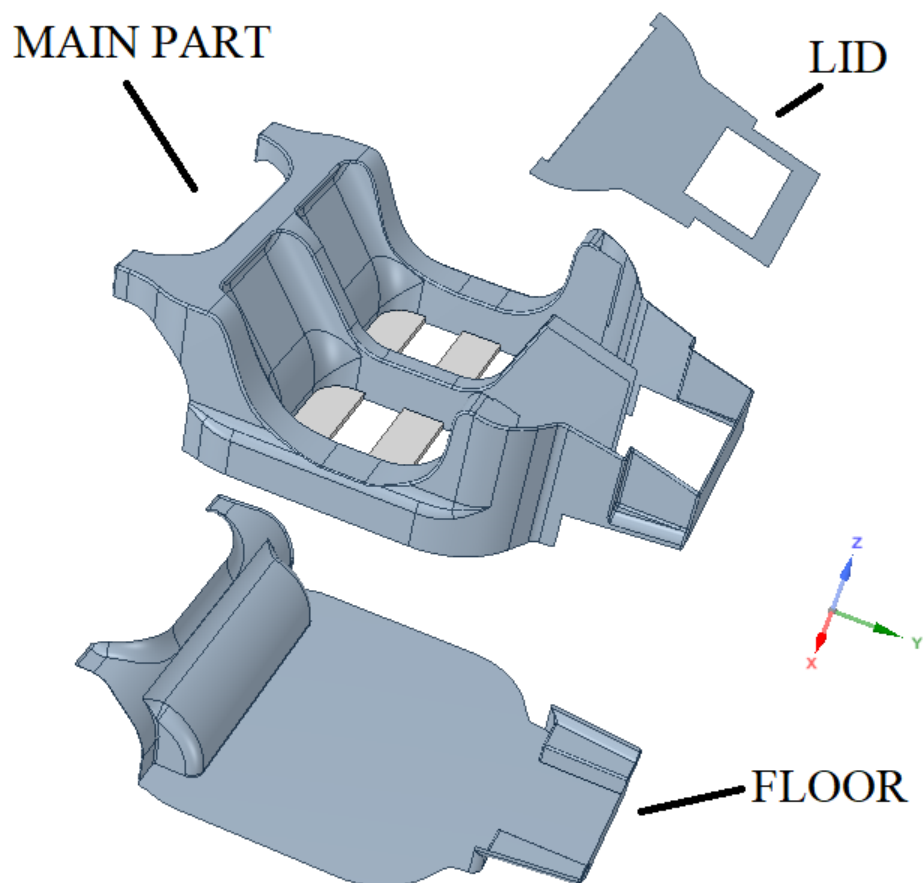


Figure 9.1. Chassis structure. Agile SC122.

The chassis is formed by three sub-structures, main part, lid and floor. The sub-structures are adhesively bonded and the torsional stiffness is reached by using shear webs as shown in figure 9.2. The thermoplastic material turned out to be less strong than the ordinary thermoset resin. However, bodywork parts can be made of thermoplastic material since they are not structural as the chassis. In that case, a manufacturing process has been developed in chapter 3 where a good A-surface is obtained.

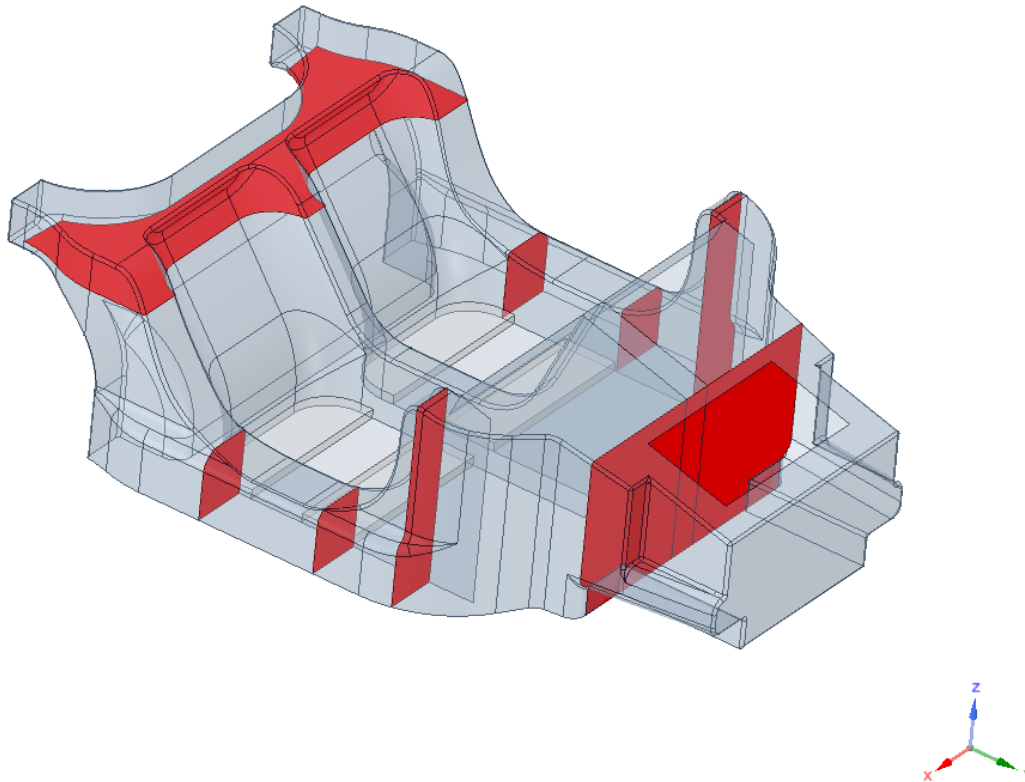


Figure 9.2. Chassis structure. Shear webs.

The main structural joint of the structure is the joint between the main part and the floor. The final joint design is shown in figure 9.3.

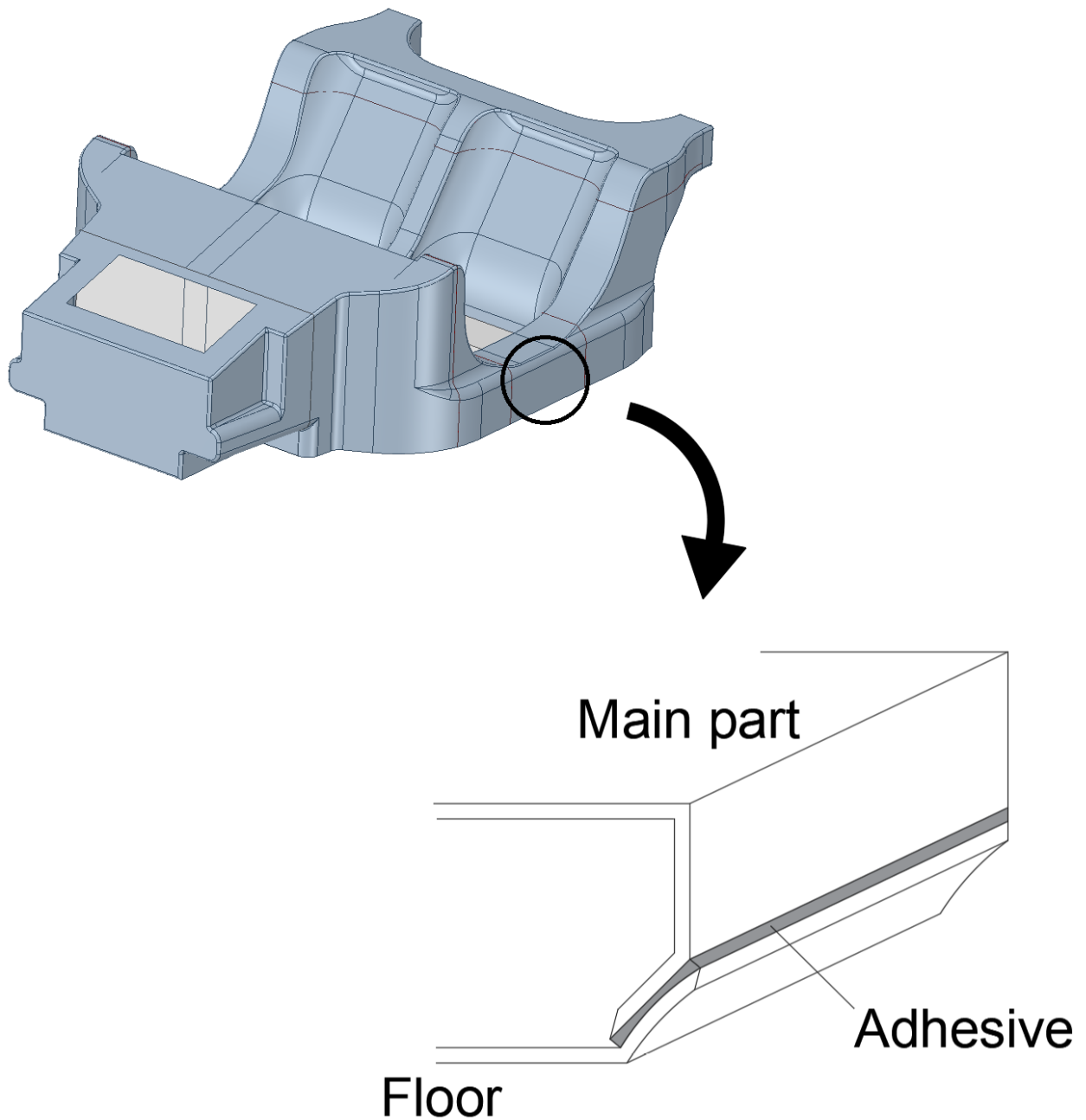


Figure 9.3. Final joint design.

Note that the lap from the floor part is curved while the lap from the main part is flat. Thus, the lap from the main part can be manufactured with a straight flange along the whole mold. Regarding the lay-up, as a design tip, the adherends should have as top and bottom plies the stiffest plies in the direction of the joint width.

References

- Agile, Automotive.** Agile. *Agile Automotive*. <http://www.agileautomotive.com/>, Automotive. [10-02-2018].
- Akzo, Nobel.** Akzo. *Akzo Nobel*. <https://www.akzonobel.com/>, Nobel. [20-04-2018].
- Araldite, Adhesives.** Araldite. *Araldite*. <http://go-araldite.com/>, Adhesives. [02-05-2018].
- Arkema, Elium.** Arkema. *Elium 188 XO technical data sheet*. <https://www.arkema.com/en/>, Elium. [02-03-2018].
- Arora, 2016.** Jasbir Arora. *Introduction to Optimum Design*. ISBN: 9780128008065. Academic Press, 2016.
- ASTM, D2344.** ASTM. *Standard Test Method For Shear Properties of Composite Materials by the V-Notched Beam Method, D2344*. [2013].
- Bodotex, 900S.** Bodotex. *Bodopox 900S technical data sheet*. <http://www.bodotex.dk/>, 900S. [10-04-2018].
- Chomarat, Carbon fabricc.** *Chomarat*. <https://composites.chomarat.com/en/product/c-weave-600t-12k-hs/>, Carbon fabricc. [10-04-2018].
- Chomarat, Fabrics.** Compagnie Chomarat. *Chomarat*. <https://chomarat.com/en/>, Fabrics. [12-04-2018].
- CI, Composite Integration.** *CI*. <http://composite-integration.co.uk/>, Composite Integration. [10-04-2018].
- Cook et al., 2001.** Robert D. Cook, David S. Malkus, Michael E. Plesha and Robert J. Witt. *Concepts and applications of finite element analysis*. ISBN: 978-0-471-35605-9. Wiley, John and Sons, 2001.
- da Silva and Adams, 2007.** Lucas F M da Silva and R D Adams. *Techniques to reduce the peel stresses in adhesive joints with composites*. 2007,227-235. International Journal of Adhesion and Adhesives, 2007.
- Dym and Shames, 2013.** Clive L. Dym and Irving H. Shames. *Solid Mechanics*. ISBN: 978-1-4614-6034-3. Springer New York, 2013.
- Goland and Reissner, 1944.** M. Goland and E. Reissner. *The Stresses in Cemented Joints*. In Journal of Applied Mechanics. a, 1944.
- Hart-Smith, 1978.** L.J. Hart-Smith. *Adhesive bonded joints for composites- Phenomenological considerations*. Conference on advanced composites technology. 1978.
- HOC, Composites.** HOC. *House of Composites*. <http://www.houseofcomposites.com/>, Composites. [10-02-2018].

- Jones, 1975.** Robert M. Jones. *Mechanics of composite materials*. ISBN: 1-56032-712-X. McGraw-Hill, 2 edition, 1975.
- Metals, Metals.** Aerospace Specification Metals. *ASM*. <http://www.aerospacemetals.com/>, Metals. [18-05-2018].
- MTU, University.** MTU. *Michigan Technological University*. <https://www.mtu.edu/>, University. [15-03-2018].
- NASA, Ergonomics.** NASA. <https://msis.jsc.nasa.gov/sections/Section03.htm>, Ergonomics. [05-07-2018].
- Qu, 2006.** Jianmin Qu. *Fundamentals of micromechanics of solids*. ISBN: 0471464511. Wiley, John and Sons, 2006.
- Raybuck, Fuel tanks.** *Raybuck*. <https://raybuck.com>, Fuel tanks. [05-07-2018].
- Sigmatex, Fabrics.** Sigmatex. *Sigmatex Material Innovation*. <http://www.sigmatex.com/>, Fabrics. [15-03-2018].
- Sigmund and P.Bendsøe., 2011.** Ole Sigmund and Martin P.Bendsøe. *Topology Optimization. Theory, Methods and Applications*. ISBN: 364207698X. Springer Berlin Heidelberg, 2 edition, 2011.
- Toray, Fabrics.** Toray. *Toray company*. <https://www.toray.com/>, Fabrics. [05-04-2018].
- Volkersen, 1938.** O. Volkersen. *Nietkraftverteilung in zugbeanspruchten nietverbindungen mit konstanten Laschenquerschnitten*. In *Luftfahrtforschung*. 1938.

Topology optimization of the chassis geometry A

The topology optimization is performed on the solid initial geometry shown in figure A.1.

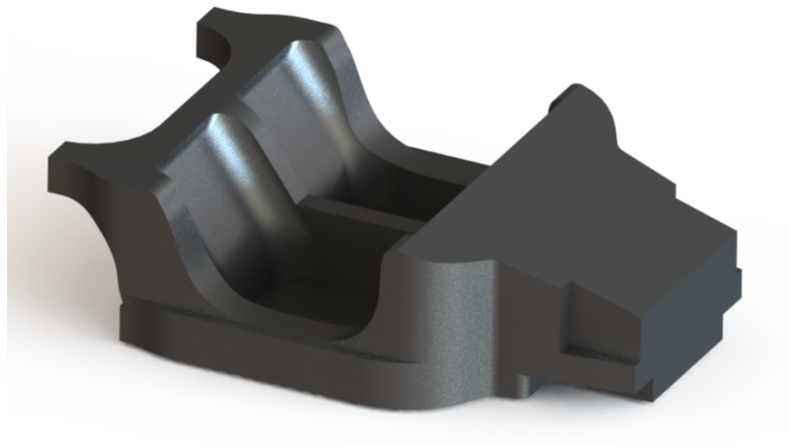


Figure A.1. Solid initial chassis geometry.

Two load cases are introduced as described in section 2.3, Loads. The front is clamped for load case 1 while the loads are applied on the rear of the structure. In contrast, the rear surfaces are clamped for load case 2, while the loads are applied at the front part of the chassis, where the wishbones are supposed to be placed. Thus, the topology optimization problem is stated as section 2.3 details. Useful information is obtained after analyzing all optimization iterations. Although the problem formulation remains unchanged, the mass constraint is set for different values in order to compare and use the most relevant one. The following sections show the obtained results for the different mass constraints for both load cases.

A.1 50% mass reduction

Case 1

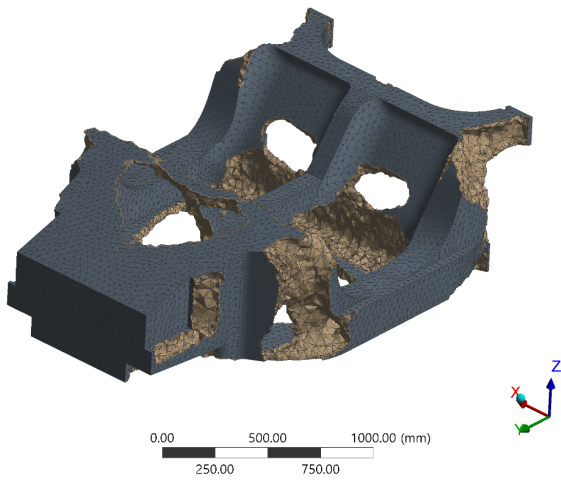


Figure A.2. Optimized mass distribution for case 1. View 1.

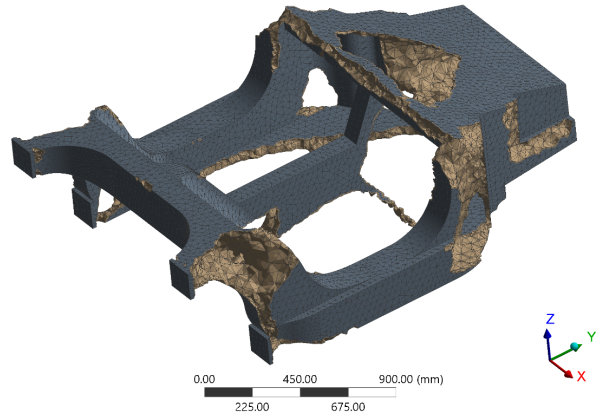


Figure A.3. Optimized mass distribution for case 1. View 2.

Case 2

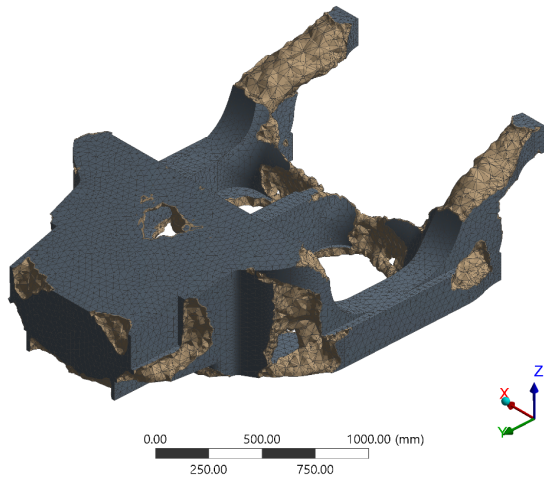


Figure A.4. Optimized mass distribution for case 2. View 1.

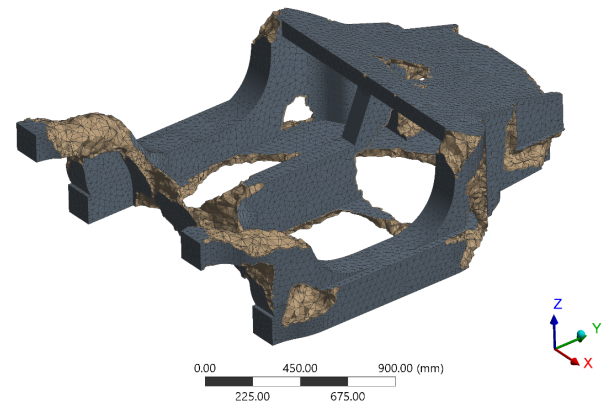


Figure A.5. Optimized mass distribution for case 2. View 2.

A.2 60% mass reduction

Case 1

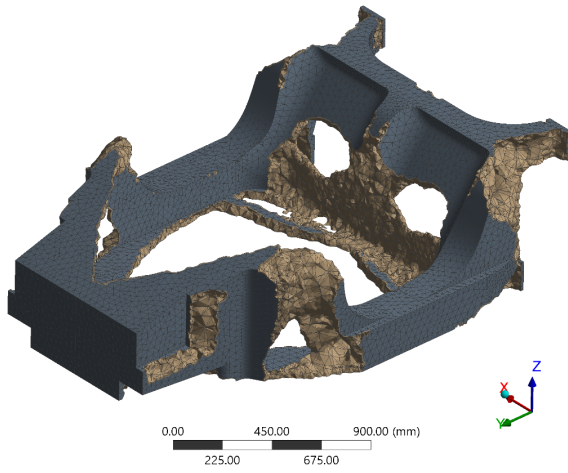


Figure A.6. Optimized mass distribution for case 1. View 1.

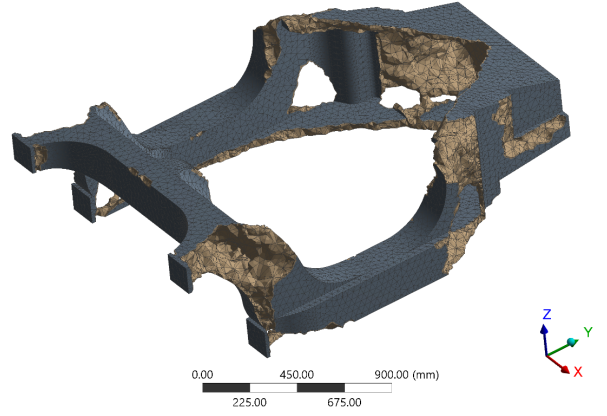


Figure A.7. Optimized mass distribution for case 1. View 2.

Case 2

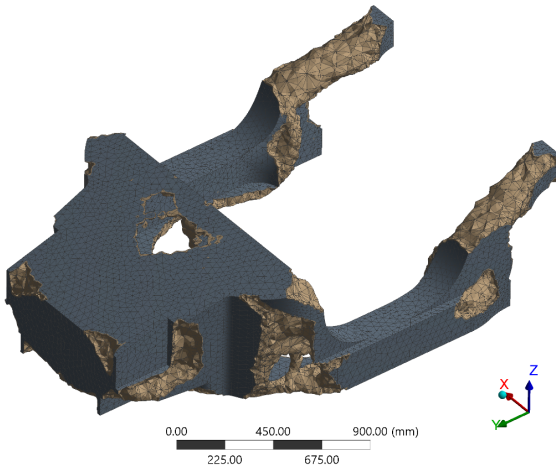


Figure A.8. Optimized mass distribution for case 2. View 1.

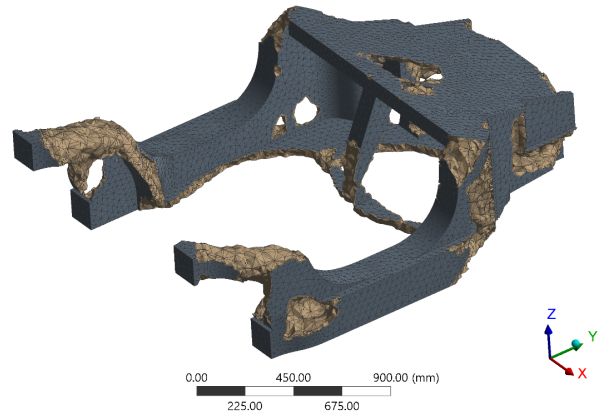


Figure A.9. Optimized mass distribution for case 2. View 2.

A.3 70% mass reduction

Case 1

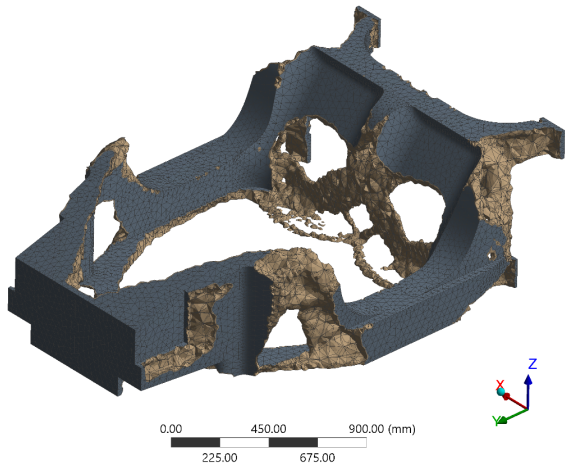


Figure A.10. Optimized mass distribution for case 1. View 1.

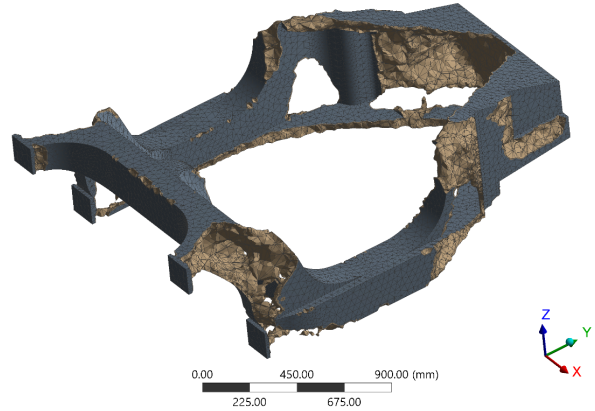


Figure A.11. Optimized mass distribution for case 1. View 2.

Case 2

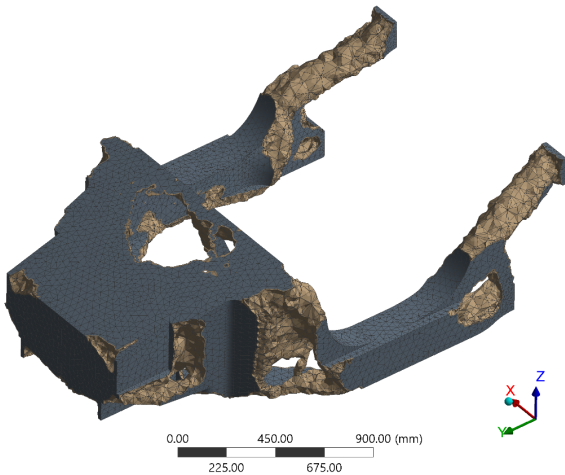


Figure A.12. Optimized mass distribution for case 2. View 1.

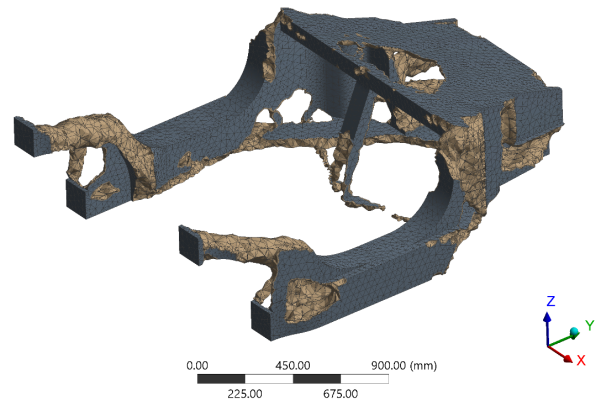


Figure A.13. Optimized mass distribution for case 2. View 2.

A.4 80% mass reduction

Case 1

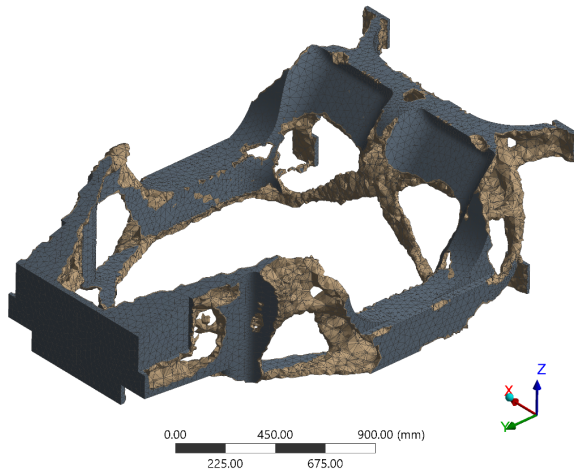


Figure A.14. Optimized mass distribution for case 1. View 1.

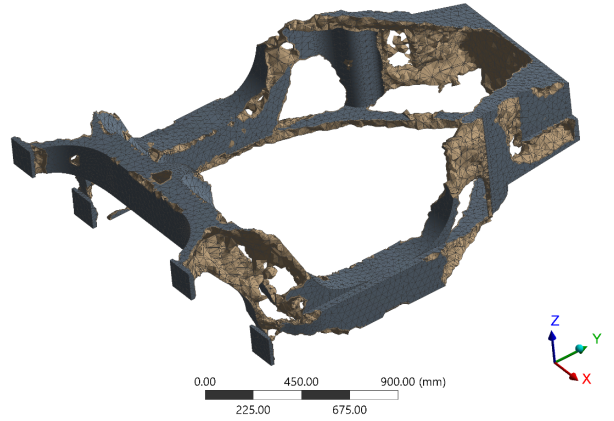


Figure A.15. Optimized mass distribution for case 1. View 2.

Case 2

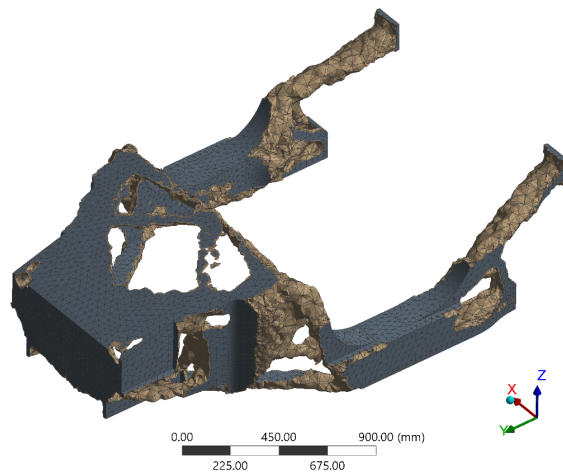


Figure A.16. Optimized mass distribution for case 2. View 1.

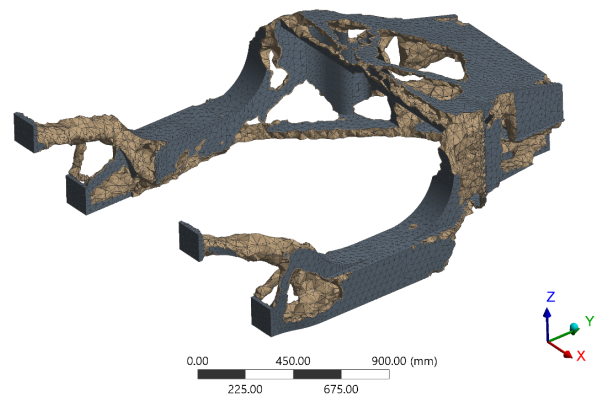


Figure A.17. Optimized mass distribution for case 2. View 2.

Shell geometry. Iterative design process

B

All iterations for the final shell geometry of the chassis are detailed in this appendix.

B.1 Iteration 1

The first iteration is the initial guess.

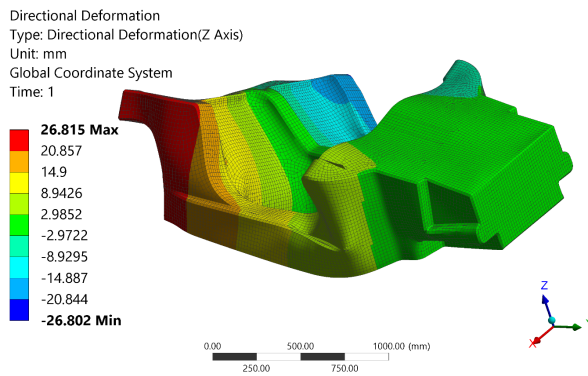


Figure B.1. Directional deformation. View one.

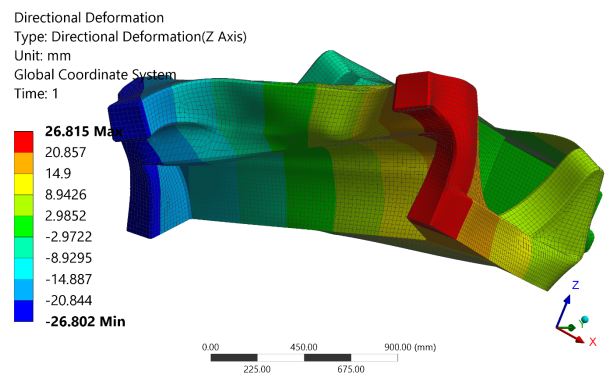


Figure B.2. Directional deformation. View two.

- Element type: Shell 181 Quads (4 nodes and 6 d.o.f per node)
- Number of elements: 33268
- Number of nodes: 33607

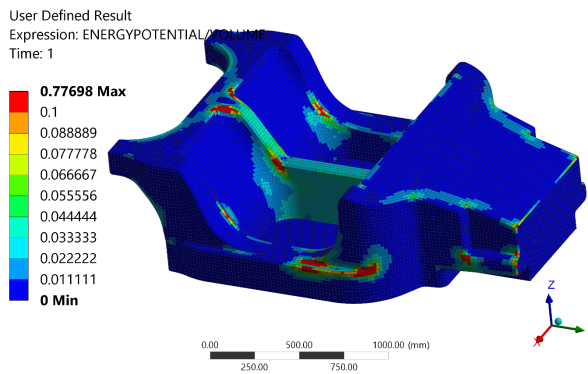


Figure B.3. Strain energy density. View one.

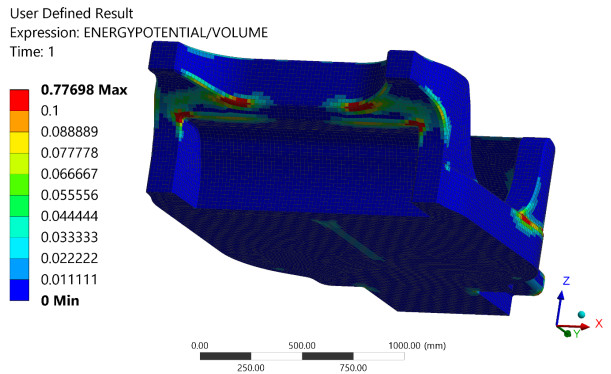


Figure B.4. Strain energy density. View two.

Iteration	Mass (kg)	Maximum "Y" disp. (mm)	Torsional stiffness (Nm/deg)
1	77,9	26,8	6580

Table B.1. Iteration 1 results.

From the deformation (B.1 and B.2), it is shown that the sharp corners produce local bending of the faces. Moreover, the places where local stiffness has to be increased are obtained from the strain energy density (B.3 and B.4). Table B.1 shows the obtained stiffness and mass results.

B.2 Iteration 2

Geometry transitions are smoothed (B.5), so the corners are transformed into curves or fillets to facilitate the soft stress transition along the geometry. Furthermore, two shear webs are added as shown in figure B.6. The shear webs are responsible of carrying the shear stress produced by the deformation mode of the shell, producing stiffer faces. A cut on the front lid is introduced to have space for the battery.

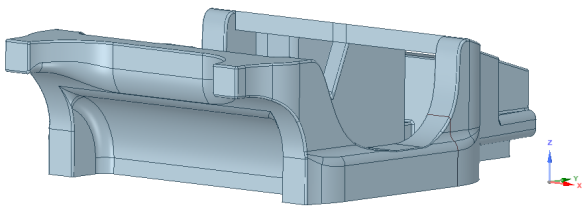


Figure B.5. Shell geometry 2. View 1.

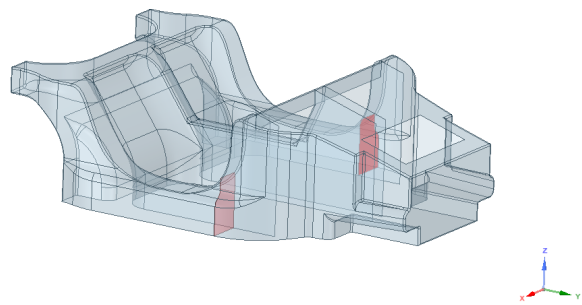


Figure B.6. Shell geometry 2. View 2.

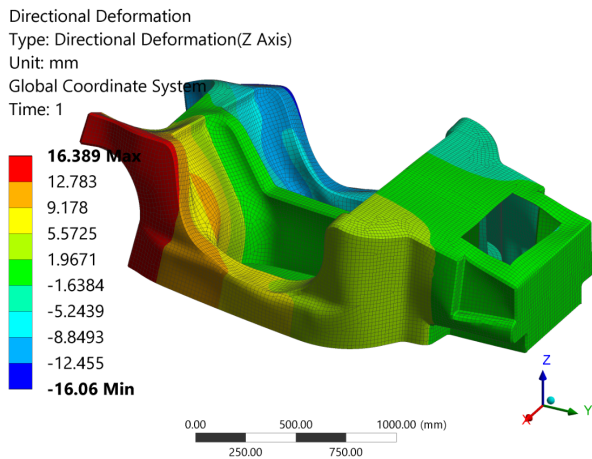


Figure B.7. Directional deformation. View one.

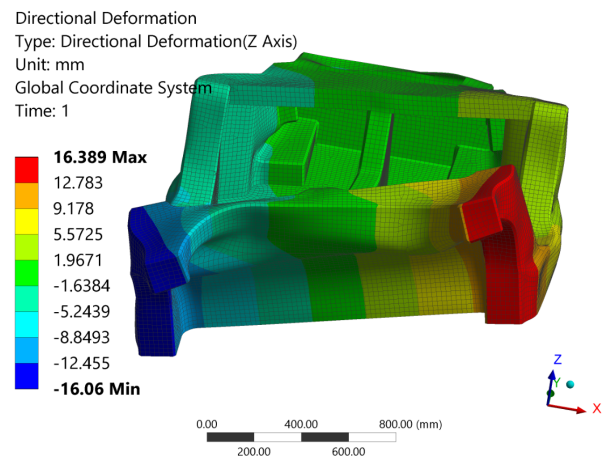


Figure B.8. Directional deformation. View two.

- Element type: Shell 181 Quads (4 nodes and 6 d.o.f per node)
- Number of elements: 29803
- Number of nodes: 29577

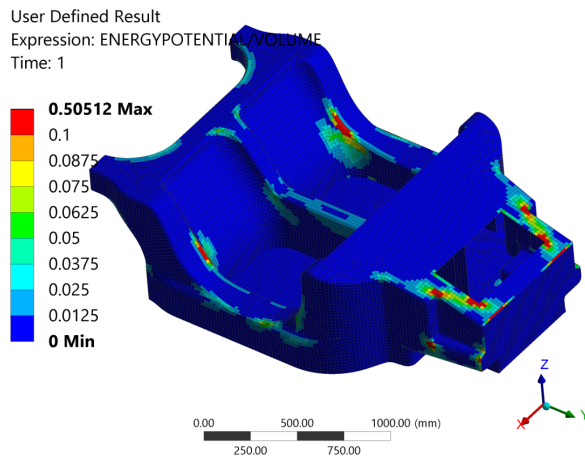


Figure B.9. Strain energy density. View one.

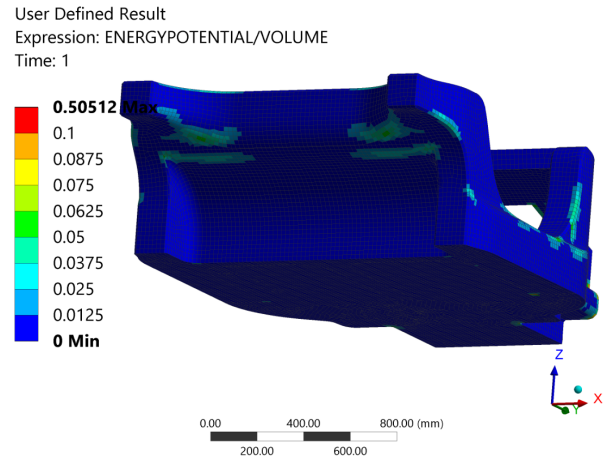


Figure B.10. Strain energy density. View two.

Iteration	Mass (kg)	Maximum "Y" disp. (mm)	Torsional stiffness (Nm/deg)
2	78	16,389	10756

Table B.2. Iteration 2 results.

The results show a clear improvement in stiffness (B.2). However from the deformation state in figures B.7 and B.8 it is deduced that the sides of the chassis and the rear central beam can be enhanced. The new cut on the front lid produces higher strain energy density results in the elements around the edges (B.9 and B.10). But since the hole has to be kept, that problem has to be solved when the design with carbon fiber is done by placing core material reinforced with stiff carbon fabrics.

B.3 Iteration 3

Existing side shear webs are extended to completely stabilize the face sheets and a new shear web is introduced in the rear beam of the chassis as shown in figure B.11.

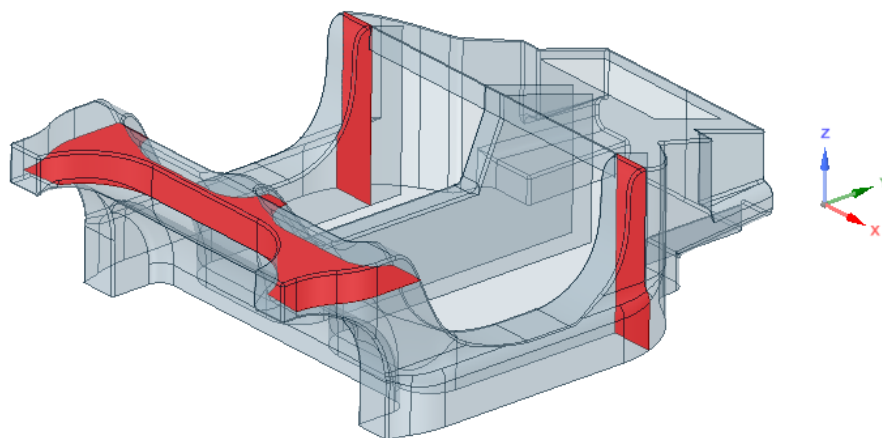


Figure B.11. Shell geometry 3.

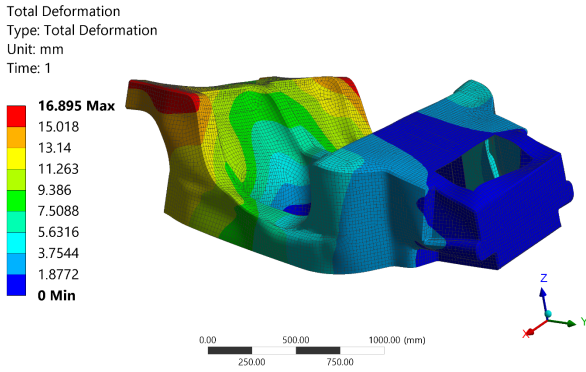


Figure B.12. Directional deformation. View one.

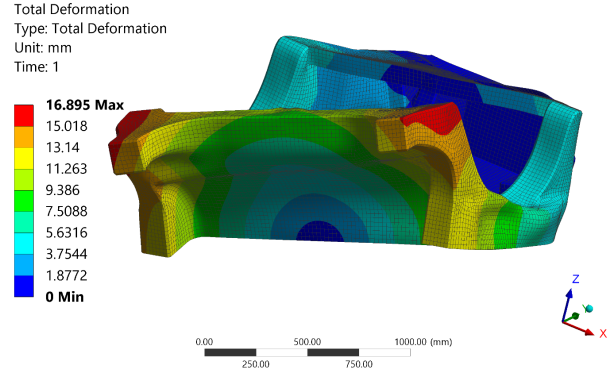


Figure B.13. Directional deformation. View two.

- Element type: Shell 181 Quads (4 nodes and 6 d.o.f per node)
- Number of elements: 31274
- Number of nodes: 31308

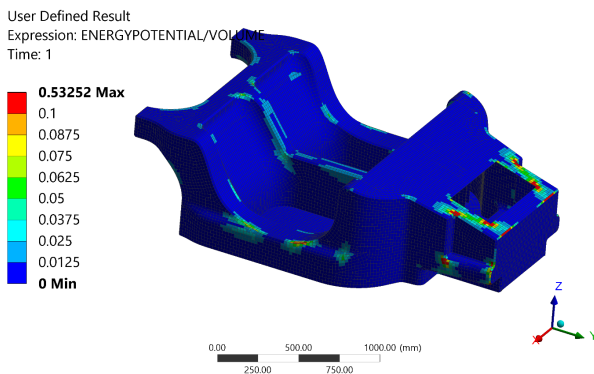


Figure B.14. Strain energy density. View one.

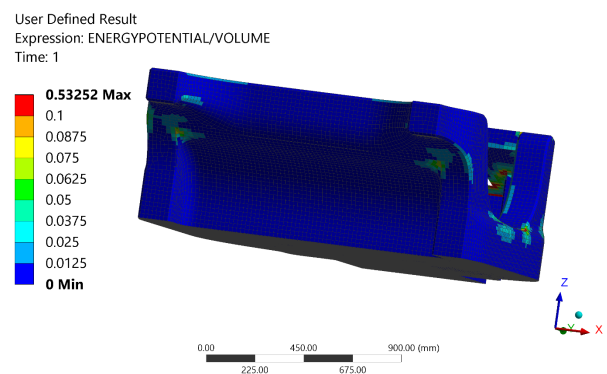


Figure B.15. Strain energy density. View two.

Iteration	Mass (kg)	Maximum "Y" disp. (mm)	Torsional stiffness (Nm/deg)
3	77,2	12,942	13620

Table B.3. Iteration 3 results.

From figure B.12, it is shown that the deformation in the sides has been reduced by extending the shear webs. However, there is still room for improvement at the rear part of the side beams. In figure B.13 an enhanced stiffness is obtained by introducing the rear shear web. The strain energy density plots (B.14 and B.15) confirm that the strain energy is more evenly distributed, producing a stiffer geometry. Results for the current iteration are shown in table B.3.

B.4 Iteration 4

A new horizontal shear web is introduced in the model (B.16). The aim of this new component is to completely stabilize the parallel face sheets of the side beams of the chassis.

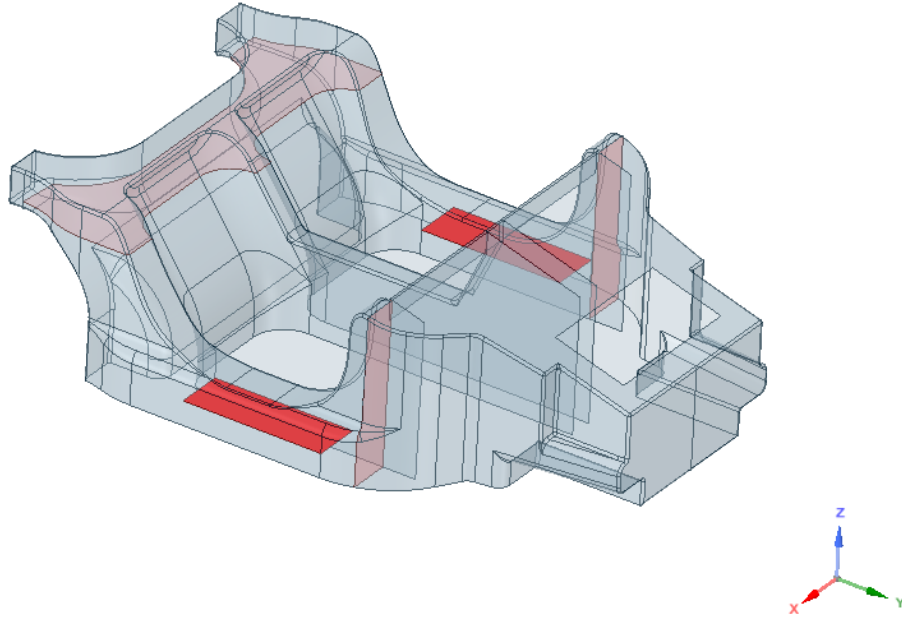


Figure B.16. Shell geometry 4.

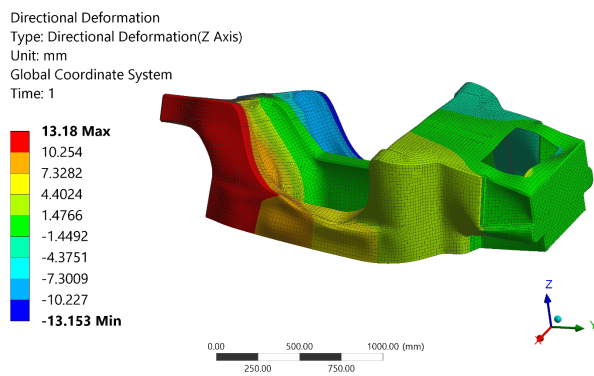


Figure B.17. Directional deformation. View one.

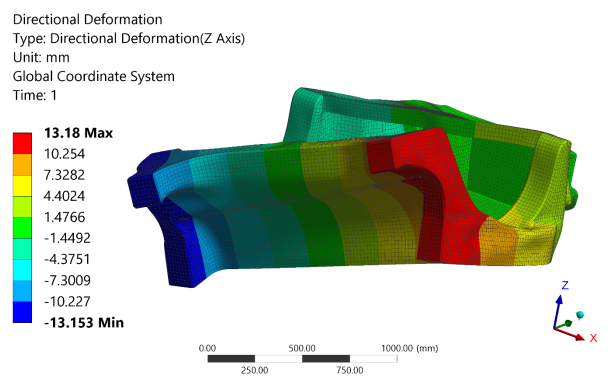


Figure B.18. Directional deformation. View two.

- Element type: Shell 181 Quads (4 nodes and 6 d.o.f per node)
- Number of elements: 31809
- Number of nodes: 31932

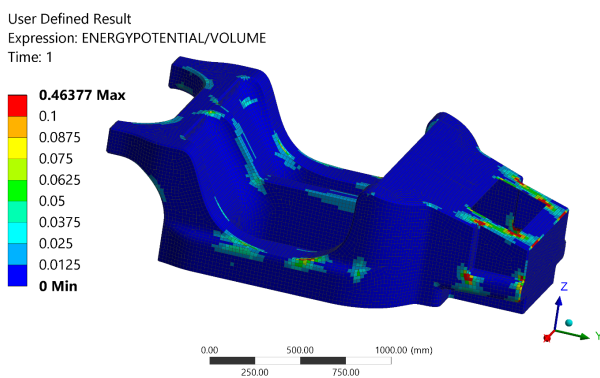


Figure B.19. Strain energy density. View one.

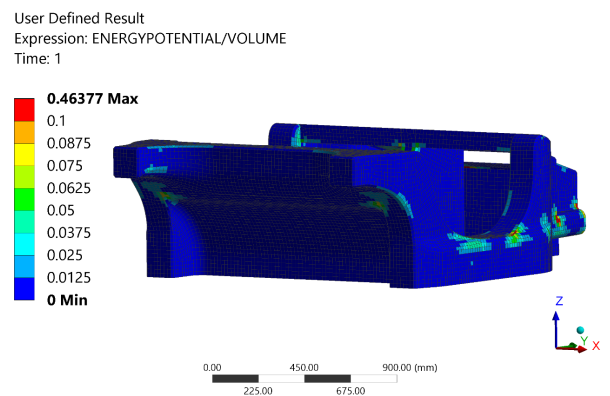


Figure B.20. Strain energy density. View two.

Iteration	Mass (kg)	Maximum "Y" disp. (mm)	Torsional stiffness (Nm/deg)
4	76,8	13,18	13374

Table B.4. Iteration 4 results.

The introduced shear web is not working as efficiently as it is supposed to do. The deformation of the side beams is still producing local bending of the faces because they are too high so the local bending is moved to the upper and lower parts of the side beams (B.17 and B.18). Moreover, the strain energy density is re-distributed in the side beams but it still produces high strain energy concentrations (B.19 and B.20). As a consequence of introducing the new shear webs, in order to keep the mass to a similar value with respect to the previous iteration, the whole thickness of the model is reduced. Table B.4 shows the stiffness and mass results. As the table shows, the stiffness is decreased as a result of the new geometry which keeps the same mass but introduces a new shear web. Thus, the shear web introduced is not implemented in the design.

B.5 Iteration 5

Instead of the horizontal shear web introduced in the previous iteration, two vertical shear webs are placed in the side beams to stabilize the face sheets and avoid local bending (B.21).

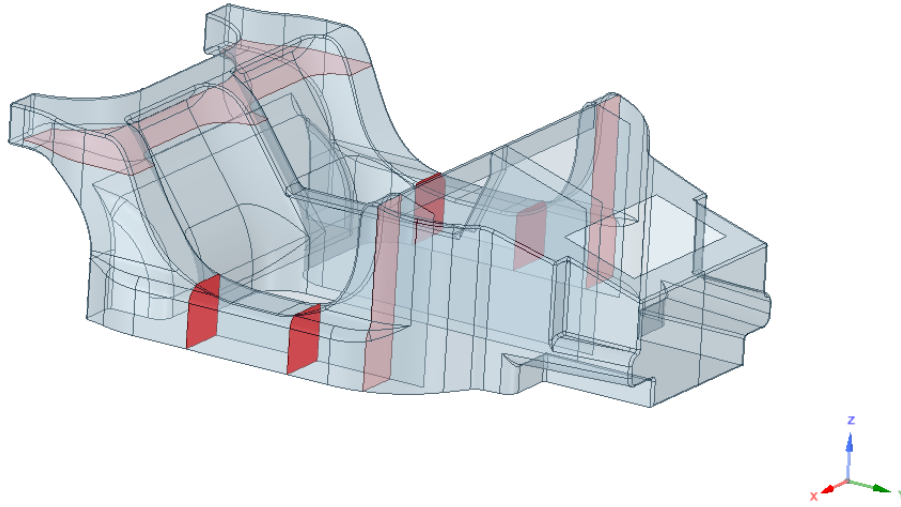


Figure B.21. Shell geometry 5.

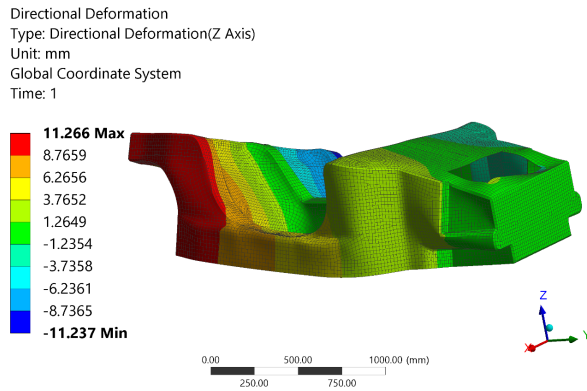


Figure B.22. Directional deformation. View one.

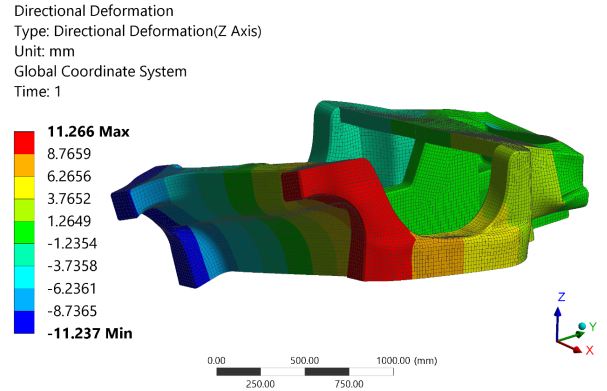


Figure B.23. Directional deformation. View two.

- Element type: Shell 181 Quads (4 nodes and 6 d.o.f per node)
- Number of elements: 31740
- Number of nodes: 31629

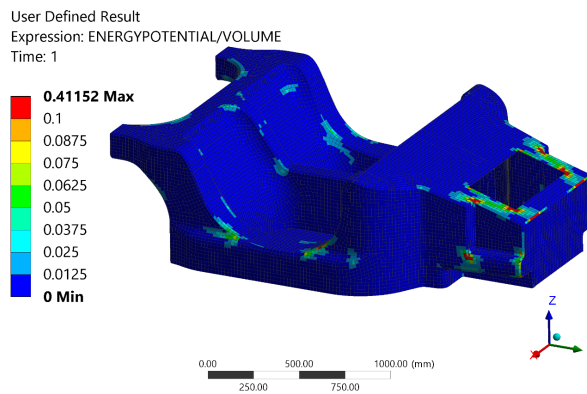


Figure B.24. Strain energy density. View one.

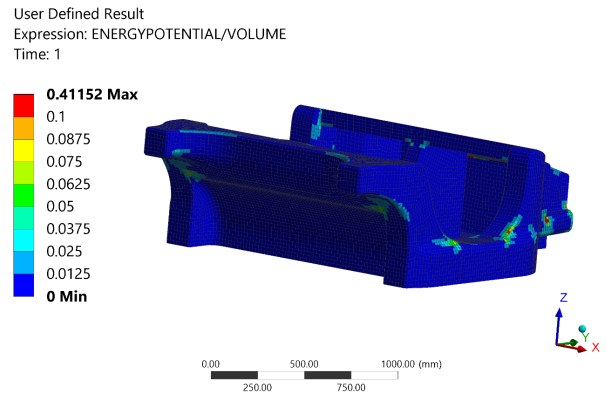


Figure B.25. Strain energy density. View two.

Iteration	Mass (kg)	Maximum "Y" disp. (mm)	Torsional stiffness (Nm/deg)
5	78,3	11,26	15655

Table B.5. Iteration 5 results.

The new deformed shape becomes more even than the previous iteration (B.22 and B.23). In this iteration the local bending of the side beams is almost removed completely which means that the new shear webs work as expected. Moreover, the strain energy density, (B.24 and B.25) is more evenly distributed although there is still room for improvement. Table B.5 displays the results where it is shown that the stiffness has increased significantly while the mass is kept.

B.6 Iteration 6

A front firewall is added to the shell structure and transverse beams to increase stiffness while they are the main support for the seats. The new components are shown in figure B.26. Moreover, the longitudinal central beam in between the two seats is lowered and extended until touching the front firewall.

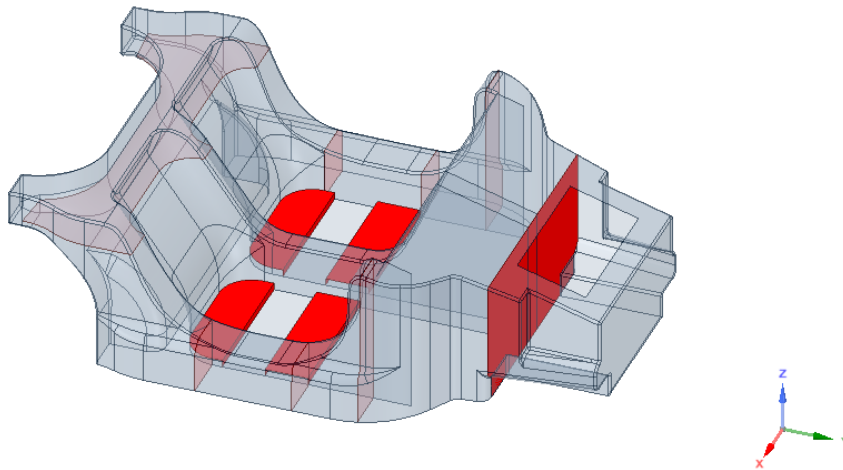


Figure B.26. Shell geometry 6.

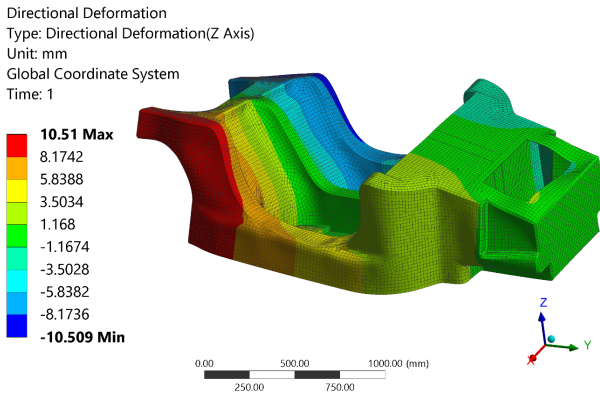


Figure B.27. Directional deformation. View one.

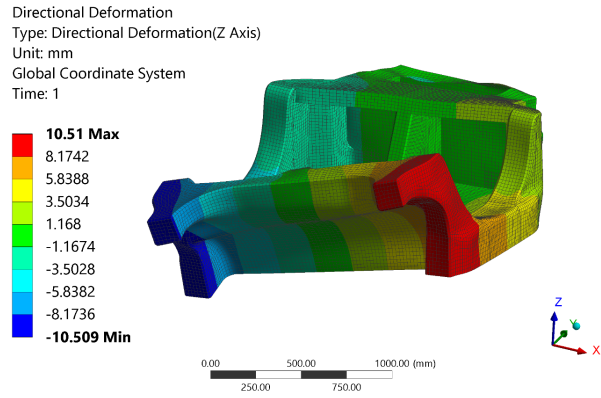


Figure B.28. Directional deformation. View two.

- Element type: Shell 181 Quads (4 nodes and 6 d.o.f per node)
- Number of elements: 34083
- Number of nodes: 34427

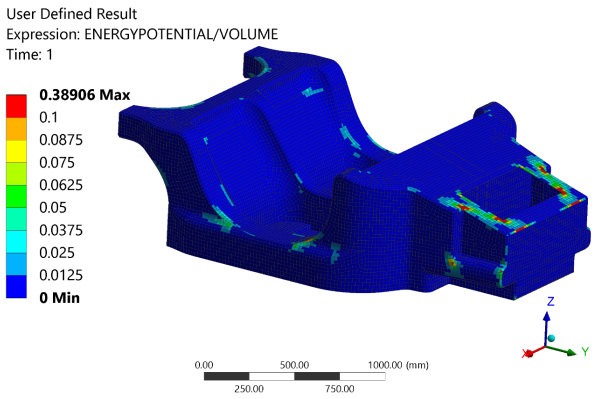


Figure B.29. Strain energy density. View one.

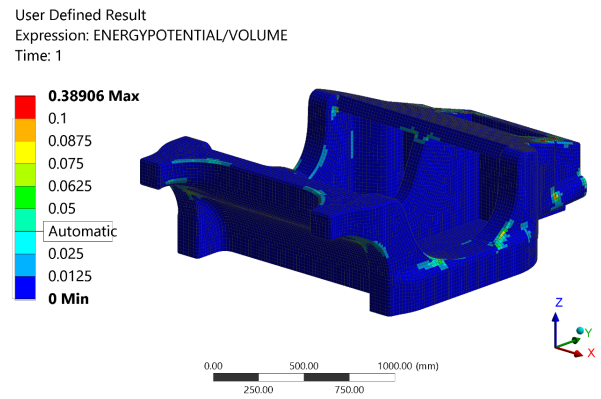


Figure B.30. Strain energy density. View two.

Iteration	Mass (kg)	Maximum "Y" disp. (mm)	Torsional stiffness (Nm/deg)
6	83,7	10,5	17044

Table B.6. Iteration 6 results.

Figures B.27 and B.28 show the deformation of the final iteration. The scaled plot shows an almost homogeneous deformation along the whole geometry which is interpreted as an excellent result. The strain energy density is also evenly distributed (B.29 and B.30). Therefore, as it is shown in table B.6, the final stiffness results are really close to the desired result of 20000 Nm/deg while the mass is kept to the 80 kg target approximately.

Elium 188 XO TDS



ELIUM[®] 180 LIQUID THERMOPLASTIC RESIN

Technical Datasheet

- For Infusion and RTM processes at ambient- or elevated temperature to produce thermoplastic continuous glass, carbon or natural fiber composites reinforcements.
- Due to low viscosity of the resin at room temperature, the same low pressure processes and similar equipment's used today to process thermoset composite parts can be used.
- The resulting thermoplastic composite parts show mechanical properties similar to those parts made of epoxy resins while presenting the major advantages of being post-thermoformable and recyclable.

PROPERTIES (CURING CONDITIONS: 200G RESIN + 3W% DIBENZOYL PEROXIDE AT ROOM TEMPERATURE)

Brookfield Viscosity (@ 25 °C)	100	m.Pas	
Liquid density	1,01	g/cm ³	ISO 1675
Appearance	Colorless limpid liquid		
Pot life	60 - 90	min	
Peroxide ratio	2.4	%	BPO
Standard packages	180	kg drum	
Shelf life	6 months when stored in sealed containers, protected from light and at a temperature between 15 – 25 °C		

TYPICAL CURED RESIN NON REINFORCED PROPERTIES (POST CURING 24H AT 60°C)

Shore D hardness	85 - 90		ISO 868
Heat deflection temperature	76	°C	ISO 75
Water uptake (8 days @ 60°C)	0,5	%	ISO 62
Coefficient of linear expansion	0,065	mm/m°C	ISO 2155-1
Fracture toughness stress intensity, K _{1c}	1,2	MPa.m ^{0,5}	ISO 13586
Elongation at break	2,8	%	ISO 527
Flexural Strength	111	MPa	ISO 178
Flexural Modulus	2,91	GPa	ISO 178
Tensile Strength	66	MPa	ISO 527
Tensile Modulus	3,17	GPa	ISO 527
Compression Strength	116	MPa	ISO 14126
Compression Modulus	3,83	GPa	ISO 14126

¹ Properties are typical values based on the Elium 180 resin tested in our laboratories. Typical values should not be construed as a guaranteed analysis of any specific lot or as specification items.

This results are applicable for Elium 180 and Elium 188 XO.

If a less or higher reactive resin is needed, please contact your Arkema representative for more informations. A material safety data sheet and a short processing guidance for the product is available on request.

Disclaimer - Please consult Arkema's disclaimer regarding the use of Arkema's products on <http://www.arkema.com/en/products/product-safety/disclaimer/index.html>

Headquarters: Arkema France
420, rue d'Estienne d'Orves
92705 Colombes Cedex - France
Tel.: +33 (0)1 49 00 80 80 - Fax: +33 (0)1 49 83 96
arkema.com - forane.com

ELIUM[®]
BY ARKEMA

Arkema France - A French "société anonyme", registered with the Commercial and Companies Register of Nanterre (France) under number 319 632 796 - August 2017

Figure C.1. Elium 188 XO TDS.

Perkadox CH-50X TDS

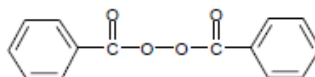
D



Product Data Sheet

Perkadox[®] CH-50X

Product description Dibenzoyl peroxide, powder, 50% with dicyclohexyl phthalate



CAS No. : 94-36-0
EINECS/ELINCS No. : 202-327-6
TSCA status : listed on inventory

Specifications Appearance : white free flowing powder
Assay : 48.0-50.0%

Characteristics Density : 1.230 g/cm³
Bulk density : 0.620-0.650 g/cm³

Storage Due to the relatively unstable nature of organic peroxides a loss of quality can be detected over a period of time. To minimize the loss of quality, AkzoNobel recommends a maximum storage temperature (T₂ max.) for each organic peroxide product.

For *Perkadox* CH-50X T₂ max. = 25°C

When stored under these recommended storage conditions, *Perkadox* CH-50X will remain within the AkzoNobel specifications for a period of at least one year after delivery.

Thermal stability Organic peroxides are thermally unstable substances, which may undergo self-accelerating decomposition. The lowest temperature at which self-accelerating decomposition of a substance in the original packaging may occur is the Self-Accelerating Decomposition Temperature (SADT). The SADT is determined on the basis of the Heat Accumulation Storage Test.

For *Perkadox* CH-50X SADT : 55°C

The Heat Accumulation Storage Test is a recognized test method for the determination of the SADT of organic peroxides (see Recommendations on the Transport of Dangerous Goods, Manual of Tests and Criteria – United Nations, New York and Geneva).

Major decomposition products Carbon dioxide, benzene, benzoic acid, diphenyl, phenylbenzoate

Packaging and transport

The standard packaging is a cardboard box for 25 kg peroxide.

Both packaging and transport meet the international regulations. For the availability of other packed quantities consult your AkzoNobel representative.

Perkadox CH-50X is classified as Organic peroxide type D, solid; Division 5.2; UN 3106.

Safety and handling

Keep containers tightly closed. Store and handle *Perkadox* CH-50X in a dry well-ventilated place away from sources of heat or ignition and direct sunlight. Never weigh out in the storage room.

Avoid contact with reducing agents (e.g. amines), acids, alkalis and heavy metal compounds (e.g. accelerators, driers and metal soaps).

Please refer to the Safety Data Sheet (SDS) for further information on the safe storage, use and handling of *Perkadox* CH-50X. This information should be thoroughly reviewed prior to acceptance of this product.

The SDS is available at www.akzonobel.com/polymer.

Applications

Perkadox CH-50X is a non-caking, fine, granular powder with excellent free flowing properties containing 50% dibenzoylperoxide.

Perkadox CH-50X is used for the curing of unsaturated polyester resins and (meth)acrylic resins at ambient and elevated temperatures.

At temperatures up to 80°C, *Perkadox* CH-50X should be used in combination with an aromatic tertiary amine accelerator, above 80°C the use of an accelerator is not required.

Perkadox CH-50X is easy to handle, easy to disperse and dissolves very quickly in unsaturated polyester resins and (meth)acrylic resins.

Perkadox CH-50X does not dissolve clearly in the resin system and is therefore not applicable for the production of cured parts when a high degree of transparency is required. For these applications, the special grade *Perkadox* CH-50L is advised.

The curing system *Perkadox* CH-50X/amine accelerator shows a very fast cure that is hardly influenced by humidity and fillers.

Even at low temperatures a relatively good cure will be obtained.

A disadvantage may be the yellow color and poor light resistance of the moulded product.

For ambient temperature curing the following amine accelerators are available to adjust the gel time and speed of cure of the cure system based on *Perkadox* CH-50X:

- Accelerator NL-65-100 (N,N-Dimethyl-p-toluidine) for short gel times
- Accelerator NL-63-100 (N,N-Dimethylaniline) for medium gel times
- Accelerator NL-64-100 (N,N-Diethylaniline) for long gel times

^{*} phr = parts per hundred resin

Dosing

Depending on working conditions, the following peroxide and accelerator dosage levels are recommended:

<i>Perkadox</i> CH-50X	2 - 5 phr [*]
Amine accelerator	0.05 - 0.5 phr

Cure Characteristics

In a high reactive standard orthophthalic polyester resin the following application characteristics were determined.

Gel times at 20°C

UP resin	100	100	100	100	100	100	100
<i>Perkadox</i> CH-50X	3.0	3.0	3.0	3.0	3.0	3.0	3.0
Accelerator NL-63-100	0.1	0.4					
Accelerator NL-64-100			0.1	0.5			
Accelerator NL-65-100					0.05	0.1	0.4
Gel time (minutes)	22	6	160	20	20	5	1

Cure of 1 mm pure resin layer at 20°C

The speed of cure is expressed as the time to reach a Persoz hardness of respectively 30, 60 and 120 s.

	Persoz: 30	60	120 s
3 phr <i>Perkadox</i> CH-50X + 0.1 phr Acc. NL-63-100	0.5	0.8	2 h
3 phr <i>Perkadox</i> CH-50X + 0.4 phr Acc. NL-63-100			<0.5h
3 phr <i>Perkadox</i> CH-50X + 0.5 phr Acc. NL-64-100		0.5	1 h
3 phr <i>Perkadox</i> CH-50X + 0.05 phr Acc. NL-65-100	1	2.5	14 h
3 phr <i>Perkadox</i> CH-50X + 0.1 phr Acc. NL-65-100			0.5h

Cure of 4 mm laminates at 20°C

4 mm laminates have been made with 450 g/m² glass chopped strand mat. The glass content in the laminates is 30% (w/w).

The following parameters were determined:

- Time-temperature curve
- Speed of cure expressed as the time to achieve a Barcol hardness (934-1) of 0-5 and 25-30 respectively.
- Residual styrene content after 24h at 20°C and a subsequent postcure of 8 h at 80°C.

	Gel time min.	Time to Peak min.	Peak exotherm °C
3 phr <i>Perkadox</i> CH-50X + 0.1 phr Acc. NL-63-100	24	31	99
3 phr <i>Perkadox</i> CH-50X + 0.5 phr Acc. NL-64-100	21	26	140
3 phr <i>Perkadox</i> CH-50X + 0.05 phr Acc. NL-65-100	28	35	64

	Barcol		Res. styrene		
	0-5	25-30	24 h 20°C	+8 h 80°C	
	h	h	%	%	
3 phr <i>Perkadox</i> CH-50X + 0.1 phr Acc.NL-63-100			<1	3.2	1.0
3 phr <i>Perkadox</i> CH-50X + 0.5 phr Acc.NL-64-100			<<1	2.9	2.1
3 phr <i>Perkadox</i> CH-50X + 0.05 phr Acc.NL-65-100	1	8.5		6.6	0.8

Pot life at 20°C

Pot lives were determined of a mixture of *Perkadox* CH-50X and a non-preaccelerated UP resin at 20°C.

3 phr <i>Perkadox</i> CH-50X	21 days
6 phr <i>Perkadox</i> CH-50X	11 days

Perkadox is a registered trademark of Akzo Nobel Chemicals B.V. or affiliates in one or more territories.

All information concerning this product and/or suggestions for handling and use contained herein are offered in good faith and are believed to be reliable. AkzoNobel, however, makes no warranty as to accuracy and/or sufficiency of such information and/or suggestions, as to the product's merchantability or fitness for any particular purpose, or that any suggested use will not infringe any patent. Nothing contained herein shall be construed as granting or extending any license under any patent. Buyer must determine for himself, by preliminary tests or otherwise, the suitability of this product for his purposes. The information contained herein supersedes all previously issued bulletins on the subject matter covered. The user may forward, distribute, and/or photocopy this document only if unaltered and complete, including all of its headers and footers, and should refrain from any unauthorized use. You may not copy this document to a website.

AkzoNobel Polymer Chemistry
 Arnhem, The Netherlands
 T +31 88 969 6767
 F +31 88 969 6101
 E polymerchemistry.nl@akzonobel.com

AkzoNobel Polymer Chemistry
 Chicago, U.S.A.
 T +1 312 544 7000
 T +1 800 828 7929 (Toll free US only)
 F +1 312 544 7188
 E polymerchemistry.us@akzonobel.com

Akzo Nobel (Asia) Co., Ltd.
 Shanghai, PR China
 T +86 21 2220 5000
 F +86 21 2220 5558
 E polymerchemistry.ap@akzonobel.com

www.akzonobel.com/polymer

TS 65919.12/December 2015
 Page 4 of 4

Thermoplastic testing.

A-surface issue

E

Test 1

Test	Lay-up	Sizing	Vacuum	Mesh	Release/gelcoat	Quality
1	2xTwill/12K 600g	TP	100%/60%	Full mesh	Yes/No	2

Table E.1. Test 1.

The first test shows a bad quality a-surface, which is shown in figure E.



Figure E.1. Test 1.

Test 2

Test	Lay-up	Sizing	Vacuum	Mesh	Release/gelcoat	Quality
2	2xTwill/12K 600g	TS	100%/60%	Full mesh	Yes/No	2

Table E.2. Test 2.

As it is shown in table E.2, in this case, a fabric with thermoset sizing is used to see what the results are. Figure E shows a clear improvement in the surface finishing. The quality is almost perfect, but if checking with microscope, it is seen that the fibers in contact with the mold are not wet. If the test specimen is scratched, the fibers fall a part. As it is shown in figure E, there are some dark spots in the center of the fibers which are not wet.



Figure E.2. Test 2.

Test 3

The possibility of air going inside the infusion due to the vacuum reduction is now checked. Thus, the vacuum level is kept (E.3) during the infusion process and during the curing cycle.

Test	Lay-up	Sizing	Vacuum	Mesh	Release/gelcoat	Quality
3	10xTwill/12K 600g	TP	100%/100%	Full mesh	Yes/No	2

Table E.3. Test 3.

As it is shown in figure E.3, no improvement is achieved by modifying the vacuum level variable.



Figure E.3. Test 3.

Test 4

Test	Lay-up	Sizing	Vacuum	Mesh	Release/gelcoat	Quality
4	10xTwill/12K 600g (dried)	TP	100%/60%	Full mesh	Yes/No	2

Table E.4. Test 4.

Since the thermoplastic resin is highly reactive to water, the fibers are now dried during two hours at 100°. Thus, the fibers are water free but the result shown in figure E.4 does not improve.



Figure E.4. Test 4.

Test 5

Test	Lay-up	Sizing	Vacuum	Mesh	Release/gelcoat	Quality
5	10xTwill/12K 600g	TP	100%/60%	Half mesh	Yes/No	3

Table E.5. Test 5.

A fast infusion can produce air enclosures because the resin gets infused faster on top because of the mesh while the "through the thickness" infusion can not follow the same pace. So in this test, the mesh is reduced to half of the used before, which means that the resin has more time to go through the whole laminate. However, as it is shown in figure E.5 no improvement is achieved.

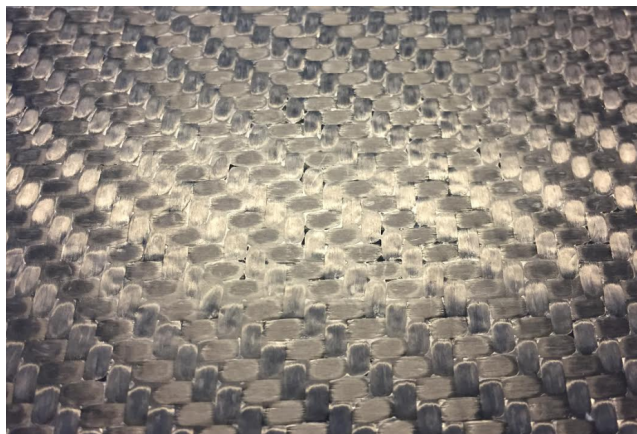


Figure E.5. Test 5.

Test 6

The curing process of the thermoplastic resin starts due to the peroxide added to the mix. According to the supplier, between 3% and 4% of peroxide can be added to the thermoplastic. Thus in this test, the upper bound is reached, which means that the mix has 4% of peroxide.

Test	Lay-up	Sizing	Vacuum	Mesh	Release/gelcoat	Quality
6	10xTwill/12K 600g	TP	100%/60%	Full mesh	Yes/No	3

Table E.6. Test 6.

Surprisingly the quality of the A-surface has improved as shown in figure E.6.

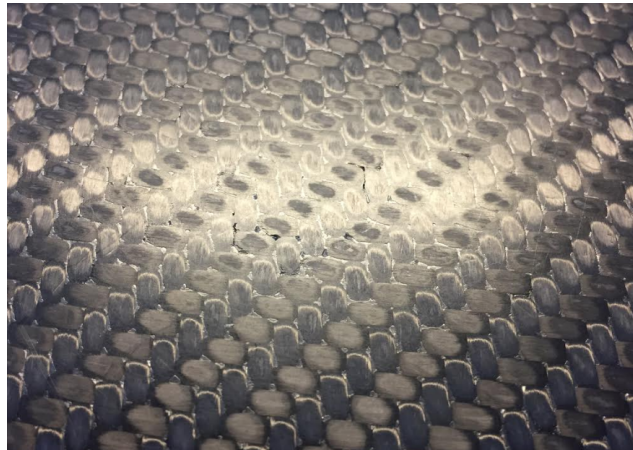


Figure E.6. Test 6.

However, the pot life is decreased by half of the original tests and the resin starts curing much faster. The short pot life means that it is not possible to infuse big parts, while having controlled the process and the quality is still not excellent.

Test 7

The possible chemical reaction of the release agent with the resin is now checked.

Test	Lay-up	Sizing	Vacuum	Mesh	Release/gelcoat	Quality
7	2xTwill/12K 600g	TP	100%/60%	No mesh	No/No	4

Table E.7. Test 7.

Instead of infusing the test sample on a mold, in this case, a plastic bag is used for top and bottom surfaces and then infused. This makes that no other products are involved into the process such as release agents or wax.



Figure E.7. Test 7.

As it is shown in figure E.7, the holes are gone and the surface is now totally continuous. However, shrinkage is observed, so that the plastic bag has shrunk together with the resin. The intention of this test is to check for some chemical reactions. Nevertheless, the issue is found, which is shrinkage. The resin shrinks and where the corners of the fiber intersections are, a hole is created because the sizing of the fabric makes it bond perfectly to the fibers.

Test 8

Test	Lay-up	Sizing	Vacuum	Mesh	Release/gelcoat	Quality
8	2xTwill/3K 600g+8g ply	TP	100%/60%	Full mesh	Yes	5

Table E.8. Test 8.

A solution is proposed for test number 8. A micro carbon fabric of chopped fibers is used as the first ply on the mold with the intention of stopping the resin from shrinking. At the same time, the fabric is $8g/m^2$ which means that after infused, it will not be seen, being mostly transparent. The fabrics are shown in figure E.8.

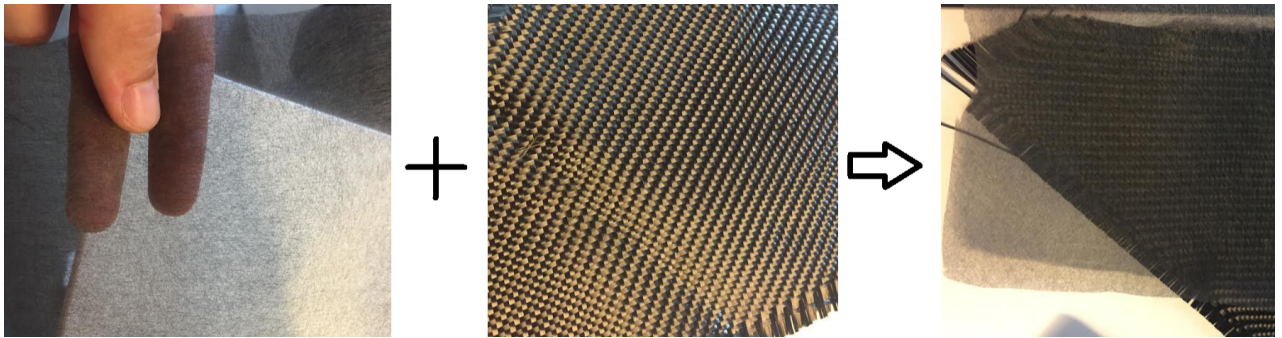


Figure E.8. Shrinkage solution for test.

As a result, a perfect A-surface is obtained as shown in figure E.9.

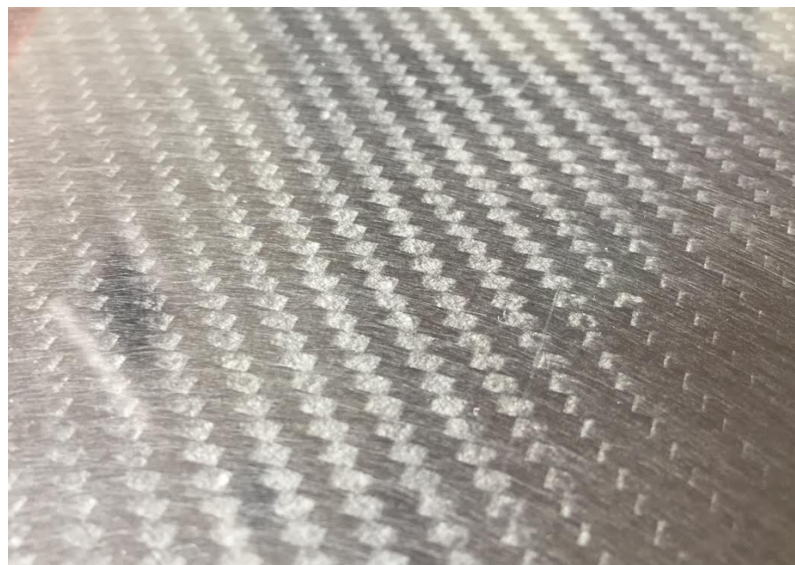


Figure E.9. Test 8

Goland & Reissner Stress Distribution. Matlab code

F

```
1 - clear all, clc, cla;
2 - % Script file: shear_goland
3 - %
4 - % Purpose:
5 - % This program calculates the shear stress distribution
6 - % for a single lap joint with the Goland & Reissner model.
7 - %
8 - % Date          Programmer          Description of change
9 - % =====          =====          =====
10 - % 11/06/2018     Efren G. Madruga          Original code
11 - %
12 - % Define variables:
13 - %
14 - P = 100;          %Applied tensile load per unit width in N/m
15 - c = 0.05;         %Half of the overlap length in m
16 - t = 0.01;         %Thickness of the adherend in m
17 - t_a = 0.020;      %Thickness of the adhesive in m
18 - x = -c:0.0002:c; %Variable x along the overlap length in m
19 - E = 100000000000; %Adherend modulus E_1 in N/m^2
20 - nu = 0.33;        %Poisson's ratio of adherends
21 - G_a = 30000000000; %Adhesive shear modulus in N/m^2
22 - E_a = 80000000000; %Adhesive modulus E in N/m^2
23 - %
24 - %
25 - %-----SHEAR STRESS DISTRIBUTION-----
26 - %
27 - % Calculate beta
28 - beta = sqrt(8.*(G_a./E).*(t./t_a));
29 - %
30 - % Calculate u_2
31 - u_2 = sqrt((3.*(1-nu^2))./(2)).*(1./t).*(sqrt(P./(t.*E)));
32 - %
33 - % Calculate the bending moment factor k
34 - k = (cosh(u_2.*c))./((cosh(u_2.*c)+(2.*sqrt(2).*sinh(u_2.*c))));
35 - %
36 - % Calculate the shear stress distribution
37 - tau = (1./8).*(P./c).*((beta.*c)./t).*(1+3.*k).*(cosh((beta.*c)./t) ...
38 - .*(x./c))./(sinh((beta.*c)./t))+3.*(1-k));
```

Figure F.1. Matlab code for single lap stress distribution. Part 1.

```

39 %
40 %-----PEEL STRESS DISTRIBUTION-----
41 %
42 % Calculate gamma
43 - a1 = 6.*(E_a./E).*(t./t_a);
44 - gamma = nthroot(a1,4);
45 %
46 % Calculate landa
47 - landa = gamma.*(c./t);
48 %
49 % Calculate delta
50 - delta = (1./2).*(sin(2.*landa)+sinh(2.*landa));
51 %
52 % Calculate R_1 and R_2
53 - R_1 = cosh(landa).*sin(landa)+sinh(landa).*cos(landa);
54 - R_2 = -cosh(landa).*sin(landa)+sinh(landa).*cos(landa);
55 %
56 % Calculate the values for A and B through kl (transverseforce factor)
57 - kl = ((k.*c)./t).*sqrt(3.*(1-nu^2).*(P./(t.*E)));
58 - A = ((R_2.*landa^2.*(k./2))+(landa.*kl.*cosh(landa).*cos(landa))) ...
59     .*cosh((landa.*x)./c).*cos((landa.*x)./c);
60 - B = ((R_1.*landa^2.*(k./2))+(landa.*kl.*sinh(landa).*sin(landa))) ...
61     .*sinh((landa.*x)./c).*sin((landa.*x)./c);
62 %
63 %Calculate peel stress distribution
64 - sigma = (1./delta).*((P.*t)./c^2).*(A+B);
65 %
66 %Plot shear stress and peel stress
67 - plot(x,tau,'r');
68 - hold on
69 - plot(x,sigma,'g');
70 - grid on;
71 - xlabel ('lap length "x" (m)');
72 - ylabel ('Stress (N/m^2)');
73 - title ('shear stress and peel stress of single lap joint');
74 - legend('sigma','tau');

```

Figure F.2. Matlab code for single lap stress distribution. Part 2.

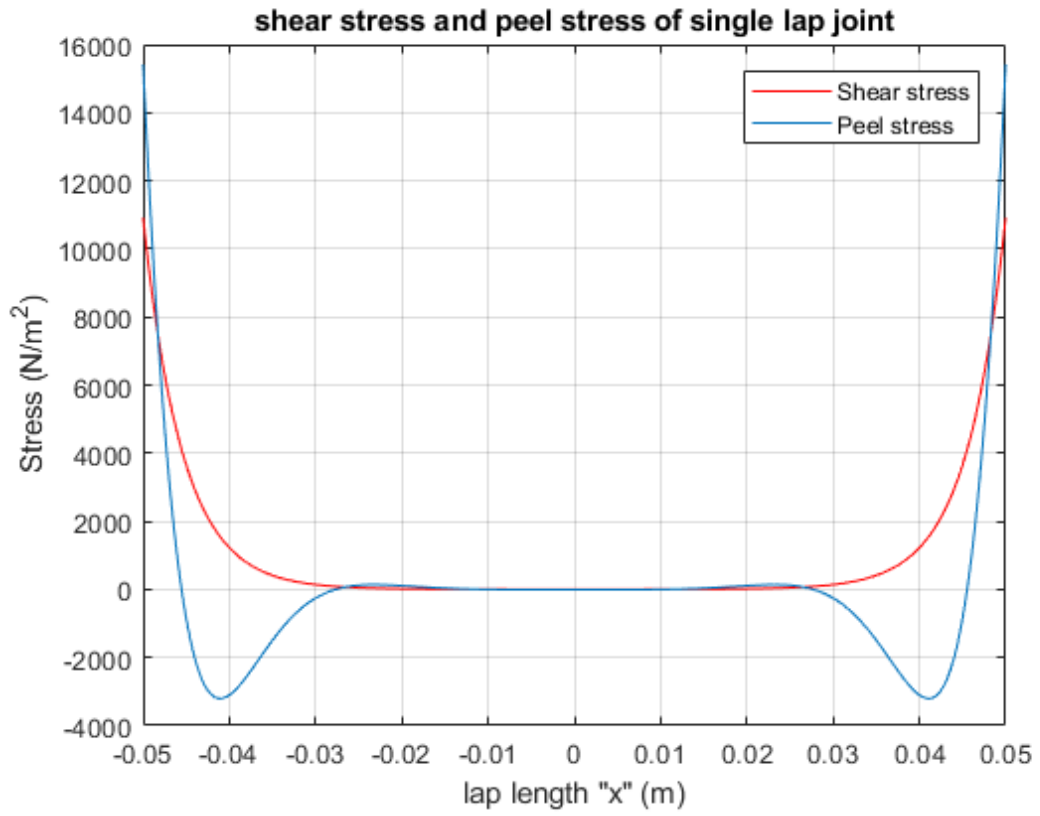


Figure F.3. Stress distribution plots. Shear and peel stress.